

**A MODELING AND CONTROL HIERARCHY OF QUADRUPEDAL
RUNNING WITH TORSO COMPLIANCE**

by
Qu Cao

A dissertation submitted to the Faculty of the University of Delaware in partial fulfillment of the requirements for the degree of Doctor of Philosophy in Mechanical Engineering

2016 Spring

© 2016 Qu Cao
All Rights Reserved

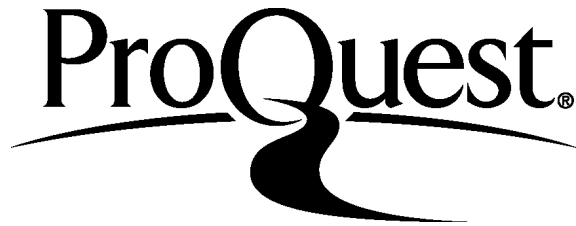
ProQuest Number: 10156494

All rights reserved

INFORMATION TO ALL USERS

The quality of this reproduction is dependent upon the quality of the copy submitted.

In the unlikely event that the author did not send a complete manuscript and there are missing pages, these will be noted. Also, if material had to be removed, a note will indicate the deletion.



ProQuest 10156494

Published by ProQuest LLC (2016). Copyright of the Dissertation is held by the Author.

All rights reserved.

This work is protected against unauthorized copying under Title 17, United States Code
Microform Edition © ProQuest LLC.

ProQuest LLC.
789 East Eisenhower Parkway
P.O. Box 1346
Ann Arbor, MI 48106 - 1346

**A MODELING AND CONTROL HIERARCHY OF QUADRUPEDAL
RUNNING WITH TORSO COMPLIANCE**

by

Qu Cao

Approved: _____
Suresh G. Advani, Ph.D.
Chair of the Department of Mechanical Engineering

Approved: _____
Babatunde A. Ogunnaike, Ph.D.
Dean of the College of Engineering

Approved: _____
Ann L. Ardis, Ph.D.
Senior Vice Provost for Graduate & Professional Education

I certify that I have read this dissertation and that in my opinion it meets the academic and professional standard required by the University as a dissertation for the degree of Doctor of Philosophy.

Signed: _____
Ioannis Poulakakis, Ph.D.
Professor in charge of dissertation

I certify that I have read this dissertation and that in my opinion it meets the academic and professional standard required by the University as a dissertation for the degree of Doctor of Philosophy.

Signed: _____
Herbert G. Tanner, Ph.D.
Member of dissertation committee

I certify that I have read this dissertation and that in my opinion it meets the academic and professional standard required by the University as a dissertation for the degree of Doctor of Philosophy.

Signed: _____
Ryan Zurakowski, Ph.D.
Member of dissertation committee

I certify that I have read this dissertation and that in my opinion it meets the academic and professional standard required by the University as a dissertation for the degree of Doctor of Philosophy.

Signed: _____
Fabrizio Sergi, Ph.D.
Member of dissertation committee

ACKNOWLEDGEMENTS

First of all, I would like to thank my advisor Prof. Poulakakis for having me as his first Ph.D student in the Robotic Locomotion Lab (RLL) and his exceptional vision, knowledge, patience and energy that carried me forward. I would also like to thank my committee members Prof. Tanner, Prof. Agrawal, Prof. Zurakowski and Prof. Sergi for their instrumental advices. In terms of funding, the research for this dissertation is supported by the Army Research Laboratory (ARL) through the contract W911NF-12-1-0117 and the National Science Foundation (NSF) through the grant CMMI-1130372.

It has been a great pleasure to work with the members in the Robotic Locomotion Lab. I thank Xin, Jian, Mohamad, Sushant and Duanyi for discussing legged locomotion with me. Special thanks to Anthom who produced preliminary results during his visiting at UD that make my work on gait transition possible.

Outside the lab, many people directly or indirectly contributed to my completion of this dissertation. I thank Chengkun for helping me settle down during my first days in Newark and Ying for assisting me getting the internship in GE. I thank my roommates Yuchen and Jun for creating the wonderful social setting to make the “village” life less boring. I thank my friends in the department Hang, Wenjie, Yupeng, Jiayin, Zeyuan, Weiju, Siqiang, Jianxin, Jie and Konstantinos for sharing their experience in learning, teaching and researching.

This thesis is dedicated to my family. I thank my grandparents and parents for always being proud of me. I thank my wife Zhuo for her constant support for my graduate study. Finally, I would like to thank Jelly, my domestic short-haired cat, for motivating my research as a quadruped.

TABLE OF CONTENTS

LIST OF TABLES	ix
LIST OF FIGURES	x
ABSTRACT	xvii
 Chapter	
1 INTRODUCTION	1
1.1 Motivation and Objectives	1
1.2 Contributions: A Modeling Hierarchy to Study Quadrupedal Running	2
1.3 Structure of This Dissertation	4
2 LITERATURE SURVEY	6
2.1 Quadrupedal Robots	7
2.1.1 Quadrupeds with Rigid Torsos	7
2.1.2 Quadrupeds with Segmented Torsos	8
2.2 Biological Observations: Benefits of Torso Compliance	9
2.3 Reduced-order Models of Legged Locomotion	11
2.3.1 A Canonical Example: Spring Loaded Inverted Pendulum	12
2.3.2 Quadrupedal Reduced-order Models with Rigid Torsos	13
2.3.3 Quadrupedal Reduced-order Models with Segmented Torsos	14
3 BACKGROUND ON BIOLOGY AND CONTROL	17
3.1 Biological Concepts	17
3.1.1 Quadrupedal Gaits	17
3.1.2 Dimensional Analysis	19

3.1.3	Cost of Transport	21
3.2	Mathematical Tools	22
3.2.1	Poincaré Return Map	22
3.2.2	Passive Stability	23
3.2.3	Virtual Holonomic Constraints	24
3.2.4	Domain of Attraction Estimates via Sums-of-Squares Programming	25
4	PASSIVELY STABLE QUADRUPEDAL RUNNING WITH A FLEXIBLE TORSO	27
4.1	A Passive and Energy-conservative Model	27
4.2	Bounding Gait	28
4.3	Hybrid Dynamics in a Non-dimensional Setting	28
4.3.1	Dynamics in Continuous-time	28
4.3.2	Event-based Transitions	31
4.3.3	Hybrid Dynamics of Bounding	32
4.4	Passively Generated Periodic Motions	34
4.4.1	Fixed Points and Their Properties	34
4.4.2	Continua of Symmetric Fixed Points	38
4.5	Local Stability	40
4.5.1	Coordination of Torso and Leg Spring Stiffness	41
4.5.2	Other Physical Parameters	43
5	FEEDBACK CONTROL OF QUADRUPEDAL BOUNDING	45
5.1	Overview of the Hybrid Controller	46
5.2	Continuous-time Control	47
5.2.1	Stance Phases	48
5.2.2	Flight Phases	49
5.3	Discrete-time Control	50
5.4	Disturbance Rejection	50
5.4.1	Unexpected Ground Height Variations	51

5.4.2	Domain of Attraction	52
6	GAIT TRANSITIONS BETWEEN PRONKING AND BOUNDING	56
6.1	General Scheme	56
6.2	Descriptions of Pronking and Bounding Gaits	57
6.3	Passively Generated Motions	58
6.4	Feedback Control	60
6.4.1	An Extended Gait Description	60
6.4.2	Hybrid Controller	60
6.5	Gait Transition	62
6.5.1	Estimation of Domain of Attraction	63
6.5.2	Transitions Between Pronking and Bounding	66
7	ENERGETICS OF QUADRUPEDAL BOUNDING	68
7.1	Non-dimensional Reduced-order Models	68
7.1.1	Continuous-time Dynamics in Non-dimensional Form	69
7.1.2	Event-based Transitions	72
7.1.3	Hybrid Dynamics of Bounding	73
7.2	Generation of Efficient Bounding Motions	73
7.2.1	Leg Recirculation Control	74
7.2.2	Poincaré Return Map	79
7.3	Methods: Searching for Fixed Points	79
7.3.1	Mechanical Cost of Transport	80
7.3.2	Metabolic Cost of Transport	80
7.3.3	Optimization	82
7.4	Results: Mechanical COT	82
7.4.1	Comparison of the Mechanical COT	82
7.4.2	Torso Oscillation and Energy Efficiency	84

7.4.3	Other Parameters	86
7.5	Results: Metabolic COT	88
7.5.1	Animal Data and Computations	89
7.5.2	Discussion	92
7.5.3	Metabolic and Mechanical COTs	97
8	EXTENSIONS TO HIGHER-DIMENSIONAL MODELS	100
8.1	Model	100
8.2	Hybrid Dynamics of Bounding	101
8.3	Leg Recirculation: Generating Periodic Motions	101
8.3.1	Designing the Constraints	102
8.3.2	Poincaré Map	104
8.3.3	Local Stability	105
8.4	Leg-torso Coordination: Stabilizing Periodic Motions	105
8.4.1	Continuous-time Control	107
8.4.2	Discrete-time Control	108
8.5	Speed Transitions	109
8.5.1	Estimation of Domain of Attraction	110
8.5.2	Realization of Speed Transitions	112
9	CONCLUSIONS AND FUTURE WORK	115
9.1	Conclusions	115
9.2	Perspectives on Future Work	116
9.2.1	Experimental Validation	116
9.2.2	Extension of Modeling Work	117
	BIBLIOGRAPHY	120
	Appendix	
	REPRINT PERMISSIONS	133

LIST OF TABLES

4.1	Non-dimensional Physical Parameters	34
5.1	Mechanical Parameters of the Model	46
7.1	Non-dimensional Parameters	72
7.2	Non-dimensional Mechanical Parameters of the Models	83
7.3	Non-dimensional Physical Parameters of Certain Animals	90
7.4	Average deviation of model-predicted metabolic COT from animal data	94
8.1	Mechanical Parameters of the Model	101

LIST OF FIGURES

1.1	Modeling hierarchy of quadrupedal bounding with a flexible torso. Center: a three-dimensional virtual prototype. (a): an energy-conservative template used to generate self-stable motions ; (b): the template in (a) with input at the torso joint to enlarge the domain of attraction. (c): the template in (a) with non-trivial leg mass and hip actuation to examine the effect of torso compliance on running efficiency; (d): the model in (c) with a control input at the torso joint to realize stable bounding motions.	3
2.1	Running horse and cheetah; the pronounced torso motion allows the cheetah to cover approximately as much ground as the horse in a single stride. Reproduced by [58] with permission.	10
2.2	The SLIP model used to describe running. In the first part of the stance phase the leg compresses and energy is stored in the spring; this energy is returned in the second part of the stance, when the body is lifted and accelerated. Figure adopted from [97].	12
3.1	Gait diagram of some common quadrupedal running gaits, plotted based on information from [60]. LP, LA, RA and RP represent the left posterior, left anterior, right anterior and right posterior legs, respectively. A back bar means that the corresponding leg is in contact with the ground.	18
3.2	An illustration of Poincaré map for a continuous-time system $\dot{x} = f(x)$	23
4.1	A sagittal-plane bounding model with a segmented torso.	28
4.2	Bounding phases and events.	29

4.3	Evolution of the cartesian variables and pitch angles with respect to time at a representative fixed point for the posterior (red continuous lines) and the anterior (blue dashed lines) parts of the torso. The vertical lines correspond to the events; from left to right: anterior leg touchdown, anterior leg liftoff, posterior leg touchdown, and posterior leg liftoff.	35
4.4	Evolution of the configuration variables of the legs. (a) Leg length, l^* . (b) Absolute angle γ^* defined with respect to the vertical; see Fig. 4.1. The red continuous lines correspond to the posterior leg, the blue dashed lines to the anterior leg. The vertical lines signify the events as in Fig. 4.3.	36
4.5	Evolution of the torso bending angle computed as $\theta_a^* - \theta_p^*$ for fixed point with one (Fig. 4.5(b)) and multiple (Fig. 4.5(c)) torso flexion-extension oscillations. The labels in Fig. 4.5(b) correspond to the sequence of phases in Fig. 4.5(a). From (a) to (h): apex height, anterior leg touchdown, torso flat, anterior leg liftoff, minimum torso bending, posterior leg touchdown, torso flat and posterior leg liftoff.	36
4.6	Bounding fixed points at different total energy levels; 5.4, 6.0 and 6.6. The vertical axis corresponds to the (absolute) touchdown angles of the posterior (upper branch) and anterior legs (lower branch), γ_p^{td*} and γ_a^{td*} , respectively. The horizontal axis corresponds to the range of torso oscillation, see Fig. 4.5(b). The points are colored according to the average velocity computed as the ratio of the stride length over the stride period. The red stars correspond to fixed points with $Fr = 1.75$ obtained at different total energies. As the total energy increases, the star “moves” to larger torso oscillation regions, which implies that maintaining the same forward speed at higher total energies results in more pronounced torso oscillations.	38
4.7	Energy distribution at the apex height of the spinal joint for fixed points with total energy $E_t = 6.0$. The horizontal axis corresponds to the (absolute) touchdown angles of the posterior (right branch) and anterior legs (left branch). The vertical axis corresponds to the energy distribution among the modes of the motion.	39
4.8	Fixed points computed for the same total energy ($E_t^* = 7.95$), average speed ($Fr = 2.41$) and hopping height ($y_{tj}^* = 0.82$) and for different values of dimensionless leg and torso stiffness. The color code corresponds to the values of the spectral radius of A	42

4.9	The paths of the six eigenvalues for constant dimensionless leg stiffness κ_{leg} as the dimensionless torso stiffness κ_{torso} varies (Fig. 4.9(a)) and for constant dimensionless torso stiffness κ_{torso} as the dimensionless leg stiffness κ_{leg} varies (Fig. 4.9(b)). The numbers show the points at which the eigenvalues start and “x” the points at which they terminate. In all cases, the eigenvalue denoted by “6” remains at one due to the conservative nature of the system. All the fixed points correspond to the same (dimensionless) total energy ($E_t^* = 7.95$), average speed ($Fr = 2.41$) and hopping height ($y_{\text{tj}}^* = 0.82$).	42
4.10	The relationship between the stiffness of the leg and torso springs for fixed points computed for the same (dimensionless) total energy ($E_t = 7.95$), average forward speed ($Fr = 2.41$) and hopping height ($y_{\text{tj}}^* = 0.82$) with (a) same relative hip-to-COM distance but different relative moment of inertia and (b) same relative moment of inertia but different relative hip-to-COM distance. The color code corresponds to the values of the spectral radius of A . The black points represent the passively stable fixed points.	44
5.1	Feedback diagram representing the structure of the hybrid controller. Continuous lines represent signals in continuous time; dashed lines represent signals in discrete time. The shaded block denotes the subsystem created via the feedback control in the continuous time. The discrete-time control action ensures that the resulting subsystem is locally exponentially stable.	47
5.2	The relative torso pitch angle $\theta_a - \theta_p$ as a function of the leg angle φ_p and φ_a in the posterior (a), and the anterior (b) stance. The monotonic relation allows to coordinate the torso oscillation with the leg sweeping motion through a virtual holonomic constraint.	49
5.3	Snapshots of the model’s motion as it runs down a step of 7.2cm (20% of the nominal leg length).	51
5.4	Response of the system to a step-down disturbance of 7.2cm showing convergence to the nominal orbit. (a) Hopping height; (b) Forward velocity; (c) Total energy. The red squares represent the apex height in the gathered flight and the green dotted lines represent the final values.	51
5.5	(a) The input of the torso joint actuator. (b) Horizontal (red continuous) and vertical (blue dotted) components of ground reaction force. For clarity, only the first six strides are presented.	53

5.6	<p>(\dot{x}_{t_j}, y_{t_j}) cross section of the domain of attraction towards the passive periodic motion when the maximum torque of the torso actuator does not exceed 50Nm. The green, blue and red area correspond the passive system, closed-loop system without consideration of double stance phase and close-loop systems with double stance phase, respectively.</p>	54
6.1	<p>A conceptual illustration of the transition between two different limit cycles, i.e., ϕ_0 and ϕ_1, which in legged locomotion could correspond to periodic motions of different gaits, for instance, pronking and bounding in this study. \mathcal{S}_0 and \mathcal{S}_1 are the Poincaré sections of ϕ_0 and ϕ_1, and \bar{z}_0 and \bar{z}_1 are the corresponding fixed points. \mathcal{D}_0 and \mathcal{D}_1 are the domain of attractions at the Poincaré sections for ϕ_0 and ϕ_1, respectively.</p>	57
6.2	<p>(a) Pronking gait; (b) Two variations of bounding gait.</p>	58
6.3	<p>The apex height (a), posterior pitch angle (b) and posterior pitch rate (c) of the fixed points corresponding to pronking (blue square), bounding without double stance (green triangle) and bounding with double stance (red circle) at speed $[1, 4]$m/s.</p>	59
6.4	<p>Extended description of the gaits in the presence of perturbation for pronking (a), bounding with double stance (b) and bounding without double stance (c). The shaded phases are the augmented phases and the dotted lines represent the possible evolution in presence of perturbation.</p>	61
6.5	<p>Fixed points that can be driven to a target fixed point (blue) within the bounding gait with double stance. The brown points are tested using the simulation-based method while the red points are predicted by the Lyapunov-SOS method.</p>	65
6.6	<p>The transition between pronking and bounding without double stance in the $(\theta_p, \dot{\theta}_p)$ section. The blue square, red circle and green triangles represent the fixed points corresponding to pronking, bounding without double stance and bounding with double stance, respectively. The black arrows show one of the transition routes. The grey area represents the projection of the domain of attraction on the $(\theta_p, \dot{\theta}_p)$ plane.</p>	66

7.1	Two sagittal-plane quadrupedal models used to study the energetics of bounding motion. (a) Rigid-torso model; (b) Flexible-torso model. The red arrows at the hip joints represent actuator inputs. In the flexible-torso model, the torso joint is not actuated.	69
7.2	Summary of the control actions in different phases. From left to right: anterior stance, gathered flight, posterior stance and extended flight. The arrows at the hip joints signify the application of torque and the blue, red and black colors of the leg springs correspond to the hip actuation patterns that are employed at different phases: (i) The blue color implies that the corresponding hip joint is passive. (ii) The red color means that a swing-leg retraction controller is applied at the corresponding hip joint. (iii) The black color indicates that the absolute leg angle of the corresponding leg is selected as the controlled variable, $q_{c,i}$, in (7.13) to enforce coordination between the motion of the legs.	75
7.3	The mechanical COT of flexible-torso (blue circles) and rigid-torso (red squares) models of different speeds and relative hip-to-COM distances. The continuous lines are fitted third degree polynomials.	83
7.4	Absolute (red) and relative (blue) leg angles for a bounding gait at $Fr = 3.0$ with $d = 0.42$ for rigid-torso (a, b), and flexible-torso (c, d) models. The dotted line represent the stance phase. The discontinuity in leg angle rate is due to the impacts at touchdown.	85
7.5	Power of the posterior (blue) and anterior actuators (red) in one stride of the rigid-torso model (a) and the flexible-torso model (b). The vertical lines separate the four phases; from left to right: flight-gathered (fg), stance-posterior (sp), flight-extended (fe), and stance-anterior (sa).	86
7.6	The stride frequency (a, b, c) and stride length (d, e, d) of flexible-torso (blue circles) and rigid-torso (red circles) models at different speed and relative hip-to-COM distance. The continuous lines are fitted 3rd-order polynomials.	87
7.7	(a) The relationship between the torso stiffness and the mechanical COT at different speeds. The black dots are the projections of the points with minimal mechanical COT. (b) The relationship between the torso stiffness and the stride frequency at different speeds. . . .	88

7.8	COT of the flexible-torso model with relative leg mass $M_{\text{leg}} \in \{0.1, 0.15, 0.2, 0.35\}$, $d = 0.38$ and $k_{\text{tor}} = 5.5$. Note that $M_{\text{leg}} := m_{\text{leg}}/m$	89
7.9	The metabolic COT computed by (3.4) using oxygen consumption measurements (magenta filled symbols in both Fig.s) and the corresponding model-predicted values at different running speeds. (a) Flexible-torso model (blue open symbols); (b) Rigid-torso model (red open symbols). Four animal species are considered in the analysis; cheetah (circles), dog (diamonds), horse (triangles) and gazelle (squares). The metabolic COT values for the “test” model are represented by green stars. In both figures, the error bars signify the standard variation of the model-predicted data due to the range of the parameter values considered in the corresponding computations.	93
7.10	The stride length and the non-dimensional stride frequency of the energy efficient motions corresponding to the horse (a, b) and the dog (c, d) in Fig. 7.9. The animal data is represented by magenta filled symbols while the values predicted by the flexible torso and the values predicted by the rigid-torso are represented by blue and red symbols, respectively.	95
7.11	The comparison of mechanical COT and metabolic COT for the flexible-torso (blue) and rigid-torso (red) models with the dog and horse physical parameters. The square pattern represents the mechanical COT. The diagonal pattern represents the increased value in COT when considering the efficiency of the actuators. The dot pattern represents the contribution of the non-ideal springs in the metabolic COT. The sum of these three component constitutes the metabolic COT shown in Fig. 7.9(a) and Fig. 7.9(b). The metabolic COT estimated based on animal data is represented by diamonds for the dog and by triangles for the horse, as in Fig. 7.9.	97
8.1	Evolution of forward velocity (a), torso oscillation (b), absolute leg angles (c) and hip joint torque (d) of a fixed point. In (c) and (d), the red and blue lines correspond to the anterior and posterior legs, respectively. The vertical lines separate one cycle into four phases: from left to right, fg, sp, fe and sa. The discontinuities are due to the impact at touchdown.	106
8.2	The evolution of the forward velocity and the anterior pitch angle when the system is perturbed with $+0.1\text{m/s}$ in \dot{x}_p and -3deg in θ_a	109

8.3	Ratio of the largest tolerable single perturbation predicted by the SOS method to their nominal values obtained through simulation for the presentative fixed point. The red and blue bars correspond to the positive and negative disturbances, respectively.	111
8.4	Transition between fixed points \bar{z}_0 , \bar{z}_1 and \bar{z}_2 of different running speeds. $\mathcal{D}_{0,\dot{x}_p\dot{y}_p}$, $\mathcal{D}_{1,\dot{x}_p\dot{y}_p}$ and $\mathcal{D}_{2,\dot{x}_p\dot{y}_p}$ are the projection of their estimated domain of attraction on the (\dot{x}_p, \dot{y}_p) planes when they are only perturbed in this plane. The blue line represents the transition from \bar{z}_1, \bar{z}_2 to \bar{z}_0 while the red line represents the transitions from \bar{z}_1 to \bar{z}_0 . The dotted red line represents a “shortcut” in transition from \bar{z}_2 to \bar{z}_1	113
8.5	Two routes of transition from \bar{z}_2 to \bar{z}_1 in Fig. 8.4.	113
9.1	The manufactured leg [75]. A cable-pulley system is used to move the knee actuator more close to the hip axis. The engagement of the leg spring in the system dynamics is controlled by a chain-lock mechanism.	117
9.2	A pseudo three-dimensional model that can be used to study trotting and galloping gaits. Both the left (red) and right (blue) limbs will swing in the sagittal plane.	118

ABSTRACT

A series of quadrupedal robots with different morphologies has been developed in the past forty years to explore the enhanced mobility such platforms may offer. The majority of these robots incorporate rigid, non-deformable torsos, a feature that distinguishes them from their counterparts in the animal world, which owe much of their remarkable locomotion abilities to their flexible bodies. Biological research indicates that torso flexibility may contribute to increased running speed, reduced energy cost and improved gait stability. This thesis proposes a modeling hierarchy that incorporates biological observations within a series of models with increasing complexity, and develops systematic feedback control algorithms for highly dynamic quadrupedal running motions that harness torso flexibility and compliant legs.

On a macroscopic level, reduced-order models, or “templates”, can capture the dominant features of an observed locomotion behavior without delving into the fine details of a robot’s (or animal’s) structure and morphology. Templates provide unified, platform-independent descriptions of the desired locomotion task, and they have proved to be indispensable in designing legged robots and in synthesizing controllers for stabilizing highly-agile locomotion behaviors. One representative example is the *Spring Loaded Inverted Pendulum* (SLIP), which, despite its very simple structure, captures the evolution of kinetic and potential energy associated with running motions, and has informed controller design of many legged robots. However, because of its simple lumped point-mass structure, the SLIP and its immediate extensions cannot describe some of the common quadrupedal gaits that involve pronounced torso oscillations, such as bounding and galloping.

Motivated by the capability as well as the limitations of SLIP-type templates, a number of reduced-order quadrupedal models that incorporate non-point-mass torsos

has been proposed in the relevant literature to investigate quadrupedal running. However, partly because of the need to describe the torso morphology of the corresponding hardware platforms, and partly because of the need to simplify running dynamics, most of these quadrupedal templates only consider non-deformable, rigid torsos. Although, a few studies with preliminary results on running with torso compliance can be found in the relevant literature, studies on the conditions for generating periodic locomotion behaviors are rather limited while the stability properties of these motions are not carefully examined. As a result, feedback controller design in the presence of torso compliance has not been carefully investigated. Beyond stability and control design, the energetic cost of transport of quadrupedal running and, in particular, the contribution of torso flexibility to running efficiency, has not received adequate attention.

This thesis aims at proposing a modeling and control hierarchy that enables the systematic evaluation of the role of torso compliance in quadrupedal running. The proposed templates have different modeling complexities and actuation schemes, and can be used to facilitate the investigation of a number of key issues in quadrupedal running, such as motion generation, gait stability, feedback design, gait transitions and energy efficiency. Through careful analysis of the models, a series of useful conclusions can be drawn; these conclusions pave the way toward synthesizing feedback control laws for legged robots with torso and leg compliance, and provide insight into designing robotic platforms that harness elastic elements to realize high-performance, reliable and natural-like quadrupedal running motions.

Chapter 1

INTRODUCTION

1.1 Motivation and Objectives

Due to their requirement for continuous contact with the ground, traditional wheeled or tracked vehicles have limited mobility when it comes to rough terrain with extreme slopes, obstacles and other terrain discontinuities. Legged robots, on the other hand, have the potential to provide access to challenging terrain by exploiting the enhanced mobility offered by legs, which use discrete footholds to handle terrain discontinuities. In this class of robots, quadrupeds provide a good tradeoff among stability, load-carrying capacity and mechanical complexity.

Raibert and his collaborators were the first to develop actively-balancing legged robots, including quadrupeds [104]. In the same vein, examples of quadrupedal robots include Scout II [100], Tekken [41], BigDog [107] and HyQ [120]. In striking contrast to their counterparts in nature—which owe much of their remarkable locomotion performance to their flexible torsos and limbs—running robotic quadrupeds always incorporate rigid, non-deformable torsos. Exceptions to this general rule are rare. Quadrupedal robots specifically designed to run with an articulated torso first appeared in the mid-90s with the work of Leeser [74]. Contemporary examples include Canid [53], MIT Cheetah [71] and Bobcat-robot [70], which all adopt a segmented morphology in the torso.

Much of the work on how torso flexibility affects locomotion performance has been developed in the context of biomechanics. Research in biomechanics indicates that torso flexibility may enhance locomotion performance in a number of ways; e.g., by increasing traveling speed [58, 59], by reducing the cost of transport in high-speed

asymmetric running gaits [4, 1], or by improving gait stability through the effective implementation of self-stabilizing mechanisms [114, 51].

A series of questions arise from such intuitive bio-mechanical observations. For instance, can some if not all of these observations be unified in a single legged model? How can these observations be translated to systematic methods for feedback control design for quadrupedal robots with flexible torsos? Under what conditions torso compliance enhances energy efficiency in quadrupedal robots? To answer these questions, this thesis proposes a modeling and control framework to investigate quadrupedal running with torso compliance.

1.2 Contributions: A Modeling Hierarchy to Study Quadrupedal Running

This work investigates the implications of torso flexibility and leg compliance on quadrupedal running in a template setting. We explore a hierarchy of models with increasing complexity to probe the effect of compliance in the legs and torso to the generation, stability and energy efficiency of periodic quadrupedal running motions; see Fig. 1.1.

(1) Passively Generated Bounding and Passive Stability. Our analysis begins with a reductive sagittal-plane model with a segmented flexible torso and compliant massless legs, see Fig. 1.1 (a). For the first time, and despite the sensitive dependence of the motion on the torso’s dorsoventral oscillations, numerical return map studies reveal that a large variety of cyclic bounding motions can be realized passively, through the natural interaction of the model with its environment. More surprisingly, for certain combinations of the torso and leg stiffness self-stable bounding motions emerge.

(2) Feedback Control Synthesis based on Passive Dynamics. The implications of self-stable bounding orbits to control design are discussed in the context of a hybrid control law that uses one actuator located at the torso joint to actively coordinate the torso bending oscillations with the movements of the legs according to a targeted, passively generated gait. In the simple massless model of Fig. 1.1 (b),

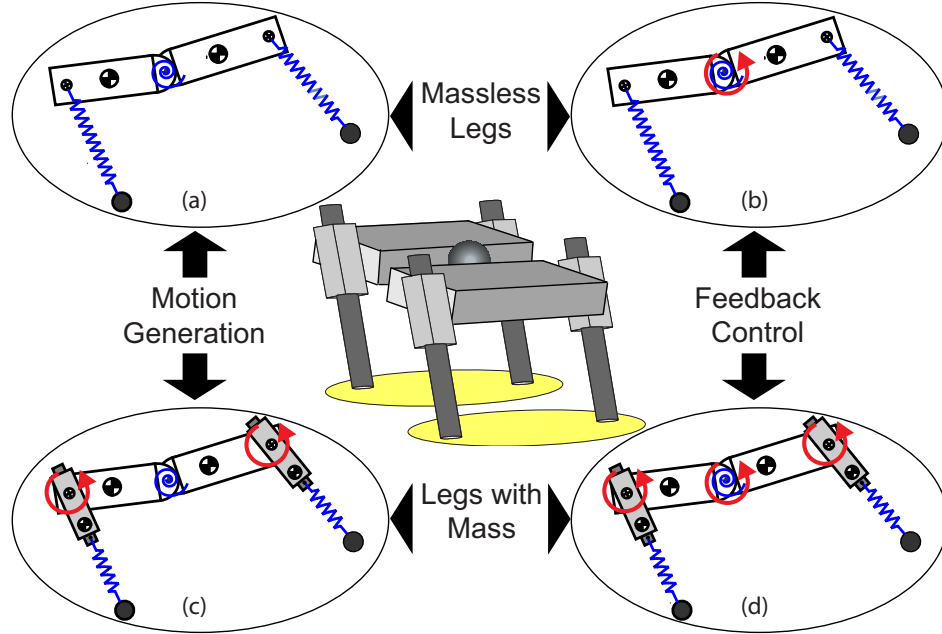


Figure 1.1: Modeling hierarchy of quadrupedal bounding with a flexible torso. Center: a three-dimensional virtual prototype. (a): an energy-conservative template used to generate self-stable motions ; (b): the template in (a) with input at the torso joint to enlarge the domain of attraction. (c): the template in (a) with non-trivial leg mass and hip actuation to examine the effect of torso compliance on running efficiency; (d): the model in (c) with a control input at the torso joint to realize stable bounding motions.

the torso actuator alone is sufficient to stabilize the four-degree-of-freedom (4-DOF) system, rejecting significantly large disturbances without excessive effort.

(3) Gait Transitions and Speed Transitions. The hybrid control framework can be extended to stabilize other quadrupedal running gaits as well, such as pronking. By estimating the domain of attraction of the fixed points corresponding to different gaits using sums-of-squares (SOS) programming, feasible transitions between these fixed points can be constructed to achieve gait transitions. Furthermore, in the higher-dimensional model with leg mass as in Fig. 1.1 (d), the same principle of coordinating the torso oscillations with the leg movements was also successful in producing stable bounding gaits. Through SOS programming the estimates of the domain of attraction of stable fixed points can be used to realize acceleration and deceleration by composing limit cycles that correspond to different running speeds in a sequential fashion.

(4) Energetics of Quadrupedal Running. To probe the relationship between elastic elements within the torso and energy consumption, the basic model is extended to include non-trivial mass in the legs, see Fig. 1.1 (c). By comparing the cost of transport with a rigid-torso model with the same leg mass, it is deduced that torso compliance significantly enhances energy efficiency, but *only* when the Froude number exceeds a particular value. Furthermore, by considering non-ideal torque generating and compliant elements with efficiency values corresponding to those of muscles and tendons, it is shown that the flexible-torso model can predict the metabolic cost of transport for different animals estimated using measurements of oxygen consumption. This way, the proposed model offers a simple means for approximating the energetic cost of transport of running quadrupeds in a simple and direct fashion.

1.3 Structure of This Dissertation

The remainder of this dissertation is organized in eight chapters.

Chapter 2 provides a brief overview of the related work on quadrupedal robots and reductive locomotion models for running behaviors, highlighting the contribution of the work presented in the thesis. Chapter 3 reviews the biological concepts and mathematical tools that are used in this thesis to study legged locomotion.

Chapter 4 introduces a reduced-order passive and conservative model with a segmented flexible torso and compliant legs. The model is used to study conditions under which cyclic bounding motions can be generated. The existence of self-stable cyclic bounding gaits in the presence of torso flexibility is examined. It is found that self-stable bounding gaits can be passively generated through appropriate combinations of the stiffness of the torso and the stiffness of the legs. The implications of this result to control design are then discussed in Chapter 5, and a hybrid controller is proposed to enhance the stability of the passively generated bounding gaits. Chapter 6 extends this control framework to controlling pronking motions and investigates the transitions between pronking and bounding by examining the domain of attraction of the associated motions at the Poincaré section using sums-of-squares programming.

Chapter 7 examines the influence of torso compliance on the energy efficiency of quadrupedal running with a bounding gait. The models feature non-trivial leg mass and inertia, and are coupled with a simple leg recirculation controller to generate bounding motions. Despite their simplicity, the proposed models are sufficiently expressive to capture the energetics of bounding motions and to assess the contribution of torso flexibility to gait efficiency measured by the cost of transport (COT). Furthermore, despite the simple structure of the model and the inaccuracy with which certain model parameters can be identified from animal data, it is remarkable that the metabolic COT predicted by the flexible-torso model is in good agreement with the COT estimated using oxygen consumption measurements of different quadrupedal running animals.

Chapter 8 studies the control of speed transitions through the composition of fixed points. Based on the control of the passive, energy-conservative model in Chapter 5, a hybrid controller that coordinates the movement of the torso and the legs and updates touchdown angles is developed to stabilize the system. The domain of attraction of each bounding motion is estimated analytically using the sums-of-squares technique. By examining the feasibility of convergence from the source fixed point to the target fixed point, transitions between these fixed points are constructed to achieve various running speeds.

Finally, Chapter 9 provides conclusions and remarks on future directions relevant to this work.

Chapter 2

LITERATURE SURVEY

In this chapter, results in the relevant literature that motivate and support the work presented in this thesis are provided. Section 2.1 briefly discusses the development of quadrupedal robots that can perform dynamic running motions. The biological observations that motivate the introduction of torso compliance in the quadrupedal robots are given in Section 2.2.

In parallel with the development of robotic platforms, substantial efforts have been devoted into developing models that can capture and quantify the mechanisms that underlie locomotion, which are reviewed in Section 2.3. As an illustrative example, the *Spring Loaded Inverted Pendulum* (SLIP) has been employed to design controllers that realize stable running motions to various many legged robots. On the other hand, its limitations in capturing the torso dynamics in bounding and galloping are discussed in Section 2.3.1, motivating the introduction of reduced-order models for quadrupedal running.

The majority of existing quadrupedal models possess rigid, non-deformable torsos. As evidenced in Section 2.3.2, only a few models have considered torso articulation and flexibility¹ while none of the models proposed so far can capture the effect of torso compliance on gait stability in a way that can be used to inform controller design. Another aspect that has not received adequate attention in the study of these models is the evaluation of the contribution of torso compliance to energy economy. These

¹ Note that articulation or segmentation does not necessarily imply flexibility or compliance at the torso. In this thesis, flexibility or compliance refers to elastic elements, such as springs, that are incorporated into the system's structure.

shortcomings of existing quadrupedal models set the stage for the work presented in this thesis.

2.1 Quadrupedal Robots

Since Raibert’s pioneering work in dynamic legged robots [104], a variety of quadrupedal robots with different actuation and control schemes has been introduced. Depending on the morphology of the torso, these quadrupedal robots can be divided into two groups: one with rigid, non-deformable torso and the other with segmented, flexible torso.

2.1.1 Quadrupeds with Rigid Torsos

The vast majority of the quadrupedal robots that have been built possess rigid, non-deformable torsos. In the early work of Raibert [104], pneumatic actuators periodically feed energy into the system to compensate the energy loss due to friction and impacts. By combining the front, the back or the diagonal pair of legs into a *virtual* leg, various symmetric gaits, such as trotting, pacing and bounding were realized on the same quadrupedal platform using a three-part controller. The purpose of the controller is to regulate the forward speed, hopping height and torso posture of the robot. In particular, forward speed is regulated by suitably placing the feet at touchdown, and hopping height is controlled by tuning the energy injected into the pneumatic pistons that radically actuate the legs during stance. Finally, torso attitude is regulated in trotting and pacing by employing the hip torques of the legs in stance. Interestingly, Raibert and his collaborators found that active torso stabilization is not required in bounding when the torso is properly designed [88].

Subsequent quadrupedal robots exploiting similar control algorithms include Scout II [100], KOLT [38] and BigDog [107]. Scout II made maximum use of the passive dynamics associated with its prismatic springy legs, each of which is controlled only by a single actuator located at the hip joint. By changing the touchdown angles during flight and the hip torques during stance, bounding [100] and galloping motions

[101] can be generated. On the other hand, in the KOLT quadruped [38], each leg was actuated by two motors; one responsible for hip rotation and the other for knee flexion through a cable. The robot has been able to pronk and trot when the forward speed was controlled by Raibert’s method and the body pitch was regulated by the leg thrust control. More recently, BigDog exhibited impressive rough-terrain mobility using controllers that combine Raibert’s approach with virtual model control ideas [107].

Other design and control approaches for dynamically stable running robots have also been proposed. Fukuoka *et al.* [41] proposed a controller based on a Central Pattern Generator (CPG) that alters its active phase based on sensory feedback, and results in adaptive dynamic walking on irregular terrain using the Tekken robot. On the other hand, an open-loop CPG network was adopted to generate trotting motions in the Cheetah-cub robot [129]. The oscillator network only relies on inter-oscillator coupling without external sensory feedback, and its output determines the position of each joint of the robot. Recently Semini *et al.* combined a CPG network with actively impedance control to realize trotting on the HyQ robot [121]. The CPG network was modified to generate a half-ellipse-shaped trajectory of each leg. In a different vein from CPG-based controllers, StarLETH [63] was able to perform a walking trot gait using an optimization-based controller, which decomposes the complex walking behavior into a simple set of least squares problems with different priorities for motion, torque, and force optimization. Recently, Park *et al.* [91] combined force control and (virtual) compliance control to generate stable bounding motions in MIT Cheetah 2 robot. By suitably planning the desired ground reaction force profile, the robot was able to change the running speed over a wide range of values while handling variations in ground height and stiffness [91, 94].

2.1.2 Quadrupeds with Segmented Torsos

Compared with quadrupedal robots with rigid torsos, only a limited number of robotic quadrupeds that incorporate segmented torsos exist. Leeser of MIT’s Leg

Lab was the first to test torso articulation in generating bounding motions using a planar quadrupedal robot [74]. Actuated segmented-torso configurations have also been studied in [53, 70, 17]. In more detail, in the Canid robot [53], the actuators are placed in parallel with a leaf spring, intended to actively tune the flexion/extension oscillations of the torso. However, due to the difficulty in regulating the motion of the torso, the robot in its current design was not able to sustain continuous running motion. The Bobcat-robot [70] features a re-configurable torso design; the segmented, actuated torso can be changed into a rigid torso by locking a pin at the spinal joint. By comparing the cost of transport of these two torso configurations in bounding generated by a CPG network, it was concluded that torso actuation does not improve energy efficiency. Recently, Boston Dynamics released a video [17] of their hydraulically actuated Cheetah robot galloping at the record speed of 29 mph, demonstrating the potential of realizing fast quadrupedal running motions through a segmented torso. However—to the best of the authors’ knowledge—only limited information on how torso bending movements affect locomotion is available in the context of this platform.

In contrast to the aforementioned robots which incorporate independent actuation to excite the oscillation of the torso, the MIT Cheetah robot [71] employs a differential mechanism to couple the motion of its flexible torso with the back legs, when these legs move in phase as in bounding. Using an impedance control strategy to actively tune the virtual leg springs, the robot is able to trot at high speeds, albeit without the use of torso flexibility; in trotting the two back legs move out of phase, as a result the differential does not couple the legs to the torso which behaves as a rigid one.

2.2 Biological Observations: Benefits of Torso Compliance

The design of quadrupedal robots with flexible-torso is inspired by biological research, which indicates that torso compliance improves the running performance. In the early work of Hildebrand on the running motion of horses and cheetahs [58], it was observed that the stride length of the cheetah at high-speed running is roughly

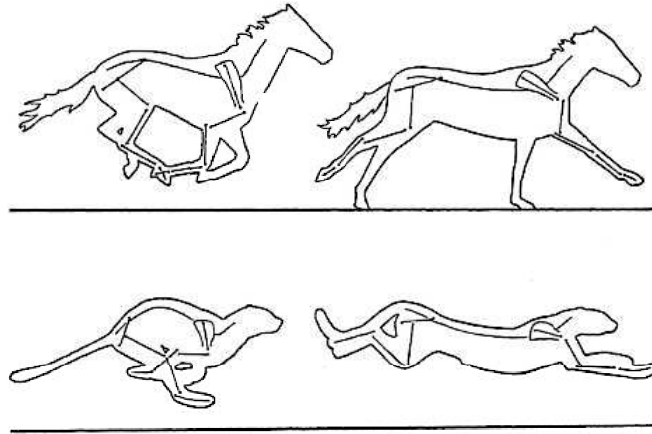


Figure 2.1: Running horse and cheetah; the pronounced torso motion allows the cheetah to cover approximately as much ground as the horse in a single stride. Reproduced by [58] with permission.

the same as that of the horse, despite the fact that its legs are much shorter than the legs of the horse, see also Fig. 2.1. By comparing the torso movement during running, Hildebrand deduced that the cheetah significantly increases its stride length by extending and flexing its flexible body so that it covers more distance during one stride. This work also provided a first phenomenological description of the coordination between the torso's sagittal movements and leg recirculation in running motion. That is, as the back legs liftoff the ground, the flexible body is extended during the flight in order to cover more distance, while before the front legs leave the ground, the body is flexed, preparing for the next body extension.

The flexibility in the torso has also been studied in the context of energy. Alexander [4] analyzed the evolution of external and internal energy² associated with quadrupedal running motions, concluding that elastic elements located in animals' back can store and release part of the kinematic energy required to recirculate the legs, thereby reducing the energy cost. To explain this energy-saving mechanism in a model setting, Alexander [1] proposed a simple model comprised of an articulated torso and

² External kinetic energy is the the energy due to the movement of center of mass (COM) while internal kinetic energy is the energy due to the movement of parts of the body relative to the COM.

massless legs. However, examination of the internal kinetic energy fluctuations associated with the torso movement lead to the conclusion that additional power will be required to maintain this motion, thereby not confirming Alexander’s original hypothesis [4]. To clarify these conflicting observations, part of this thesis focuses on assessing the contribution of torso flexion-extension oscillations to the energy economy of running by considering the energy associated with recirculating the legs with nontrivial mass and inertia.

The coordination between the torso oscillation and the leg movement not only benefits running quadrupedal animals in terms of energy efficiency; it also enhances gait stability. Recent studies on the half-bounding motion of the Pika [51] suggested that the flexion-extension of the torso promotes gait stability through the effective implementation of a “self-stabilizing” mechanism that relies on adjusting the angle and angular rate of a leg prior to its touchdown [123].

The potential benefits offered by torso compliance have not been extensively studied in the context of quadrupedal robots; for, these platforms either do not employ compliant elements in their torsos, or the physical properties of the compliant torso are not suitably combined with those of the legs. As a first step toward quantifying the contribution of torso compliance on quadrupedal running, we propose a hierarchy of models that can unify many of the biological observations described here, and can be used to inform the design and control of high-performance robotic platforms that take advantage of torso-flexibility to produce reliable, natural-like running motions.

2.3 Reduced-order Models of Legged Locomotion

On a macroscopic level, legged locomotion can be understood through the introduction of reduced-order models, or “templates” [42], the purpose of which is to capture the dominant features of an observed locomotion behavior without delving into the fine details of a robot’s (or animal’s) structure and morphology [36]. Such models provide unified, platform-independent descriptions of the desired locomotion

task, and they have proved to be indispensable in designing legged robots, and in synthesizing controllers for stabilizing highly agile locomotion behaviors [104].

2.3.1 A Canonical Example: Spring Loaded Inverted Pendulum

An important example of a reductive locomotion model is the *Spring Loaded Inverted Pendulum* (SLIP), which—in its most common configuration—consists of a point mass atop a springy, massless, prismatic leg [15], see Fig. 2.2. Notwithstanding its passive and conservative nature, the SLIP has been instrumental in reducing the complexity associated with the neuromechanical coordination producing running in animals [82, 16], and in devising empirical control strategies for a diverse set of running robots, including Raibert’s machines [104]. The success of the SLIP as a canonical model of running prompted a series of studies—see [46, 12] and references therein—revealing several properties with significant implications to control. Among these properties, the existence of self-stable running orbits—observed independently by [123] and [47]—was effectively used by [124] to realize robust running motions on the SLIP using a simple swing leg retraction policy.

Even though the SLIP has been useful in the control of robot models with different postures and leg numbers—see [113], [112], and [10] for example—it cannot

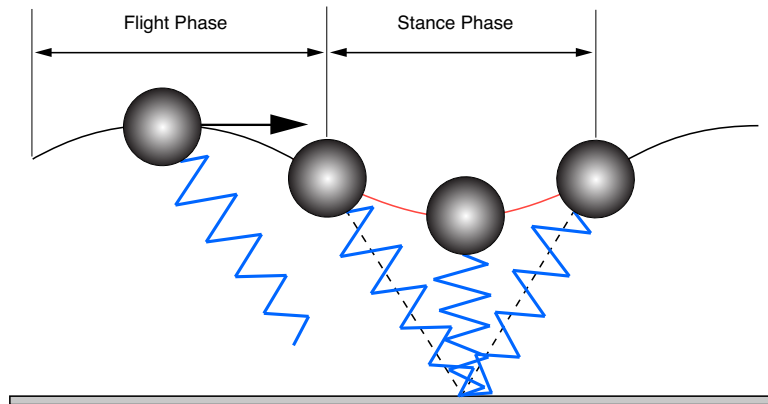


Figure 2.2: The SLIP model used to describe running. In the first part of the stance phase the leg compresses and energy is stored in the spring; this energy is returned in the second part of the stance, when the body is lifted and accelerated. Figure adopted from [97].

capture the interactions between the movement of the torso and the movement of the legs in common quadrupedal gaits, such as galloping and bounding [16]. In their early work, Raibert *et al.* [106] also observed that the legs in bounding cannot be organized to form a virtual leg that places the effective point of support close to the torso’s COM; see [87] and [104, p.193]. As a result, the models cannot be reduced to a SLIP and Raibert’s original three-part controller that regulates the system’s high-level behavior through the virtual leg, had to be modified to control bounding.

2.3.2 Quadrupedal Reduced-order Models with Rigid Torsos

Realizing the limitations of the SLIP as a template for quadrupedal running gaits like bounding, a series of quadrupedal models has been proposed. Guided by the structural form of the majority of existing robotic quadrupeds, the accompanying modeling efforts focus predominantly on systems with rigid, non-deformable torsos.

Focusing on the motion in the sagittal plane, Nanua and Waldron [89] proposed an energy-conservative bounding model with massless legs and found that cyclic trotting, bounding and galloping motions can be passively generated. A similar quadrupedal model was used in [98, 99] to interpret the success of minimalistic controllers on realizing bounding gaits on the Scout II quadruped [100]. Echoing the self-stability of the SLIP [123, 47], it was found that, for suitable parameters and initial conditions, the model was able to reject perturbations that do not alter its total energy passively. In a similar reductive setting, Zhang *et al.* [146] replaced the prismatic legs of the aforementioned models with segmented ones and found similar results, which were subsequently used in [147] to propose a control strategy that stabilizes a more representative model of the Tekken quadruped [41].

In parallel with the investigation of passive dynamics and its implications to controller design, efforts have also been devoted to evaluating the energetics of quadrupedal running. In the work of Nanua and Waldron [89], the energy cost of running is assumed to be proportional to the total kinetic energy and a performance index was formulated and minimized in order to compute energy-efficient bounding motions. However, the

assumption underlying the performance index – which was necessary given the conservative nature of the model – oversimplifies the computation of the actual energy required to compensate for friction and impact losses, as well as the energy needed to reposition the legs after liftoff [116]. As a consequence, the motions computed based on the aforementioned model differ significantly from natural bounding gaits. More complete, non-conservative, quadrupedal running models that incorporate non-trivial leg mass have been proposed in [73, 109] and the cost of transport (COT) is computed based on the positive work performed by ideal actuators. Partly because of this simplifying assumption, and partly because the metabolic COT of running animals encompasses a variety of internal phenomena that are difficult to model, the COT in [73] differs significantly from the one generated from animal data in [62]. On the other hand, Remy *et al.* [109] consider a quadrupedal model with series elastic actuators that apply inputs generated by Fourier series and compute running gaits that optimize a COT criterion; however, in the resulting gaits the legs undergo two retraction-protraction oscillations in a single stride, which is not common in animal and robot running.

2.3.3 Quadrupedal Reduced-order Models with Segmented Torsos

Quadrupedal reduce-order models with passive, unactuated torsos have been proposed [90, 35, 119, 145, 20] in order to investigate motion generation and passive dynamics. Nanua [90] introduced a sagittal-plane quadrupedal model with a passive flexible torso joint and massless springy legs. However, the difficulty associated with generating periodic motions in the context of this passive model lead to the conclusion that torso flexibility without actuation may render the realization of running motions overly complex. In [35], a quasi-passive model was introduced to generate bounding motions by assuming that the torso joint can be “locked” when it reaches its maximum flexion and extension.

Using a completely passive model, Seipel [119] investigated the possibility of generating bounding motions without actuation. The model used in this work corresponds to the particular geometry of two spring loaded inverted pendula connected

through a rotational spring, while the analysis is carried under conditions of reduced gravity. In [145], a damper is introduced in parallel with the torso spring and passively stable bounding were found when the robot runs down a slope. However, during one stride the torso undergoes two complete oscillation which are not common in animals' running. Very recently, Byl *et al.* [20] used a quadrupedal model with a passive flexible spine to exploit the improved stability by switching between different low-level gait controllers.

Except the models mentioned above, which have passive and unactuated torsos, quadrupedal models with segmented, actuated torso have also been studied in [34, 52]. In [34], the model includes springy legs with non-trivial mass and bounding was generated via PID control loops imposing desired values on the relative angle between the two segments of the torso. Optimization based on a modified version of the specific resistance that favors speed over efficiency resulted in bounding motions, which – in agreement with Alexander [1] – require more energy compared to a rigid-torso model. Contrary to these findings, it was deduced in [52] that an actuated torso can in fact improve gait efficiency, provided that high enough running speeds can be realized. However, this result was obtained under the simplifying assumption that energy is supplied or lost only at discrete instants during the gait and no comparisons with biological data was attempted.

Despite the many different models and the many different assumptions employed in evaluating the COT in quadrupedal running, the proposed approaches had limited success in producing results that are consistent with biological data. In part, this shortcoming may be attributed to the fact that none of the models discussed thus far incorporates torso flexibility. To the best of our knowledge, only [56] considers the effect of torso flexibility in the context of models for a galloping horse. They report metabolic COT computations based on an empirical rule proposed by [72], indicating good agreement with biological data of running horses extracted from the work in [62]. However, the model in [56] is “animal specific,” intended to capture the morphological characteristics of a horse, while manual tuning of the empirical rule

in [72] to estimate the metabolic energy was necessary to achieve agreement between simulation and experimental data.

To summarize, only preliminary results exist regarding the passive generation of dynamically-stable running motions in the presence of torso compliance. Furthermore, much less is known regarding the design of control laws that take advantage of torso compliance to provide enhanced disturbance rejection capabilities without the development of excessive corrective inputs. In addition, there has been limited success in providing models capable of predicting the energy cost of running in a way that is consistent with biological data; so far the potential contribution of torso compliance on energy economy has not been carefully examined. These observations set the stage of this research, which aims at proposing a modeling and control hierarchy that includes templates of different modeling complexities and actuation schemes and enables the systematic investigation of motion generation, gait stability, feedback design and energy economy in quadrupedal running with torso compliance.

Chapter 3

BACKGROUND ON BIOLOGY AND CONTROL

Before discussing the main results of this thesis, this chapter summarizes the concepts and mathematical tools that are essential to subsequent chapters. We begin with a classification of some relevant quadrupedal gaits. Then, dimensional analysis is reviewed as a method to provide general model descriptions. In particular, two important non-dimensional quantities are discussed in detail. The first one is the Froude number that captures forward speed and the second quantity is the cost of transport, which is used to evaluate the energy consumed in locomotion.

In the second part of this chapter, we provide some information on the mathematical tools commonly employed in the study of legged locomotion with a focus on stability. As a powerful tool for analyzing periodic motions, the Poincaré map is described in the context of a continuous-time system, and the implications of the linearization of the associated Poincaré map on the stability of the orbit are discussed. Then, the concepts of passive stability and virtual holonomic constraints for controller design are discussed. Finally, a brief overview of the use of SOS programming to quantify the stability of a system by estimating the domain of attraction of its equilibria is given.

3.1 Biological Concepts

3.1.1 Quadrupedal Gaits

The term “gait” is used to describe the movement pattern of an animal’s legs. In the context of quadrupeds, depending on the footfall sequence of the legs and the time intervals they are in contact with the ground, several running gaits can be distinguished as shown in Fig. 3.1.

At low speeds, the *pronking* gait is used by some animals, such as mule-deer and springboks. In this gait, all the legs will leave and touch the ground at the same time. *Trotting*, on the other hand, uses the diagonal pair of legs in unison and is adopted at moderate speeds. Gaits of high speed include *bounding*, and *galloping*. In bounding the two anterior (front) or posterior (back) legs move simultaneously. Depending on whether the anterior pair of legs touch down before the posterior pair leave the ground, two variations of bounding can be defined. In the first variation, which is referred as *bounding with double stance*, the posterior leg touchdown occurs before the anterior leg lift off, thus there is a part of the cycle when both legs are in stance. In the second variation, which is called *bounding without double stance*, the posterior leg touchdown happens after the anterior leg liftoff, thus the posterior and anterior stance phases are separated by a double flight phase. In galloping, the legs touch down the ground in a sequential manner. Galloping can be further divided into *transverse galloping* and

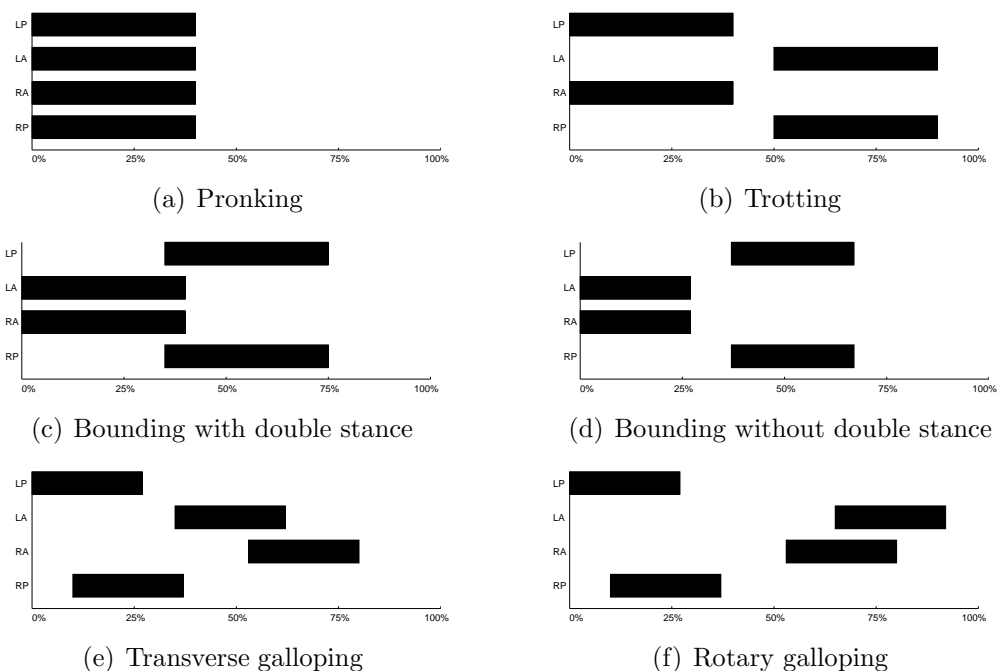


Figure 3.1: Gait diagram of some common quadrupedal running gaits, plotted based on information from [60]. LP, LA, RA and RP represent the left posterior, left anterior, right anterior and right posterior legs, respectively. A back bar means that the corresponding leg is in contact with the ground.

rotary galloping. In transverse galloping, the leading limbs of the front and back legs are at different sides (one on the left and one on the right) while in rotary galloping the leading limbs are at the same side (both on the left or right).

Each gait pattern is used only over a limited range of speeds and switching among gaits occurs at specific speeds [62] to reduce the metabolic cost [62, 5] or the bone stress [14, 40] of the animal. Inspired by the footfall pattern, Raibert first realized switching from trotting to pacing by changing the legs to touch down the ground during the flight phase at low speeds [105]. Subsequent research in robotics concentrated – almost exclusively – on realizing gait transitions via neural-inspired control schemes [135, 134, 111, 11], with central pattern generators (CPGs) [64] as a common theme. By tuning the phase difference between the legs, transitions between walking and trotting have been realized in several quadrupedal robots [135, 134, 111, 11]. Yet, the generated motions are not dynamic.

In the modeling aspect, though a series of quadrupedal models has been proposed to study quadrupedal running in a reductive setting [89, 146, 99, 45], the majority of these models study gaits individually; a model can perform one or several types of gaits, but transitions among these gaits are not typically investigated.

3.1.2 Dimensional Analysis

Non-dimensionalizing the equations of motion has been widely used in biology and biomechanics to formulate unifying descriptions of locomotion behaviors and to study the effects of scaling on locomotion of animals with different morphology. An important dimensionless quantity that is used to capture the interplay between kinetic energy and gravitational potential energy is the Froude number, which is defined as:

$$Fr := \frac{\bar{v}}{\sqrt{gl_0}} \quad (3.1)$$

where \bar{v} [m/s] is the average running speed, g [m/s²] is the gravitational acceleration and l_0 [m] is the characteristic length often selected as the nominal length of the leg¹. At the same Froude number, animals tend to use the same gait, similar relative stride lengths and duty factors, and exert similar patterns of force on the ground [6], which is referred as *dynamic similarity*. In the same spirit, the physical properties of animals can be formulated in a non-dimensional setting. For instance, despite significant differences in size and morphology, most animals have a relative leg stiffness, defined as

$$\kappa_{\text{leg}} := \frac{k_{\text{leg}} l_0}{mg} \quad (3.2)$$

between 7 and 27 [16, 61]. In (3.2), k_{leg} [N/m] is the dimensional stiffness of the leg², m [kg] is the mass of the animal and l_0 [m] is the length of the leg. Recently, work of Shen and Seipel [126, 125] on an actuated-SLIP model indicates that this preferred range of leg stiffness may help minimizing the energy cost and improving gait stability.

In modeling legged systems, dimensionless quantities facilitate parametric studies by reducing the number of the physical parameters involved in the differential equations that govern the dynamics of such systems. For example, Murphy and Raibert [87] found that the stability of bounding depends on the ratio of the non-dimensional moment of inertia of the torso I , which is defined as $I := J/(mL^2)$, where m [kg] is the mass of the torso, J [kgm²] is the moment of inertia of the torso and L [m] is the distance from the hip joint to the center of mass of the torso. In more detail, when $I < 1$ the attitude of the torso can be passively stabilized in bounding. On the other hand, when $I > 1$ the motion cannot be stabilized in an open-loop fashion and active control is required. An analysis of Murphy’s conclusion can be found in the work of

¹ Another common definition of the Froude number is $\bar{v}^2/(gl_0)$, which is the square of the definition in (3.1).

² The leg stiffness k_{leg} of animals can be empirically determined as the ratio of peak ground reaction force F_{GRF} to the maximum compression of the leg Δl , i.e., $k_{\text{leg}} := F_{\text{GRF}}/\Delta l$. In quadrupedal robots with compliant legs, the leg stiffness is simply the stiffness of the spring [100] for prismatic legs or can be derived based on the leg geometry for segmented legs [110, 75].

Berkemeier [13], who utilized the method of Poincaré to examine the local stability of bounding. More complete parametric studies in terms of stability of bounding have been conducted by Chatzakos *et al* [28], showing that—in addition to the dimensionless moment of inertia—the dimensionless leg stiffness is also crucial for maintaining passively generated bounding motions. These observations provide an example of how dimensional analysis can be used to facilitate the mechanical design of quadrupedal robots, as we will see in Chapter 4.

3.1.3 Cost of Transport

Energy economy is important to both animals and robots. When covering long distances, it is hypothesized that animals tend to move in a manner that minimizes effort [2]. On the other hand, power-autonomous legged robots need to minimize energy consumption in order to maximize operation time [122]. To quantify efficiency in legged locomotion the *cost of transport (COT)*³ has been widely employed; the COT is a dimensionless quantity that measures the total energy required to move a unit weight over a unit distance [136, 62, 32], i.e.,

$$c = \frac{P}{mg\bar{v}} \quad (3.3)$$

where P [W] is the average power, m [kg] is the mass of the animal or the robot, g [m/s²] is the gravitational acceleration and \bar{v} [m/s] is the average speed.

In animal locomotion the COT is always referred to as metabolic COT (c_{mt}) and it can be calculated from data on the mass-specific rate of oxygen consumption given the energy produced by a unit volume of oxygen and the corresponding running speed as in [84], i.e.,

$$c_{\text{mt}} = \frac{V_{\text{O}_2} E_{\text{O}_2}}{mg\bar{v}} \quad , \quad (3.4)$$

where V_{O_2} [ml/s] is the rate of oxygen consumption, m [kg] is the mass of the animal, g [m/s²] is the gravitational acceleration and \bar{v} [m/s] is the average running speed. The

³ An alternative to the COT metric of energy expenditure in locomotion is the specific resistance introduced in [43].

energy produced per unit volume of oxygen consumed, E_{O_2} , is approximately equal to 20.1J/ml according to [54] and [84].

3.2 Mathematical Tools

3.2.1 Poincaré Return Map

To determine the existence and stability properties of periodic motions, the classical Poincaré return map method is frequently used. For simplicity, in what follows, we review the definition of Poincaré return map, and its indication in the stability of the periodic motion in the context of a continuous-time system [68]; the extension of the method to hybrid systems can be found in [142].

In Fig. 3.2, let ϕ be a periodic orbit of a n -th dimensional system $\dot{x} = f(x)$ of period T . Pick a point p on ϕ and let \mathcal{H} be an $(n - 1)$ -dimensional hyperplane at p , i.e., $\forall x \in \mathcal{H}$, there exists some $a \in \mathbb{R}^n$ such that⁴ $a'(x - p) = 0$. Suppose that the hyperplane is transversal to ϕ at p ; that is $a'f(x) \neq 0$. Let $\mathcal{U} \subset \mathcal{H}$ be a sufficiently small neighbourhood of p such that ϕ intersects \mathcal{U} only at p . Then the Poincaré return map $\mathcal{P} : \mathcal{U} \rightarrow \mathcal{H}$ is defined for a point $x \in \mathcal{U}$ as

$$\mathcal{P}(x) = \Phi(\tau(x), x) \tag{3.5}$$

where $\Phi(\tau, x)$ is the solution of $\dot{x} = f(x)$ and $\tau(x)$ is the time it takes the trajectory starting at x to return to \mathcal{H} the first time. Note that $\tau(x)$ depends on x and need not be equal to T , which is the period of ϕ . However, $\tau(x) \rightarrow T$ as $x \rightarrow p$. Suppose for all $x \in \mathcal{U}$, the map can be defined. Then starting with $x[0] \in \mathcal{U}$, let $x[1] = \mathcal{P}(x[0])$. If $x[1] \in \mathcal{U}$, the Poincaré map can be defined at $x[1]$. Iterating this process, if $x[k] \in \mathcal{U}$,

$$x[k + 1] = \mathcal{P}(x[k]) \ . \tag{3.6}$$

Equation (3.6) is a discrete-time nonlinear system, which describes the evolution of the system as it crosses the hyperplane \mathcal{H} . Given (3.6), the problem of finding periodic

⁴ Notation: to avoid cluttering, hereafter we denote the transpose of a vector x by x' instead of the commonly used symbol x^T

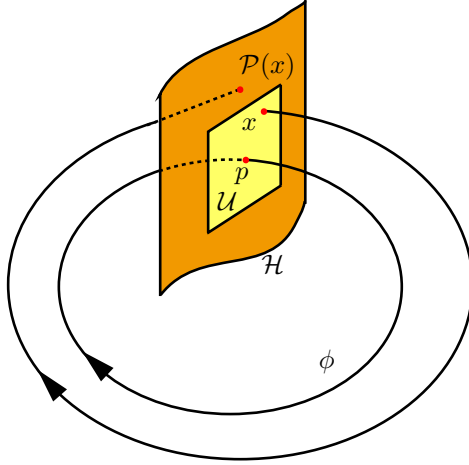


Figure 3.2: An illustration of Poincaré map for a continuous-time system $\dot{x} = f(x)$.

motion reduces to searching an equilibrium point (also referred to as a fixed point) of (3.6),

$$x - \mathcal{P}(x) = 0 \quad (3.7)$$

Clearly, p is a fixed point of (3.6) since it maps to itself after one period.

The stability of the periodic orbit ϕ can be characterized by the stability of the discrete-time system (3.6); if the equilibrium point of (3.6) is asymptotically stable, then the corresponding periodic orbit ϕ is asymptotically stable. To analyze the local stability of the Poincaré map, we can linearize (3.6) at the fixed point, resulting in

$$\Delta x[k + 1] = A\Delta x[k] \quad (3.8)$$

where $\Delta x = x - p$ and

$$A = \left. \frac{d\mathcal{P}}{dx} \right|_{x=p}. \quad (3.9)$$

When all the eigenvalues of A are within the unit disc, the corresponding fixed point p is locally exponentially stable.

3.2.2 Passive Stability

Passive stability was first investigated by McGeer, who also built passive dynamic walkers that were able to walk on an incline [81] *without* any actuation input,

merely by the gravitational force. This principle was later extended to develop a passive dynamic walker that can walk stably in three dimensions [33]. In the spirit of passive bipedal walker, a combined rimless wheel model was introduced in [127] to study passive quadrupedal walking on an incline. However, based on the physical parameters in that work, quadrupedal walking motions were found to be unstable. Recent work by Remy [108] introduced a “wobbling” mass elastically attached to the torso and stable passive walking was achieved by tuning the inertia and stiffness properties.

In parallel with passively-stable walking, passively-stable running motions have been systematically investigated in [123, 100, 146, 28]. Using the SLIP, it was found in [123] that passively generated running motions can be stable when a minimum running speed is exceeded for certain leg stiffness and fixed touchdown angles. Furthermore, the stability can be enhanced by introducing articulation in the legs [110]. Similarly to the SLIP, the work in [98, 99] revealed that passively stable quadrupedal bounding gaits can be computed at sufficiently high running speed (4m/s) using a planar bounding model with a rigid torso. More detailed analysis on the relationship between passive stability and the physical properties of the model and the extension to segmented legs can be found in [28, 146]. Note, however, passive stability of bounding has not been studied in models with torso flexibility. By conducting a thorough parametric study in a non-dimensional setting, this dissertation shows that passively generated bounding motions can be stable if the physical properties of the torso and the legs are suitably coordinated.

3.2.3 Virtual Holonomic Constraints

Virtual holonomic constraints are functional relations among the configuration variables of a robot or a model. By imposing virtual holonomic constraints through feedback control, such as PID control with feedback linearization [65], the evolution of certain joint angles can be synchronized based on a single internal “clock”. The “clock” essentially corresponds to a monotonically increasing function of the configuration variables, which can be used to replace time in defining the desired evolution of

the joint angles.

Previous analytical and experimental work has shown that virtual holonomic constraints are a powerful means to synchronize the links of a bipedal robot to achieve walking and running motions over a variety of terrain profiles [48, 144, 142, 130, 93, 19]. In this work, we will extend this method to controlling quadrupedal running motions. Inspired by the observation that the passive stability of bounding is very sensitive to the physical properties of the torso and the legs, virtual constraints are selected to (asymptotically) enforce a coordination pattern between the oscillation of the flexible torso and the movement of the legs in order to enhance stability.

3.2.4 Domain of Attraction Estimates via Sums-of-Squares Programming

The domain of attraction associated with a locally asymptotically stable equilibrium point is an invariant set such that all the trajectories starting inside this set will finally converge to the equilibrium point [68]. Computing exactly the domain of attraction is generally intractable for nonlinear systems even at low dimensions. An alternative is to obtain a compact *estimate* of the domain of attraction as a sublevel set of a Lyapunov function [138, 31, 55, 29]. In more detail, a Lyapunov function is utilized to characterize the local stability of the equilibrium point and its sub-level sets correspond to invariant subsets of the domain of attraction. In the case of polynomial systems, establishing that a function is a valid Lyapunov function reduces to checking the uniform positive (or negative) definiteness of a polynomial over a region of state space. This procedure can be formulated and solved efficiently by a sums-of-squares optimization program.

A multivariate polynomial $h(x) := h(q_1, \dots, q_n)$ is a sum of squares if there exist polynomials $f_1(x), \dots, f_m(x)$ such that

$$h(x) = \sum_{i=1}^m f_i^2(x) \tag{3.10}$$

Condition (3.10) is equivalent to the existence of a positive semidefinite matrix H such that

$$h(x) := Z'(x)HZ(x) \tag{3.11}$$

where $Z(x)$ is a suitably chosen vector of monomials. For a given polynomial, a sums-of-squares program will check the non-negativity of the polynomial $h(x)$ by searching for a positive semidefinite matrix H .

With recent advances in the sums-of-squares programming [66, 133, 30, 69] and the development of software packages [102, 76], it is possible to search for a Lyapunov function when the system dynamics is in polynomial form. If not, an approximation of the dynamics can be obtained using Taylor expansion [79, 132, 85, 78].

Chapter 4

PASSIVELY STABLE QUADRUPEDAL RUNNING WITH A FLEXIBLE TORSO

This chapter examines the passive dynamics of quadrupedal bounding in the presence of torso compliance. Sections 4.1 to 4.3 derive the hybrid dynamics of bounding in a dimensionless setting. In Section 4.4, numerical return map studies of the system reveal that a large variety of cyclic bounding motions can be realized passively, through the natural interaction of the model with its environment. Section 4.5 shows that for certain combinations of the system parameters—in particular the torso and leg relative stiffness—self-stable bounding motions emerge.

4.1 A Passive and Energy-conservative Model

To study the effect of a segmented flexible torso on bounding in a template setting, the sagittal-plane model depicted in Fig. 4.1 is introduced; see also Fig. 1.1 (a) and [21]. In this model, the torso consists of two identical rigid bodies; one represents its posterior (caudal) and the other its anterior (cranial) part. The two rigid bodies are connected via a rotational spring, intended to introduce flexibility in the segmented torso. At this stage, we concentrate on how the targeted gait behavior can be generated passively; that is, through the natural interaction between the model and its environment. Therefore, input motor torques and energy dissipation forces acting in continuous time are not considered. Such assumptions are common in relevant work on the SLIP [118, 123, 47] and on the passive generation of bounding in rigid-torso quadrupeds [98, 146, 28]. Models of this kind are useful in explaining locomotion phenomena in a general, platform-independent context [116].

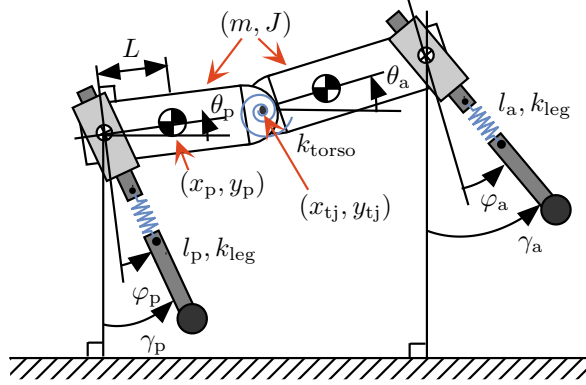


Figure 4.1: A sagittal-plane bounding model with a segmented torso.

4.2 Bounding Gait

For brevity, in this chapter we restrict our attention to bounding gait without double stance as shown in Fig. 4.2, see also Fig. 3.1. Depending on the state of a leg—stance or flight—we distinguish the following phases: the double flight phase, denoted by “f,” in which both legs are in the air; the stance-posterior phase, denoted by “sp,” in which the posterior leg is on the ground; and the stance-anterior phase, denoted by “sa,” in which the anterior leg is on the ground. Finally, the flight phase after the anterior leg liftoff will be termed gathered; during this phase the torso assumes a concave configuration. Similarly, the flight phase after the posterior leg liftoff will be called extended; during this phase the torso assumes a convex configuration.

4.3 Hybrid Dynamics in a Non-dimensional Setting

4.3.1 Dynamics in Continuous-time

In modeling the dynamics of the system in Fig. 4.1, it is assumed that both parts of the torso have mass m and moment of inertia J about their center of mass (COM), and that the hip-to-COM distance is L . The stiffness of the rotational spring connecting the two parts of the torso is denoted by k_{torso} and the stiffness of the virtual legs by k_{leg} . The toe-ground interactions are modeled as unactuated, frictionless pin joints.

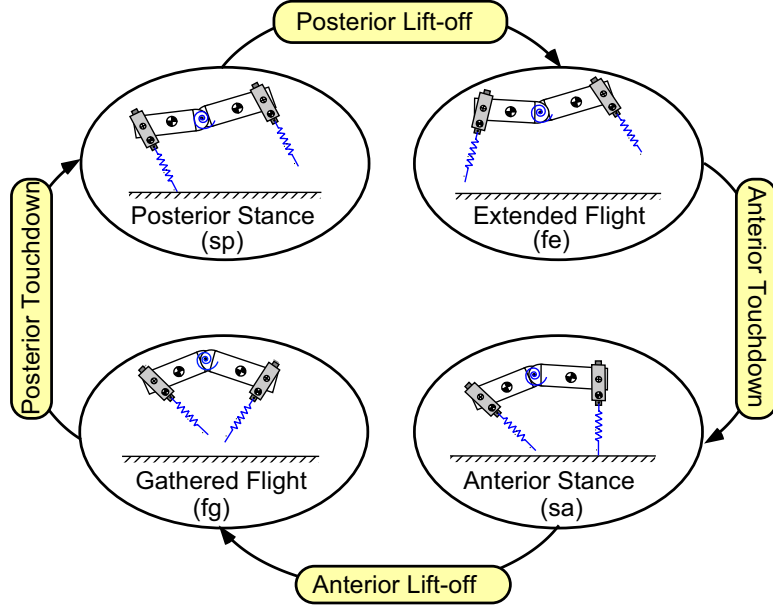


Figure 4.2: Bounding phases and events.

For the stance phases $i \in \{\text{sp}, \text{sa}\}$, the configuration space Q_i can be parameterized by the length $l_i \in \mathbb{R}$ of the leg in contact with the ground and its relative angle $\varphi_i \in \mathbb{S}^1$ with respect to the torso, together with the pitch angles $\theta_p \in \mathbb{S}^1$ and $\theta_a \in \mathbb{S}^1$ of the posterior and anterior parts of the torso, respectively; i.e.,

$$q_i := \begin{cases} (l_p, \varphi_p, \theta_p, \theta_a)' \in Q_i, & \text{for } i = \text{sp}. \\ (l_a, \varphi_a, \theta_p, \theta_a)' \in Q_i, & \text{for } i = \text{sa}. \end{cases} \quad (4.1)$$

The configuration space Q_f of the extended and gathered flight phases is parameterized through the cartesian coordinates $(x_p, y_p) \in \mathbb{R}^2$ of the COM of the posterior part of the torso, its pitch angle $\theta_p \in \mathbb{S}^1$, and the pitch angle $\theta_a \in \mathbb{S}^1$ of the anterior part of the torso; i.e.,

$$q_f := (x_p, y_p, \theta_p, \theta_a)' \in Q_f. \quad (4.2)$$

Through the method of Lagrange [128], the equations of motion can be derived in all phases, and they can be written in state-space form as

$$\dot{x}_i = f_i(x_i), \quad (4.3)$$

evolving in $TQ_i := \{x_i := (q'_i, \dot{q}'_i)' \mid q_i \in Q_i, \dot{q}_i \in \mathbb{R}^4\}$ for $i \in \{f, \text{sp}, \text{sa}\}$.

It is important to note that the equations of motion depend on the following six physical parameters

$$\{m, J, l_0, L, k_{\text{torso}}, k_{\text{leg}}\}, \quad (4.4)$$

which capture the effects of the geometry, inertia and stiffness properties of the system. In (4.4), l_0 is the natural length of the legs corresponding to an uncompressed spring; the rest of the parameters have been defined above—see also Fig. 4.1.

In what follows, we apply dimensional analysis to transform the dynamics of the system in non-dimensional form. In this form, the parameters (4.4) that characterize the solutions of (4.3) reduce to a smaller number of dimensionless quantities, allowing us to explore efficiently a large fraction of the solution space. This is crucial to computing self-stable bounding motions in Section 4.5.

By defining the characteristic length as l_0 and characteristic time scale τ as

$$\tau := \sqrt{\frac{l_0}{g}}, \quad (4.5)$$

where g is the gravitational acceleration, the dimensionless time becomes

$$t^* := \frac{t}{\tau}, \quad (4.6)$$

and the configuration variables in (4.3) and their time derivatives obtain the non-dimensional form

$$\zeta^* := \frac{\zeta}{l_0}, \quad \dot{\zeta}^* := \frac{\tau \dot{\zeta}}{l_0}, \quad \ddot{\zeta}^* := \frac{\tau^2 \ddot{\zeta}}{l_0}, \quad (4.7)$$

for $\zeta \in \{x_p, y_p, l_p, l_a\}$ and

$$\psi^* := \psi, \quad \dot{\psi}^* := \tau \dot{\psi}, \quad \ddot{\psi}^* := \tau^2 \ddot{\psi}, \quad (4.8)$$

for $\psi \in \{\varphi_p, \varphi_a, \theta_p, \theta_a\}$ where the superscript “*” denotes a dimensionless quantity.

Substitution of (4.7) and (4.8) to (4.3) for $i \in \{f, p, a\}$ reduces the six parameters in (4.4) to the following four dimensionless parameter groups:

- Relative moment of inertia:

$$I := \frac{J}{mL^2}. \quad (4.9)$$

- Relative hip-to-COM distance:

$$d := \frac{L}{l_0}. \quad (4.10)$$

- Relative leg stiffness:

$$\kappa_{\text{leg}} := \frac{k_{\text{leg}} l_0}{mg}. \quad (4.11)$$

- Relative torso stiffness:

$$\kappa_{\text{torso}} := \frac{k_{\text{torso}}}{mg l_0}. \quad (4.12)$$

In this non-dimensional setting, the continuous-time dynamics of the system for each $i \in \{\text{f}, \text{p}, \text{a}\}$ becomes

$$\frac{d}{dt^*} x_i^* = f_i^*(x_i^*), \quad (4.13)$$

where $x_i^* := ((q_i^*)', (\dot{q}_i^*)')'$ are the dimensionless counterparts of the states in (4.3) as were defined by (4.7) and (4.8). It is emphasized that (4.13) does not depend on the choice of units.

4.3.2 Event-based Transitions

The succession of the continuous-time phases occurs according to Fig. 4.2. The phases are separated by touchdown and liftoff events that are modeled through suitable threshold functions as described in the section.

Flight-to-stance Transitions. The flight phase terminates when the vertical distance between the toe of either the posterior or the anterior leg and the ground becomes zero. To realize this condition, the flight state vector is augmented with the parameter array

$$\alpha_{\text{f}}^* = (\gamma_{\text{p}}^{\text{td}*}, \gamma_{\text{a}}^{\text{td}*})', \quad (4.14)$$

with $\alpha_{\text{f}}^* \in \mathcal{A}_{\text{f}}^*$, an open subset containing the angle of the posterior and the anterior leg with respect to the vertical at touchdown; see Fig. 4.1. It is assumed that the length of both legs at touchdown is equal to its nominal value, l_0 , that corresponds to the uncompressed length of the spring. Hence, the threshold function

$$H_{\text{f} \rightarrow \text{sp}}(x_{\text{f}}^*, \alpha_{\text{f}}^*) = y_{\text{p}}^* - d \sin \theta_{\text{p}}^* - \cos \gamma_{\text{p}}^{\text{td}*} \quad (4.15)$$

signifies the touchdown event of the posterior leg at its zero crossing. Similarly, the zeroing of

$$H_{f \rightarrow sa}(x_f^*, \alpha_f^*) = y_p^* + d \sin \theta_p^* + 2d \sin \theta_a^* - \cos \gamma_a^{\text{td}*} \quad (4.16)$$

defines the touchdown event of the anterior leg.

Stance-to-flight Transitions. Generally, transitions from stance to flight can be triggered by causing the acceleration of the stance leg end to be positive—that is, directed upwards—when the ground force becomes zero. Due to the assumption of massless legs, the stance-to-flight condition can be simplified so that liftoff occurs when the stance leg, as it extends, obtains its natural length. Consequently, the zero crossing of the threshold function

$$H_{sa \rightarrow f}(x_{sa}^*) = 1 - l_a^*, \quad \dot{l}_a^* > 0, \quad (4.17)$$

signifies the transition from the stance-anterior to the flight phase, while the threshold function

$$H_{sp \rightarrow f}(x_{sp}^*) = 1 - l_p^*, \quad \dot{l}_p^* > 0, \quad (4.18)$$

defines the posterior leg liftoff at its zeroing.

4.3.3 Hybrid Dynamics of Bounding

The dynamics of the bounding gait considered here can be described by concatenating the continuous-time phases according to the sequence of Fig. 4.2. Assuming that the bounding phases are executed in a fixed order $f \rightarrow sa \rightarrow f \rightarrow sp \rightarrow f$ and that two consecutive phases are denoted as i and $i + 1$, the *hybrid dynamics* of bounding can be written as

$$\Sigma : \begin{cases} \dot{x}_i^* = f_i^*(x_i^*), & x_i^{*-} \notin \mathcal{S}_{i \rightarrow i+1}^*, \\ x_{i+1}^{*+} = \Delta_{i \rightarrow i+1}(x_i^{*-}), & x_i^{*-} \in \mathcal{S}_{i \rightarrow i+1}^*, \\ \mathcal{S}_{i \rightarrow i+1}^* = \{x_i^* \in \mathcal{X}_i^* \mid H_{i \rightarrow i+1}(x_i^*) = 0, \dot{H}_{i \rightarrow i+1}(x_i^*) < 0\}, \end{cases} \quad (4.19)$$

where $x_{i+1}^{*+} = \Delta_{i \rightarrow i+1}(x_i^{*-})$ maps the states at the end of a phase to the states at the beginning of the following phase, and for the conservative model of Fig. 4.1 they

represent coordinate changes. Note more generally, impacts can be captured by these mappings when the mass of the leg is nontrivial.

To study the existence and stability of such gaits, the method of Poincaré is used [49]. The Poincaré section is taken at the apex height of the spinal torso joint in the extended flight phase. At this instant, the vertical velocity of the torso joint is equal to zero, and the Poincaré section is defined by

$$\mathcal{S}_{\text{apex}}^* := \left\{ (x_f^*, \alpha_f^*) \in \mathcal{X}_f^* \mid \dot{y}_p^* + L\dot{\theta}_p^* \cos \theta_p^* = 0, \theta_a^* > 0 \right\}, \quad (4.20)$$

where $\mathcal{X}_f^* := TQ_f^* \times \mathcal{A}_f^*$. As in [7] and [99], the monotonically increasing horizontal coordinate x_p^* of the COM of the posterior part of the torso will be projected out of the state vector x_f^* . A further dimensional reduction inherent to the Poincaré method [49] can be used to substitute \dot{y}_p^* through the condition defining $\mathcal{S}_{\text{apex}}^*$ in (4.20). Hence¹, if $\pi : \mathcal{X}_f^* \rightarrow \mathcal{Z}_f^*$ denotes the operator that projects x_f^* onto its non- (x_p^*, \dot{y}_p^*) components, the (reduced) Poincaré map $\mathcal{P}^* : \pi(\mathcal{S}_{\text{apex}}^*) \rightarrow \pi(\mathcal{S}_{\text{apex}}^*)$ can be defined through the rule

$$z_f^*[k+1] = \mathcal{P}^*(z_f^*[k], \alpha_f^*[k]), \quad (4.21)$$

where

$$z_f^* := (y_p^*, \theta_p^*, \theta_a^*, \dot{x}_p^*, \dot{\theta}_p^*, \dot{\theta}_a^*)', \quad (4.22)$$

the parameter array α_f^* is defined by (4.14) and $\pi(\mathcal{S}_{\text{apex}}^*)$ denotes the image of $\mathcal{S}_{\text{apex}}^*$ under π .

Equation (4.21) represents a nonlinear discrete-time control system. The explicit appearance of the touchdown angles in the right hand side of (4.21) is a consequence of the dependence of the threshold functions (4.15) and (4.16) on α_f^* . It is apparent from (4.21) that the touchdown angles are considered as inputs available for control since it is (in general) easy to place the legs during the flight phase.

¹ The dimension can be further reduced due to conservation of energy.

4.4 Passively Generated Periodic Motions

In this section, a number of passively generated fixed points corresponding to the cyclic bounding motions of interest is presented. First, the properties of a representative bounding cycle are discussed. Then, families of fixed points are computed to investigate their behavior at various energy levels, forward speeds, and torso bending oscillation amplitudes.

4.4.1 Fixed Points and Their Properties

The objective is to find an argument z_f^* in (4.21) that maps onto itself; this is equivalent to solving the equation

$$z_f^* - \mathcal{P}^*(z_f^*, \alpha_f^*) = 0, \quad (4.23)$$

for physically reasonable values of touchdown angles α_f^* . For concreteness, in this section we will use the non-dimensional physical parameters that roughly correspond to the morphology of the Scout II quadruped [100]; see Table 4.1. The search for fixed points is conducted numerically using MATLAB’s `fsolve`.

Table 4.1: Non-dimensional Physical Parameters

Parameter	Value
Relative Moment of Inertia (I)	1.8120
Relative Hip-to-COM Distance (d)	0.3833
Relative Leg Spring Stiffness (κ_{leg})	22.33
Relative Torso Spring Stiffness (κ_{torso})	5

A large number of fixed points has been computed for different initial guesses and different touchdown angles using the parameters in Table 4.1 and the procedure described above. Fig. 4.3 shows the evolution of the cartesian variables of the COM for both the posterior and anterior parts of the torso as well as the pitch angles and rates during one bounding cycle. The evolution of the configuration variables of each leg for the bounding cycle is presented in Fig. 4.4.

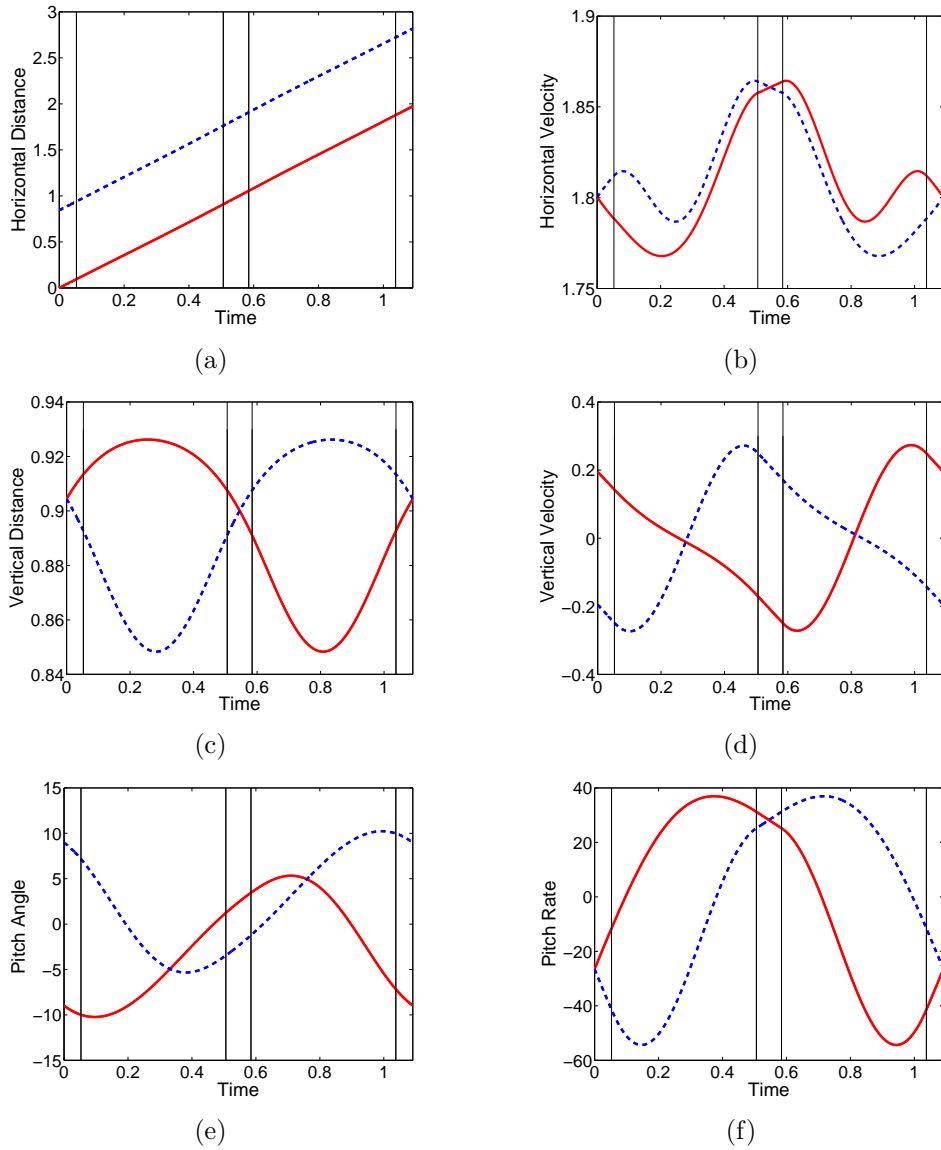


Figure 4.3: Evolution of the cartesian variables and pitch angles with respect to time at a representative fixed point for the posterior (red continuous lines) and the anterior (blue dashed lines) parts of the torso. The vertical lines correspond to the events; from left to right: anterior leg touchdown, anterior leg liftoff, posterior leg touchdown, and posterior leg liftoff.

It is of interest to describe in some detail the motion of the torso during a bounding cycle. Figure 4.5(a) presents snapshots of the bounding motion associated with the fixed point of Fig. 4.3, and Fig. 4.5(b) shows the corresponding evolution of the relative pitch angle, computed as the difference between the pitch angles of the

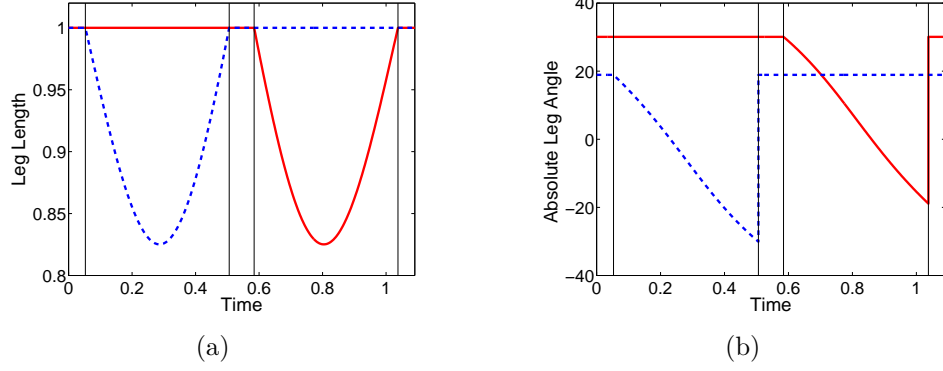
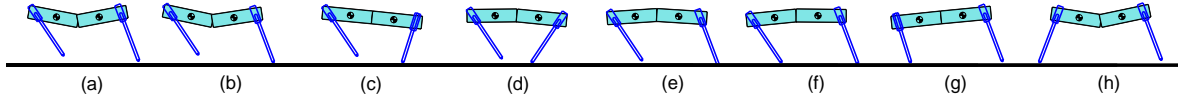
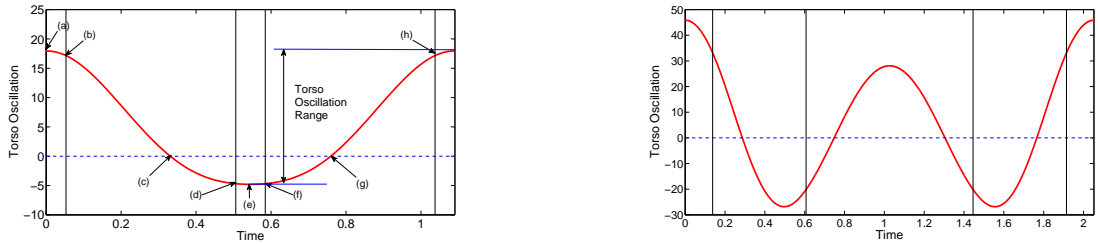


Figure 4.4: Evolution of the configuration variables of the legs. (a) Leg length, l^* . (b) Absolute angle γ^* defined with respect to the vertical; see Fig. 4.1. The red continuous lines correspond to the posterior leg, the blue dashed lines to the anterior leg. The vertical lines signify the events as in Fig. 4.3.



(a) Snapshots of the model during one bounding cycle. The letters refer to instants of interest as shown in Fig. 4.5(b)



(b) One torso flexion-extension oscillation within one stride

(c) Multiple torso flexion-extension oscillations within one stride

Figure 4.5: Evolution of the torso bending angle computed as $\theta_a^* - \theta_p^*$ for fixed point with one (Fig. 4.5(b)) and multiple (Fig. 4.5(c)) torso flexion-extension oscillations. The labels in Fig. 4.5(b) correspond to the sequence of phases in Fig. 4.5(a). From (a) to (h): apex height, anterior leg touchdown, torso flat, anterior leg liftoff, minimum torso bending, posterior leg touchdown, torso flat and posterior leg liftoff.

anterior and posterior parts of the torso; i.e., $\theta_a^* - \theta_p^*$. Effectively, the anterior and posterior leg stance phases “translate” the configuration of the torso from convex to concave and vice versa in order to prepare the system for the gathered and extended

flight phases, respectively. We remark that the maximum angular excursions of the torso do not appear to be tied to the touchdown events. As Fig. 4.5(b) shows, the maximum torso bending angle occurs at the middle of the extended flight phase denoted by (a), before the anterior leg touchdown. On the other hand, the minimum torso bending angle happens prior to the touchdown of the posterior leg, at the middle of the gathered flight phase denoted by (e). This is in agreement with observations on galloping mammals in [44] and [114], according to which maximum flexion of the spine occurs before the touchdown of the posterior leg, while maximum extension occurs prior to the touchdown of the anterior leg, contradicting Hildebrand’s original findings [58].

It should be emphasized that computing passively generated bounding motions that correspond to physically realistic torso bending oscillations—like those in Fig. 4.5(b)—is not an easy task. This difficulty has been pointed out in previous work by [90] and [35], and is attributed to the sensitive dependence of the motion on the combination between the torso stiffness and the leg stiffness. Even when fixed points can be computed—which is not always the case—they may correspond to spurious motions for which the torso exhibits multiple oscillations within a single stride. Fig. 4.5(c) presents an instance of such motions, which emerge when the leg stiffness and the torso stiffness are not properly tuned. This fact explains why bounding in the presence of a flexible torso has been studied only in actuated settings, with control laws that essentially enforce such motions on the system, thereby requiring the development of large input torques [34].

As a closing remark, note that all the bounding fixed points computed in this work exhibit some useful symmetry characteristics. Echoing the symmetry properties of fixed points corresponding to passively generated bounding motions on quadrupeds with rigid torso—see [99] for details—Fig. 4.4(b) shows that

$$\gamma_a^{\text{td}^*} = -\gamma_p^{\text{lo}^*} \text{ and } \gamma_p^{\text{td}^*} = -\gamma_a^{\text{lo}}. \quad (4.24)$$

In words, the (absolute) touchdown angle of the anterior leg is equal to the negative of

the (absolute) liftoff angle of the posterior leg, and vice versa. In fact, (4.24) reflects a more general property of the system. Careful inspection of Fig. 4.3 reveals that the evolution of the states of the anterior part of the torso (blue dashed lines in Fig. 4.3) *forward* in time is indistinguishable from the evolution of the states of the posterior part of the torso (red continuous lines in Fig. 4.3) *backward* in time. Mathematically, if $G = \text{diag}[1, -1, 1, -1, 1]$, then

$$S_p(-t^*) = G \cdot S_a(t^*), \quad (4.25)$$

where $S_i = (y_i^*, \theta_i^*, \dot{x}_i^*, \dot{y}_i^*, \dot{\theta}_i^*)'$ for $i \in \{p, a\}$.

4.4.2 Continua of Symmetric Fixed Points

To further investigate the properties of passively generated bounding cycles, a large number of fixed points of the Poincaré map (4.21) is computed. All the fixed points reported in this section comply with the symmetry property (4.25), and they all produce motions similar to the one described in detail in Section 4.4.1.

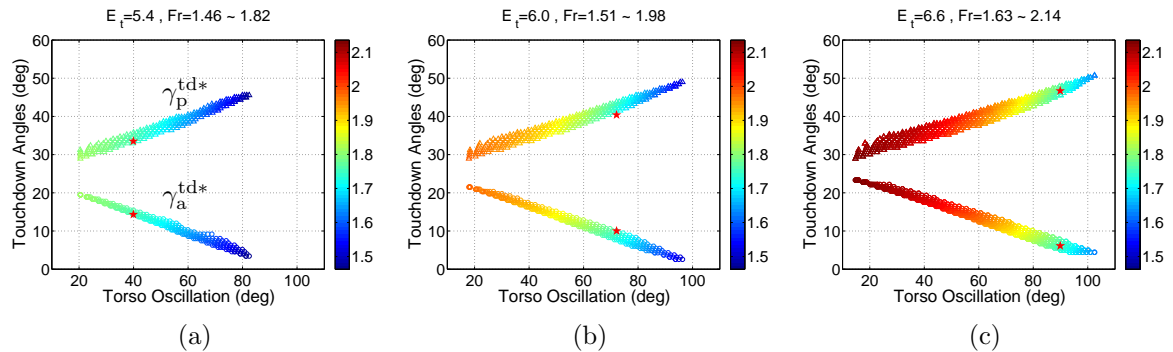


Figure 4.6: Bounding fixed points at different total energy levels; 5.4, 6.0 and 6.6. The vertical axis corresponds to the (absolute) touchdown angles of the posterior (upper branch) and anterior legs (lower branch), $\gamma_p^{\text{td}*}$ and $\gamma_a^{\text{td}*}$, respectively. The horizontal axis corresponds to the range of torso oscillation, see Fig. 4.5(b). The points are colored according to the average velocity computed as the ratio of the stride length over the stride period. The red stars correspond to fixed points with $Fr = 1.75$ obtained at different total energies. As the total energy increases, the star “moves” to larger torso oscillation regions, which implies that maintaining the same forward speed at higher total energies results in more pronounced torso oscillations.

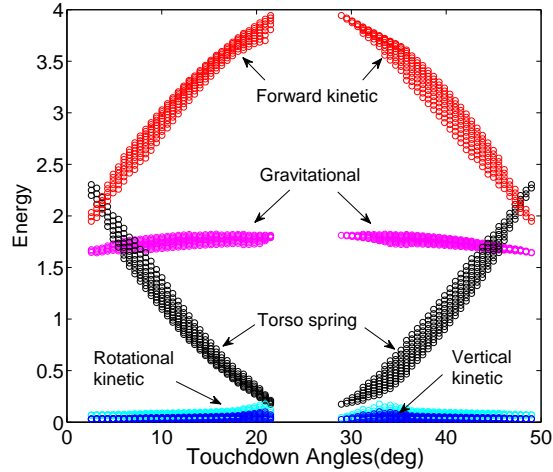


Figure 4.7: Energy distribution at the apex height of the spinal joint for fixed points with total energy $E_t = 6.0$. The horizontal axis corresponds to the (absolute) touchdown angles of the posterior (right branch) and anterior legs (left branch). The vertical axis corresponds to the energy distribution among the modes of the motion.

Due to the conservative nature of the model, the fixed points are organized according to their total energy. The results are summarized in Fig. 4.6, which shows fixed points computed at three different total energy levels; namely, 5.4, 6.0 and 6.6. Fig. 4.6 illustrates that more pronounced torso oscillations and higher average forward velocities can be achieved as the total energy increases. However, at a constant energy level, the torso oscillation range and the average forward speed are inversely related: larger forward speeds correspond to lower torso oscillation ranges. To provide further intuition, Fig. 4.7 presents the energy distribution among the modes of the motion for the fixed points in Fig. 4.6(b). The gravitational potential energy as well as the sum of the rotational kinetic energies of the posterior and anterior parts of the torso remain roughly constant throughout the fixed points. Given that the sum of the vertical kinetic energies of the two parts of the torso is very small, the relation between the forward motion and the torso oscillation becomes clear: fixed points at larger forward kinetic energies are associated with smaller torso elastic energies and vice versa.

It should be mentioned here that the range of forward speeds that can be realized within a constant energy level is significant—at (dimensionless) total energy equal to

6.6 for example, the Froude number varies from 1.63 to 2.14 as Fig. 4.6(c) shows—implying that a certain degree of velocity regulation can be achieved within the same total energy level. This differs from the findings in [99] concerning bounding models with a rigid torso, in which the range of possible forward speeds within the same energy level is very narrow, prompting the development of controllers that regulate the forward speed by regulating the total energy of the system, e.g., as in [141].

Finally, note that, at a nominal gait, the distribution of the total energy between the forward kinetic and the torso elastic energy is related to the touchdown angles. As Fig. 4.6 shows, within the same energy level, a combination of smaller (closer to the vertical) anterior and larger (flatter) posterior touchdown angles causes more pronounced torso oscillations corresponding to nominal motions with lower average forward speeds. On the other hand, larger (flatter) anterior and smaller (closer to the vertical) posterior touchdown angles result in torso oscillations with smaller amplitudes, thereby accommodating higher forward velocities. Clearly, the leg touchdown angles provide powerful control inputs for regulating the distribution of the total energy among these modes and thus altering the forward speed.

4.5 Local Stability

To analyze the local stability properties of bounding, we linearize (4.21) at a fixed point $(\bar{z}_f^*, \bar{\alpha}_f^*)$ resulting in

$$\Delta z_f^*[k+1] = A\Delta z_f^*[k] + B\Delta\alpha_f^*[k], \quad (4.26)$$

where $\Delta z_f^* = z_f^* - \bar{z}_f^*$, and $\Delta\alpha_f^* = \alpha_f^* - \bar{\alpha}_f^*$, and

$$A = \left. \frac{\partial \mathcal{P}^*}{\partial z_f^*} \right|_{z_f^* = \bar{z}_f^*, \alpha_f^* = \bar{\alpha}_f^*}, \quad B = \left. \frac{\partial \mathcal{P}^*}{\partial \alpha_f^*} \right|_{z_f^* = \bar{z}_f^*, \alpha_f^* = \bar{\alpha}_f^*}. \quad (4.27)$$

While the largest eigenvalue of the majority of the fixed points computed in Section 4.4.2 for the parameters of Table 4.1 has magnitude less than three, none gives rise to a passively stable bounding cycle. It is known, however, that in the context of rigid-torso quadrupedal models, passively stable walking [109] and running motions

[28] can be generated through suitable combinations of the physical parameters of the system. Motivated by these results, this section examines the effect of certain (dimensionless) parameters on the stability of the resulting motion, concluding that self-stable bounding orbits can indeed be generated under suitable parameter combinations.

4.5.1 Coordination of Torso and Leg Spring Stiffness

We begin by considering the effect of the relative torso and leg stiffness on the system’s motion, since these parameters are of key importance for the leg-torso coordination. Fig. 4.8 shows how the spectral radius $\rho(A) := \max_i |\lambda_i|$ of the matrix A in (4.26) changes as a function of the pair $(\kappa_{\text{leg}}, \kappa_{\text{torso}})$ —defined by (4.11) and (4.12), respectively—keeping the rest of the (dimensionless) parameters—namely, I and d defined by (4.9) and (4.10), respectively—constant. The grey area in Fig. 4.8 corresponds to periodic motions with multiple torso flexions and extensions within one stride as shown in Fig. 4.5(c). These types of periodic behaviors appear for small values of leg stiffness. Clearly, a softer leg requires a relatively longer time period to go through a complete compression and decompression phase during stance, thereby allowing the torso to oscillate multiple times within one stride, as in Fig. 4.5(c).

An interesting observation from Fig. 4.8 is that the range of values of the relative leg stiffness over which bounding gaits—not necessarily stable ones—can be generated passively depends strongly on the coordination of the torso and leg spring stiffness. For example, when the dimensionless torso stiffness $\kappa_{\text{torso}} = 3.6$ passively generated bounding orbits exist for $\kappa_{\text{leg}} \in [20.80, 21.55]$. On the other hand, when $\kappa_{\text{torso}} = 5.4$, bounding orbits can be generated for $\kappa_{\text{leg}} \in [22.00, 28.15]$, a significantly wider region than that corresponding to $\kappa_{\text{torso}} = 3.6$. Fig. 4.8 also illustrates that self-stable bounding motions emerge for particular combinations of the relative torso and leg stiffness. These motions correspond to a small fraction of the bounding gaits that can be generated passively, a fact that can be explained by Figs. 4.9(a) and 4.9(b) that show the loci of the eigenvalues of A in (4.26) as the parameters κ_{torso} and κ_{leg} vary. In more detail, Fig. 4.9(a) indicates that as the torso stiffness κ_{torso} increases for

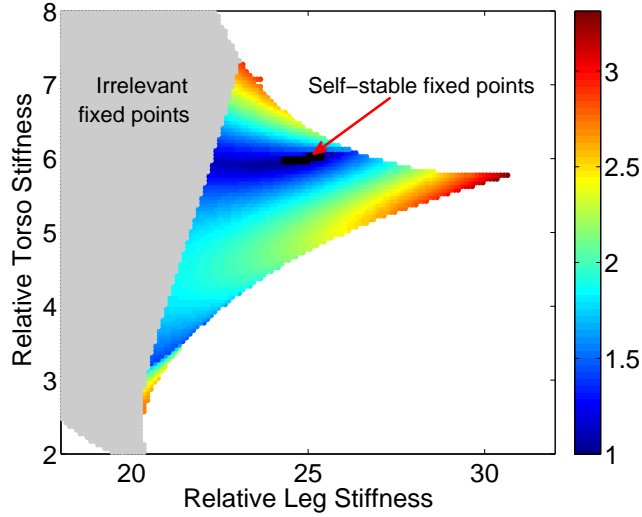
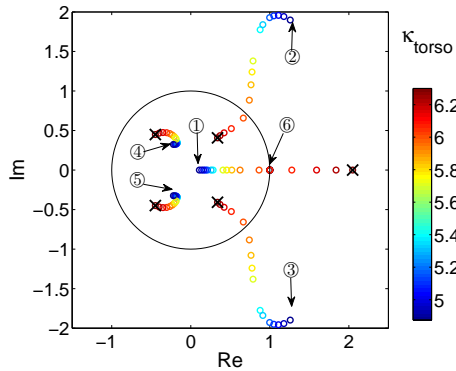
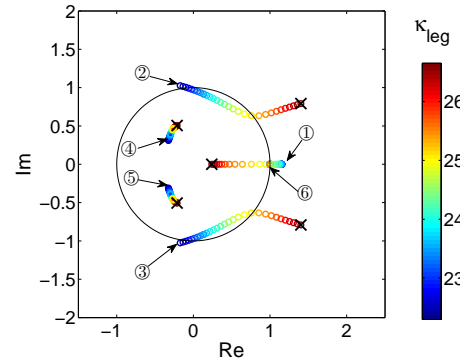


Figure 4.8: Fixed points computed for the same total energy ($E_t^* = 7.95$), average speed ($Fr = 2.41$) and hopping height ($y_{tj}^* = 0.82$) and for different values of dimensionless leg and torso stiffness. The color code corresponds to the values of the spectral radius of A .



(a) $\kappa_{leg} = 25.00$ and κ_{torso} varying in $[4.88, 6.30]$



(b) $\kappa_{torso} = 6.00$ and κ_{leg} varying in $[22.30, 26.65]$

Figure 4.9: The paths of the six eigenvalues for constant dimensionless leg stiffness κ_{leg} as the dimensionless torso stiffness κ_{torso} varies (Fig. 4.9(a)) and for constant dimensionless torso stiffness κ_{torso} as the dimensionless leg stiffness κ_{leg} varies (Fig. 4.9(b)). The numbers show the points at which the eigenvalues start and “x” the points at which they terminate. In all cases, the eigenvalue denoted by “6” remains at one due to the conservative nature of the system. All the fixed points correspond to the same (dimensionless) total energy ($E_t^* = 7.95$), average speed ($Fr = 2.41$) and hopping height ($y_{tj}^* = 0.82$).

a given value of κ_{leg} the eigenvalues “2” and “3” enter the unit circle. However, the eigenvalue “1” eventually exits from the unit circle, implying that an upper bound on κ_{torso} exists, beyond which instability occurs. On the other hand, Fig. 4.9(b) shows that keeping κ_{torso} constant and increasing κ_{leg} moves the eigenvalue “1” inside the unit circle, but the eigenvalues “2” and “3” exhibit the opposite behavior: while they initially are compromised within the unit circle, they eventually move outside of it.

4.5.2 Other Physical Parameters

The range of values of $(\kappa_{\text{torso}}, \kappa_{\text{leg}})$ that result in self-stable motions depends on the rest of the parameters; namely, the (dimensionless) moment of inertia I and hip-to-COM distance d . To provide more information, Fig. 4.10 shows fixed points computed with the same forward speed, hopping height and total energy as the ones in Fig. 4.8, but for different values of I and d . Clearly, the same pattern as in Fig. 4.8 is observed. Furthermore, as the moment of inertia I increases, a larger number of fixed points can be computed, and there exists a threshold value for I —approximately 1.6—beyond which self-stability emerges. On the other hand, Fig. 4.10(b) demonstrates that the relative hip-to-COM distance does not have a significant impact on self-stability; the number of passively stable fixed points does not significantly vary for a wide range of hip-to-COM distance values. It should be mentioned here that, in all cases, the range of parameter values that result in self-stable motions is narrow, explaining the difficulty in computing such motions in the research efforts [90, 35].

As a final remark, note that self-stability in the presence of a flexible segmented torso is not immediate given the existence of such bounding orbits in quadrupedal models with rigid torso [99, 28]. The reason is that torso bending movements may cause divergent behavior when they are not properly coordinated with the hybrid oscillations of the legs. While in the rigid-torso case the inertia properties of the torso—captured by the dimensionless moment of inertia of the torso—dominate self-stability [99, 28], in the flexible-torso case, the combination of the stiffness properties of the legs and the torso appears to be the dominant factor.

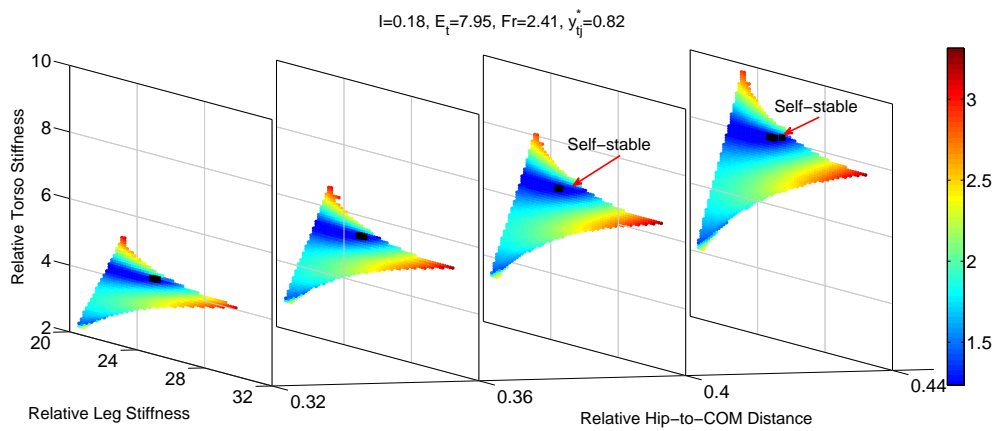
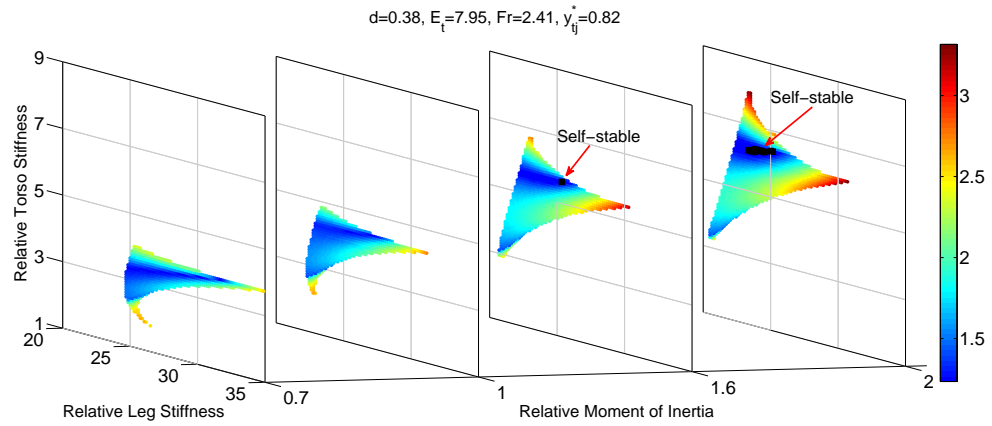


Figure 4.10: The relationship between the stiffness of the leg and torso springs for fixed points computed for the same (dimensionless) total energy ($E_t = 7.95$), average forward speed ($Fr = 2.41$) and hopping height ($y_{ij}^* = 0.82$) with (a) same relative hip-to-COM distance but different relative moment of inertia and (b) same relative moment of inertia but different relative hip-to-COM distance. The color code corresponds to the values of the spectral radius of A . The black points represent the passively stable fixed points.

Chapter 5

FEEDBACK CONTROL OF QUADRUPEDAL BOUNDING

The existence of passively generated bounding orbits and its relation to key design parameters that couple the stiffness, inertia and geometric properties of the model can provide useful information for the design of quadrupedal robots with a flexible torso. In terms of stability, however, it is clear that the model in its current passive and conservative form cannot reject disturbances that perturb the total energy of the system. Furthermore, even when the applied perturbations do not alter the total energy level, the domain of attraction of the self-stable bounding orbits found in Section 4.5 is not sufficiently large to practically ensure convergence. Clearly, the development of control laws is necessary to sustain periodic bounding orbits in the presence of perturbations. This chapter takes a step toward this direction by proposing a controller that uses a *single* actuator located at the spinal joint to enhance the stability of the 4-DOF compliant bounding model discussed in the previous sections.

Section 5.1 gives an overview of general structure of the controller which consists of both continuous-time and discrete-time components, which are explained in detail in Section 5.2 and 5.3, respectively; see also [25]. In the last section, the capability of the closed-loop system in dealing with disturbances are discussed [22]. It should be mentioned that—as will be shown in Chapter 6 and Chapter 8—the control architecture developed in this chapter can be used to stabilize pronking motions as well as to derive feedback control laws for models with non-trivial leg mass and inertia [26].

To enable the development of non-conservative corrective forces, the passive flexible-torso model in Fig. 1.1 (a) is modified to include one actuator in parallel with

the torso spring; see Fig. 1.1 (b). With this modification, the open-loop dynamics of the system (4.3) in each phase $i \in \{\text{fe}, \text{fg}, \text{sp}, \text{sa}\}$ becomes

$$\dot{x}_i = f_i(x_i) + g_i(x_i)u_i, \quad (5.1)$$

where u_i is the input torque; note that the vector field f_i in (5.1) corresponds to the passive dynamics (4.3). For concreteness, we consider a model with mechanical properties that roughly correspond to the quadrupedal robot Scout II [99]; see Table 5.1.

5.1 Overview of the Hybrid Controller

The proposed controller exploits the hybrid nature of the system by introducing control action on two levels; see Fig. 5.1. On the first level, a continuous-time controller is employed at the torso joint to impose a virtual (holonomic) constraint that coordinates the torso and legs according to a passively generated bounding orbit; the orbit is selected to satisfy desired forward velocity and hopping height specifications. On the second level, a discrete-time controller that uses event-based state feedback is engaged to update the leg touchdown angles.

It should be mentioned here that in rigid-torso models, the stability of the torso pitch oscillation in bounding emerges without direct control over the pitch angle for a wide range of initial conditions [104, Chapter 8] provided that the dimensionless moment of inertia of the torso is less than one. However, in models with a segmented flexible torso, the additional degree of freedom corresponding to the torso relative pitch

Table 5.1: Mechanical Parameters of the Model

Parameter	Value	Units
Half Torso Mass (m)	10.432	kg
Half Torso Inertia (J)	0.36	kg m ²
Hip-to-COM spacing (L)	0.138	m
Nominal Leg Length (l_0)	0.36	m
Leg Spring Constant (k_{leg})	7329	N/m
Torso Spring Constant (k_{torso})	203	Nm/rad

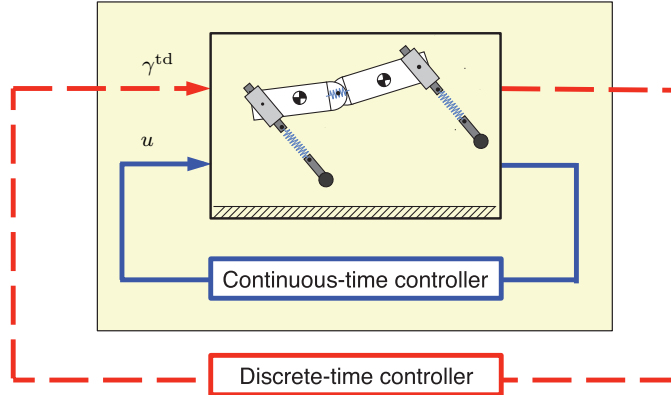


Figure 5.1: Feedback diagram representing the structure of the hybrid controller. Continuous lines represent signals in continuous time; dashed lines represent signals in discrete time. The shaded block denotes the subsystem created via the feedback control in the continuous time. The discrete-time control action ensures that the resulting subsystem is locally exponentially stable.

oscillations is very sensitive to perturbations and highly coupled to the leg motion. The controller proposed here explicitly couples the torso relative pitch oscillation to the leg motion, effectively reducing the system so that stability is determined by the event-based updates of the leg touchdown angles.

5.2 Continuous-time Control

For each phase $i \in \{\text{sp}, \text{sa}, \text{fg}, \text{fe}\}$ we associate to the continuous dynamics (5.1) the output function

$$y_i = h_i(q_i) := H_i q_i - h_{P,i}^d(q_i), \quad (5.2)$$

where

$$H_i := \begin{bmatrix} 0 & 0 & -1 & 1 \end{bmatrix}, \quad (5.3)$$

so that, by (4.1) and (4.2), the *controlled variable* $H_i q_i$ corresponds to the relative pitch angle $\theta_a - \theta_p$ and $h_{P,i}^d(q_i)$ is its desired evolution. Note that in (5.2), $h_i(q_i)$ is a function of the configuration variables (not time), and therefore it can be interpreted as a (virtual) holonomic constraint. This constraint can be imposed on the system in an asymptotic fashion via a control law, the objective of which is to drive the output (5.2)

to zero. To simplify¹ the development, PD control laws will be employed to achieve this objective; i.e.,

$$u_i = K_{P,i}y_i + K_{D,i}\dot{y}_i, \quad (5.4)$$

where $K_{P,i}$ and $K_{D,i}$ are selected gains.

It is through the design of $h_{P,i}^d(q_i)$ in (5.2) that information about the leg-torso coordination pattern that characterizes the selected passively generated gait is passed to the controller. In more detail, $h_{P,i}^d(q_i)$ is designed through a suitable parameterization of the evolution of the relative pitch angle $\theta_a - \theta_p$ at the selected (desired) passive gait. To simplify the implementation, for $i \in \{\text{f, sp, sa}\}$, $h_{P,i}^d(q_i)$ is selected as a fifth degree polynomial

$$h_{P,i}^d(q_i) = \sum_{k=0}^5 a_{i,k} s^k(q_i), \quad (5.5)$$

fitted to the nominal evolution of $\theta_a - \theta_p$ according to the desired passive orbit. It is important to note that the function s in (5.5) does *not* explicitly depend on time, and it is selected for the stance and flight phases as is detailed in the following sections.

5.2.1 Stance Phases

Utilizing the fact that during the anterior and posterior stance phases, $\theta_a - \theta_p$ is a (strictly) monotonic function of the angle of the stance leg relative to the torso—see also Fig. 5.2—the function $s(q_i)$ in (5.5) can be selected as

$$s(q_i) := \frac{\bar{\varphi}^{\max} - \varphi}{\bar{\varphi}^{\max} - \bar{\varphi}^{\min}}, \quad s \in [0, 1] \quad (5.6)$$

where $i \in \{\text{sp, sa}\}$,

$$\varphi := \begin{cases} \varphi_p, & \text{for } i = \text{sp} \\ \varphi_a, & \text{for } i = \text{sa}, \end{cases} \quad (5.7)$$

and $\bar{\varphi}^{\min}$ and $\bar{\varphi}^{\max}$ are the minimum and maximum values of φ in the corresponding stance phase during the nominal motion. Then, the coefficients $a_{i,k}$ are determined via

¹ Alternatively, instead of using PD controllers, the inputs that zero the outputs could be computed through feedback linearization [143].

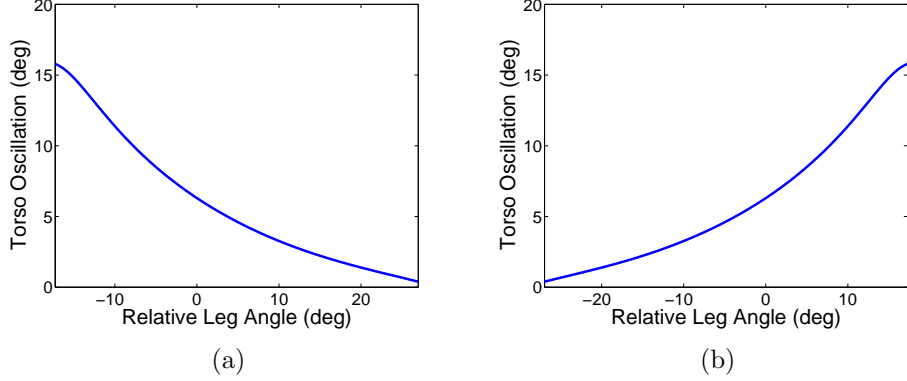


Figure 5.2: The relative torso pitch angle $\theta_a - \theta_p$ as a function of the leg angle φ_p and φ_a in the posterior (a), and the anterior (b) stance. The monotonic relation allows to coordinate the torso oscillation with the leg sweeping motion through a virtual holonomic constraint.

fitting (5.5) to the evolution in Fig. 5.2(a) and Fig. 5.2(b) for the stance-posterior and stance-anterior respectively. Intuitively, with this parametrization, the virtual constraint design (5.2) ensures that the torso extends during the posterior stance phase and flexes during the subsequent anterior stance phase, and that this flexion-extension oscillation is coordinated with the nominal motion through the sweeping angle of the corresponding stance leg.

5.2.2 Flight Phases

In a similar fashion, during the flight phases, $s(q_f)$ is computed as

$$s(q_f) := \frac{x_{tj}(q_f) - \bar{x}_{tj}^{\min}}{\bar{x}_{tj}^{\max} - \bar{x}_{tj}^{\min}}, \quad s \in [0, 1] \quad (5.8)$$

where x_{tj} is the horizontal distance travelled by the torso spinal joint during flight; i.e.,

$$x_{tj}(q_f) := x_p + L \cos \theta_p, \quad (5.9)$$

where x_p is the horizontal position of the COM of the posterior part of the torso and θ_p the corresponding pitch angle as in Fig. 4.1. In (5.8), \bar{x}_{tj}^{\min} and \bar{x}_{tj}^{\max} are the values of x_{tj} at the beginning and at the end of the flight phase, respectively.

Note that when the system is closed-loop with the continuous-time controller described above bounds along a nominal orbit, the torques developed by the actuator

are very small, but are not exactly equal to zero; see also Section 5.4.1 below. This is due to the numerical errors introduced by the fitting process. Increasing the degree of the polynomials in (5.5) may help decreasing the fitting error. To further suppress the residual torques after convergence to the nominal gait, the PD controller (5.4) can be implemented using

$$\dot{y}_i = H_i \dot{q}_i - h_{V,i}^d(q_i), \quad (5.10)$$

where, instead of differentiating (5.5) with respect to time, $h_{V,i}^d(q_i)$ is obtained by fitting a new polynomial to the rate of change of y_i . A similar idea has been employed by [143] in the context of passive bipedal walking, and is very effective in reducing the torques that are present in the nominal motion.

5.3 Discrete-time Control

The posterior and anterior leg touchdown angles $\alpha_f = (\gamma_p^{\text{td}}, \gamma_a^{\text{td}})'$ provide control inputs that (partially) determine when the corresponding gathered and extended flight phases are terminated. A variety of control procedures is available for updating these angles in an event-based fashion to enhance stability; see [104] or [7] for examples. In this work, a discrete Linear Quadratic Regulator (LQR) is employed that positions the legs during flight based on feedback of the states at the apex height of the gathered flight phase as follows

$$\alpha_f[k] = \bar{\alpha}_f + K(z_f^{\text{apex}}[k] - \bar{z}_f^{\text{apex}}). \quad (5.11)$$

where z_f^{apex} are the states (4.22) corresponding to the parameters of Table 5.1 and \bar{z}_f^{apex} is their nominal (fixed-point) values. The gain matrix K is determined by MATLAB's `dlqr` function.

5.4 Disturbance Rejection

In this section, the ability of the proposed controller to establish convergence to a nominal gait under the influence of unexpected disturbances is assessed. Quantifying disturbance rejection is an important and challenging problem in legged locomotion, and several metrics have been proposed in the relevant literature to capture aspects

of it; [67] and [83] provide detailed accounts of available metrics. Here, we describe the performance of the controller as the system recovers from an unexpected step, and we provide numerically computed estimates of projections of the domain of attraction that highlight the advantages and limitations of the proposed control approach.

5.4.1 Unexpected Ground Height Variations

Encountering a disturbance in the form of an unexpected step is a commonly employed measure of disturbance rejection [67, 83, 139, 92]. In our setting, the model experiences a variation in the ground height that is equal to 20% of the nominal leg length (approximately 7.2cm). Figure 5.3 shows snapshots of the system’s motion as it converges to a periodic orbit, which corresponds to the desired (nominal) one when the hopping height is measured from the new ground level. In addition, Fig. 5.4 shows the evolution of the hopping height, forward velocity and the total energy

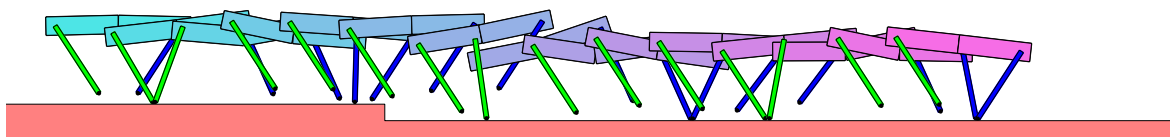


Figure 5.3: Snapshots of the model’s motion as it runs down a step of 7.2cm (20% of the nominal leg length).

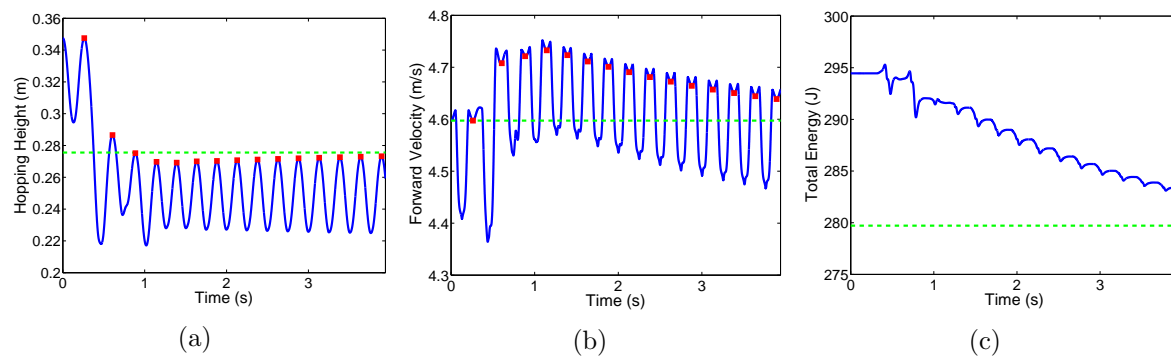


Figure 5.4: Response of the system to a step-down disturbance of 7.2cm showing convergence to the nominal orbit. (a) Hopping height; (b) Forward velocity; (c) Total energy. The red squares represent the apex height in the gathered flight and the green dotted lines represent the final values.

of the system and Fig. 5.5(b) presents the corresponding ground reaction forces and input torques developed by the torso actuator for the first six strides. It is noted that the step-down disturbance does not significantly affect the hopping height oscillations (measured from the new ground level). Instead, the forward speed is affected more, but it eventually converges to its nominal value after few strides. The profile of the corresponding ground reaction forces in Fig. 5.5(b) resembles the one used to generate bounding through force planning in [137] based on the ground reaction forces of a galloping dog [140]. Note though, in the model studied here, these forces are primarily the result of the springy unactuated legs. It should also be mentioned that the friction cone limitations are respected throughout the motion. Finally, during the first stride which is along the nominal orbit, the torque is close, but not exactly equal, to zero due to the fitting errors associated with (5.5). In the recovering strides, the size of the input torque remains within practically reasonable bounds, and eventually becomes very small as the system converges to its nominal motion.

5.4.2 Domain of Attraction

Estimates of the domain of attraction of periodic walking or running motions are frequently employed in locomotion studies to evaluate robustness to perturbations [46, 10]. Except for the case of models with sufficiently low dimension², it is not feasible to compute the domain of attraction in its entirety through simulations over the space of all possible initial conditions. Therefore, to further analyze the disturbance rejection capabilities of the bounding model of Fig. 4.1 in closed loop with the controller of Section 5.1, Fig. 5.6 provides an estimate of the projection of the domain of attraction onto the (\dot{x}_{tj}, y_{tj}) plane that characterizes the system's ability to handle simultaneous perturbations in forward speed and hopping height states.

In computing Fig. 5.6, perturbations in the nominal forward speed and hopping height are introduced at the apex of the gathered flight phase, and a perturbed initial

² In the case of simple passive dynamic walkers for example, the domain of attraction of walking motions of interest can be (numerically) fully characterized [117, 143].

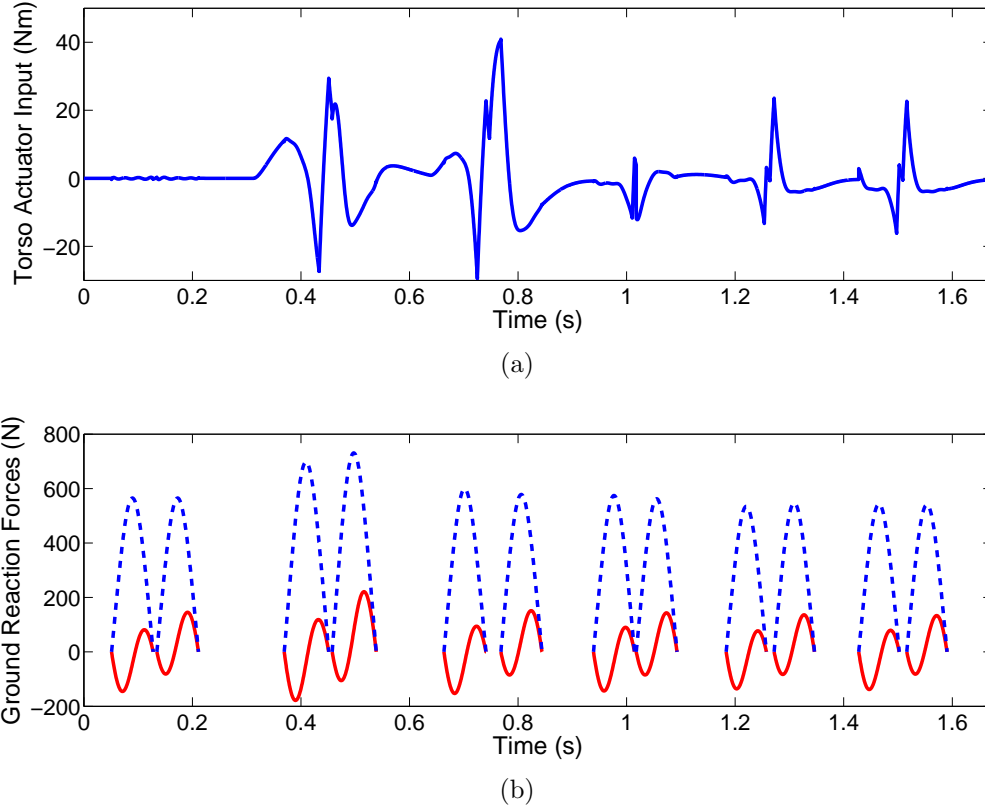


Figure 5.5: (a) The input of the torso joint actuator. (b) Horizontal (red continuous) and vertical (blue dotted) components of ground reaction force. For clarity, only the first six strides are presented.

condition is assumed to belong to the domain of attraction if after 50 strides the error from the nominal motion is less than 1%. Note also that all the points of Fig. 5.6 correspond to motions where the maximum torque developed by the torso actuator is less than 50Nm. In converging to the nominal orbit, the model may experience double stance phases, where both anterior and posterior leg are in contact with the ground; the corresponding initial conditions that cause the emergence of such phases are depicted in red in Fig. 5.6.

Comparing the green area in Fig. 5.6, which corresponds to the initial conditions that are attracted to the nominal orbit in the open-loop system, it can easily be seen that the controller significantly enlarges the domain of attraction of the desired

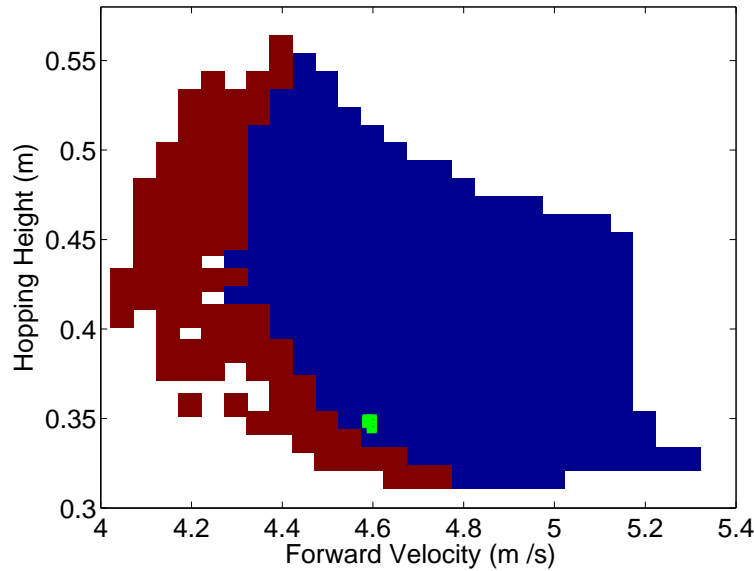


Figure 5.6: (\dot{x}_{tj}, y_{tj}) cross section of the domain of attraction towards the passive periodic motion when the maximum torque of the torso actuator does not exceed 50Nm. The green, blue and red area correspond the passive system, closed-loop system without consideration of double stance phase and close-loop systems with double stance phase, respectively.

motion. However, it is apparent that perturbations that tend to simultaneously decrease the forward velocity and hopping height cannot be accommodated as easily as perturbations in the opposite direction. In fact, perturbations of this kind—decreasing hopping height and forward velocity—tend to result in failure to sustain running due to insufficient toe clearance. This is a consequence of the absence of active control over the leg length; clearly, maintaining the leg at its nominal length during flight phase makes the system susceptible to toe scuffing, and this is more likely to occur when the energy content of the system is smaller during the first steps after the perturbation is encountered. This limitation is attributed to the model’s capabilities rather than the control laws. In fact, it should be emphasized that the proposed control law is capable of stabilizing a 4-DOF compliant system undergoing significantly large disturbances with only one actuator. Additional actuators can be included at the hips and/or the

legs to further improve the performance of the controller or to achieve additional control objectives in the context of more complete higher-dimensional robot models, which will be discussed in [Chapter 8](#).

Chapter 6

GAIT TRANSITIONS BETWEEN PRONKING AND BOUNDING

In this chapter, we will utilize the tools developed in Chapter 4 and Chapter 5 to generate stable pronking motions using the same reduced-order model in Fig. 4.1; see also Fig. 1.1(b) and [24]. Then, by estimating the domain of attraction of pronking and bounding motions using SOS programming, conservative conditions regarding the feasibility of transitions between these gaits can be stated analytically. Section 6.1 introduces the general approach of performing gait transitions as sequential composition of controllers. Section 6.2 and Section 6.3 derive the dynamics and passively generate periodic pronking and bounding motions. The properties of the periodic motions, especially the pitch rate, reveal the challenge of performing direct transition from pronking and bounding without double stance. In Section 6.4, the hybrid controller previously developed in Chapter 5 is employed to enhance the stability of the passively generated motions. Section 6.5 provides analytically estimates of the domain of attraction of different gaits and demonstrates the transitions between gaits at a given speed.

6.1 General Scheme

We formulate gait transition as a problem of switching between limit cycles as is conceptually illustrated in Fig. 6.1. The limit cycles ϕ_0 and ϕ_1 represent periodic motions corresponding to different gaits. To characterize stability, the method of Poincaré is used, resulting in two discrete-time mappings \mathcal{P}_0 and \mathcal{P}_1 and the corresponding fixed points \bar{z}_0 and \bar{z}_1 . Assuming the two limit cycles are stabilized under the influence of the controllers Γ_0 and Γ_1 , respectively, the domain of attraction of the limit cycles on the Poincaré sections \mathcal{S}_0 and \mathcal{S}_1 can be estimated as \mathcal{D}_0 and \mathcal{D}_1 . By examining the relationship between the estimated domains of attraction and the fixed points, feasible

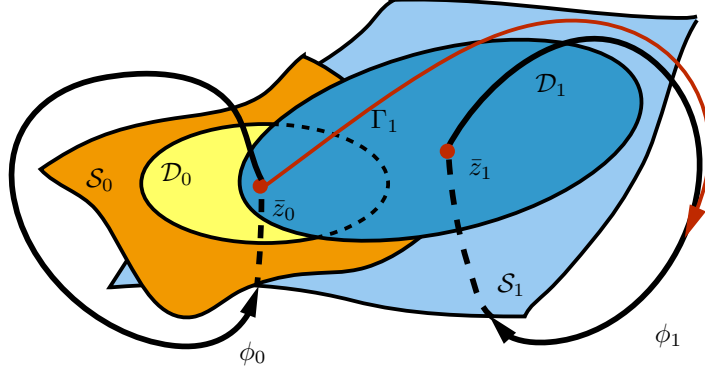


Figure 6.1: A conceptual illustration of the transition between two different limit cycles, i.e., ϕ_0 and ϕ_1 , which in legged locomotion could correspond to periodic motions of different gaits, for instance, pronking and bounding in this study. \mathcal{S}_0 and \mathcal{S}_1 are the Poincaré sections of ϕ_0 and ϕ_1 , and \bar{z}_0 and \bar{z}_1 are the corresponding fixed points. \mathcal{D}_0 and \mathcal{D}_1 are the domain of attractions at the Poincaré sections for ϕ_0 and ϕ_1 , respectively.

transitions can be determined. For instance, as shown in Fig. 6.1, if \bar{z}_0 is within the domain of attraction of ϕ_1 at the Poincaré section, then by employing the controller Γ_1 , the system starting from \bar{z}_0 will eventually converge to the orbit ϕ_1 , i.e., switch to \bar{z}_1 . Mathematically, if $\bar{z}_0 \in \mathcal{D}_1$, then $\bar{z}_0 \xrightarrow{\Gamma_1} \bar{z}_1$. Furthermore, if $\bar{z}_1 \in \mathcal{D}_0$, then two-way transitions can be realized between the two gaits, i.e., $\bar{z}_0 \xleftrightarrow[\Gamma_0]{\Gamma_1} \bar{z}_1$.

6.2 Descriptions of Pronking and Bounding Gaits

In a pronking gait, shown in Fig. 6.2(a), both the anterior and the posterior legs touch and leave the ground in unison. In a bounding gait, two variations are considered: one with double stance and one without. For both pronking and bounding, depending on the state of the legs—stance or flight—we distinguish the following phases: the double flight phase, denoted by “f”, in which both legs are in the air; the stance-posterior phase, denoted by “sp”, when only the posterior leg is on the ground; the stance-anterior phase, denoted by “sa”, when only the anterior leg is on the ground; and the double stance phase, denoted by “sd”, in which both legs are in contact with the ground.

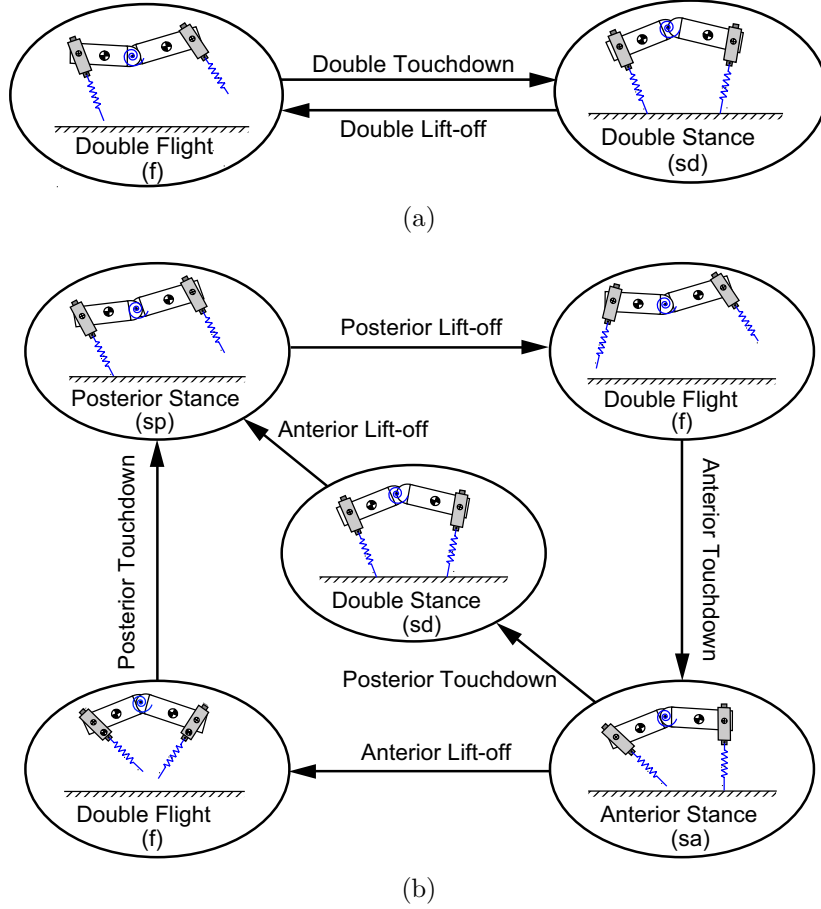


Figure 6.2: (a) Pronking gait; (b) Two variations of bounding gait.

6.3 Passively Generated Motions

The hybrid dynamics of all the gaits can be studied using Poincaré’s method, resulting in return maps of the form:

$$z_f[k+1] = \mathcal{P}(z_f[k], \alpha_f[k]), \quad (6.1)$$

where $z_f := (y_p, \theta_p, \theta_a, \dot{x}_p, \dot{\theta}_p, \dot{\theta}_a)'$ represents the (reduced) states at the Poincaré section and α_f represents the vector of touchdown angles.

A large number of fixed points corresponding to passive pronking and bounding gaits can be generated. Reflecting the symmetry of the underlying vector fields, the computed fixed points exhibit certain symmetry properties that will be useful in designing transition controllers. In more detail, for both pronking and bounding, $\theta_p = -\theta_a$

and $\dot{\theta}_p = \dot{\theta}_a$ at the apex height. Specifically, the pronking gait exhibits zero pitch velocity at apex height, i.e., $\dot{\theta}_p = \dot{\theta}_a = 0$. These symmetry properties facilitate the investigation of the states that distinguish the two gaits at the Poincaré section. Figure 6.3 shows the apex height, the posterior pitch angle and the posterior pitch rate of the fixed points corresponding to pronking and bounding gaits. It can be seen that these three types of motions can be distinguished by the pitch rate of the posterior part of the torso; in particular, pronking has zero pitch rate, bounding with double stance has small pitch rate magnitude (< 2.5 rad/s) and bounding without stance exhibits larger values of pitch rate (in the range of $[2.5$ rad/s, 5 rad/s]).

The significant difference in the pitch rate shown in Fig. 6.3 clearly demonstrates the natural separation in the dynamics of different gaits, and reveals a major challenge in achieving gait transition. In the context of transitioning from pronking to bounding without double stance, the model needs to experience a drastic perturbation in the torso dynamics, which can easily destabilize the motion. In other words, following the definition in Section 6.1, if the bounding motion is regarded as the target limit cycle, to guarantee convergence, the domain of attraction at the Poincaré section of the bounding limit cycle should be excessively large in order to include the pronking fixed point. However, the model in its current passive and conservative form is limited in rejecting disturbances, resulting in narrow domains of attraction; in fact, not all the

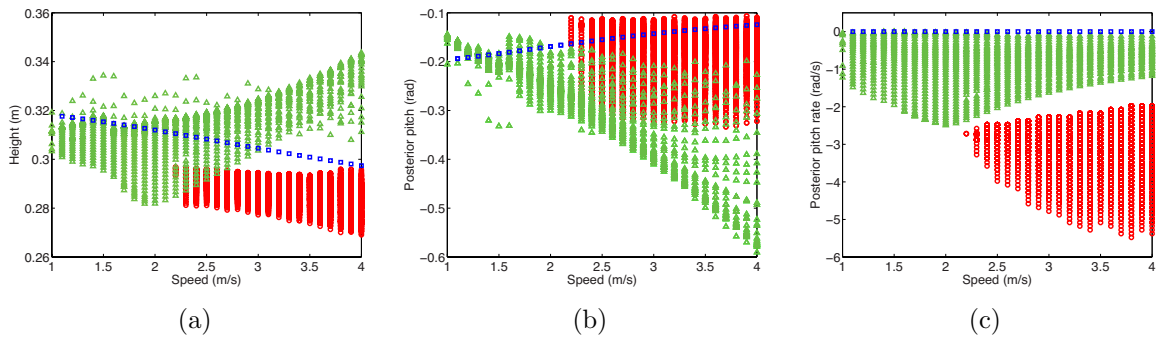


Figure 6.3: The apex height (a), posterior pitch angle (b) and posterior pitch rate (c) of the fixed points corresponding to pronking (blue square), bounding without double stance (green triangle) and bounding with double stance (red circle) at speed $[1, 4]$ m/s.

fixed points computed are stable. Therefore, transitioning from pronking to bounding calls for developing control laws that stabilize the gaits and ensure that the domain of attraction of the “target” gait is sufficiently large to include the states of the “source” gait.

6.4 Feedback Control

In this section, a controller employing actuation at the torso joint will be developed to stabilize the pronking and bounding motions computed in Section 6.3. The structure of the controller is the same as the one developed in Chapter 5, thus here we only give an outline of the controller design.

6.4.1 An Extended Gait Description

To enlarge the domain of attraction of the nominal motions, the model is allowed to go through additional phases beyond nominal phase sequences as it converges to the target motion; see Fig. 6.4. For example, in the nominal pronking motion, both the anterior and posterior legs touch and leave the ground in unison with the same touchdown angle. However, when the motion is disturbed during the flight – e.g., when the anterior pitch angle increases – then determining the touchdown angles α_f that result in simultaneous touchdown and liftoff requires numerically solving for the dynamics of the double stance phase. To avoid such cumbersome computation, the model is allowed to enter either posterior stance or anterior stance before entering the double stance phase; Fig. 6.4(a). Under the control action, the duration of these two augmented phases gradually decreases to zero, resulting in the nominal periodic motion. In Fig. 6.4(b) and 6.4(c), the double flight and double stance are augmented after the anterior stance for bounding with and without double stance, respectively.

6.4.2 Hybrid Controller

As in Section 5.1, the hybrid controller introduces control action on two levels. In continuous time, holonomic constraints are imposed to the system to coordinate—according to a passively generated motion—the torso’s flexion-extension oscillations

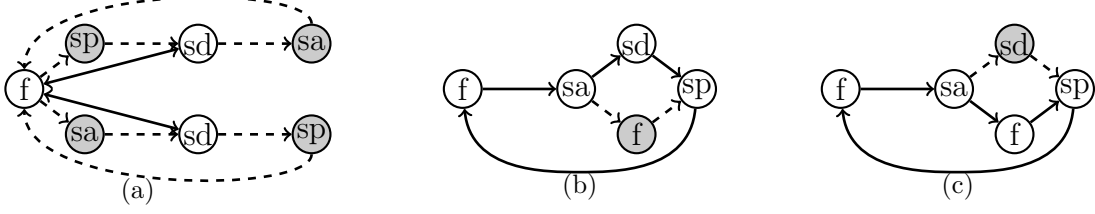


Figure 6.4: Extended description of the gaits in the presence of perturbation for pronking (a), bounding with double stance (b) and bounding without double stance (c). The shaded phases are the augmented phases and the dotted lines represent the possible evolution in presence of perturbation.

with the leg's motion during stance¹. Under the continuous-time control, the closed-loop Poincaré map becomes

$$z_f[k+1] = \mathcal{P}_1^{\text{cl}}(z_f[k], \alpha_f[k]) \quad (6.2)$$

and its linearization takes the form

$$\Delta z_f[k+1] = A\Delta z_f[k] + B\Delta \alpha_f[k], \quad (6.3)$$

where

$$A = \left. \frac{\partial \mathcal{P}_1^{\text{cl}}}{\partial z_f} \right|_{z_f=\bar{z}_f, \alpha_f=\bar{\alpha}_f}, \quad B = \left. \frac{\partial \mathcal{P}_1^{\text{cl}}}{\partial \alpha_f} \right|_{z_f=\bar{z}_f, \alpha_f=\bar{\alpha}_f} \quad (6.4)$$

and $\Delta z_f = z_f - \bar{z}_f$, $\Delta \alpha_f = \alpha_f - \bar{\alpha}_f$.

In discrete time, a discrete linear quadratic regulator (LQR) is employed to place the legs during flight based on feedback of the states at the Poincaré section to minimize the quadratic cost function

$$J(z_f, \alpha_f) = \sum_{k=1}^{\infty} (z_f[k] - \bar{z}_f)' Q (z_f[k] - \bar{z}_f) + (\alpha_f[k] - \bar{\alpha}_f)' R (\alpha_f[k] - \bar{\alpha}_f) \quad (6.5)$$

where z_f are the states and \bar{z}_f is their nominal values, and Q and R are selected positive definite matrices. It can be shown that the optimal cost-to-go, J^* , is given by

$$J^*(z_f) = (z_f[k] - \bar{z}_f)' S (z_f[k] - \bar{z}_f) \quad (6.6)$$

¹ During the double stance phase, the relative pitch angle is slaved to the posterior leg angle.

where S is the infinite horizon solution of the associated discrete-time Riccati equation:

$$A'SA - S - (A'SB)(B'SB + R)^{-1}(B'SA) + Q = 0 \quad (6.7)$$

The optimal feedback policy is given by

$$\alpha_f[k] = \bar{\alpha}_f - K(z_f[k] - \bar{z}_f) \quad (6.8)$$

where K is derived from S :

$$K = (B'SB + R)^{-1}(B'SA) \quad (6.9)$$

and A, B have been defined in (6.3).

With the discrete-time control action, the closed-loop form of the Poincaré map (6.2) becomes

$$\begin{aligned} z_f[k+1] &= \mathcal{P}_1^{\text{cl}}(z_f[k], \bar{\alpha}_f - K(z_f[k] - \bar{z}_f)) \\ &= \mathcal{P}_2^{\text{cl}}(z_f[k]) \end{aligned} \quad (6.10)$$

and the associated control action can be stated as

$$\Gamma := \Gamma(\bar{z}_f, \bar{\alpha}_f, \beta, K) \quad (6.11)$$

where β includes all the coefficients in designing the virtual holonomic constraints in the continuous-time control.

6.5 Gait Transition

As an example of gait transition behavior, this section examines switching between pronking and bounding without double stance. First, a strategy for estimating analytically the domain of attraction of the closed-loop system is introduced. Then, transitions between pronking and bounding are realized through a sequence of switchings among fixed points with bounding with double stance acting as an intermediate gait.

6.5.1 Estimation of Domain of Attraction

Generally, determining the domain of attraction is a difficult task, even for low dimensional systems. However, for the system (6.10), the state space of which is six dimensional, we can provide suitable *estimates* of the domain of attraction of a bounding gait using quadratic Lyapunov functions [68] and sums of squares verification [95, 132].

For ease of implementation, the fixed point is translated to the origin. Since $\Delta z_f[k] = z_f[k] - \bar{z}_f$, (6.10) implies

$$\Delta z_f[k+1] = \mathcal{P}_2^{\text{cl}}(\bar{z}_f + \Delta z_f[k]) - \bar{z}_f . \quad (6.12)$$

which represents a map from $\Delta z_f[k]$ to $\Delta z_f[k+1]$; i.e.,

$$\Delta z_f[k+1] = \mathcal{P}_3^{\text{cl}}(\Delta z_f[k]) . \quad (6.13)$$

The fixed point corresponding to (6.13) is $\Delta z_f[k] = 0$ and its domain of attraction can be used to determine the domain of attraction of (6.10) in a straightforward manner.

A function $V(\Delta z_f)$ is a valid Lyapunov function for the discrete-time system (6.13) if $V(\Delta z_f)$ is positive definite and $V(\Delta z_f)[k+1] - V(\Delta z_f)[k] < 0$ in a bounded domain \mathcal{D} . Then, a subset of the domain of attraction can be defined as a sublevel of V ,

$$\mathcal{D}(\rho) := \{\Delta z_f \mid 0 \leq V(\Delta z_f) \leq \rho\} \quad (6.14)$$

where ρ is a positive scalar. Note that the linear optimal cost-to-go function (6.6) is a Lyapunov function for the nonlinear system (6.10). Thus by defining² $V(\Delta z_f) := J^*(\Delta z_f) = \Delta z_f' S \Delta z_f$, the problem of estimating the domain of attraction can be formulated as

$$\begin{aligned} & \max \rho \\ & \text{s.t. } \forall \Delta z_f \in \mathcal{D}(\rho), J_+^*(\Delta z_f[k]) < 0 \end{aligned} \quad (6.15)$$

where $J_+^*(\Delta z_f[k]) = J^*(\Delta z_f[k+1]) - J^*(\Delta z_f[k])$.

² Note that $\Delta z_f[k] = z_f[k] - \bar{z}_f$.

An analytically tractable way to verify that the Lyapunov function is decreasing within the domain \mathcal{D} is to formulate a sums-of-squares (SOS) feasibility problem [95, 132]:

$$\begin{aligned} & \max \rho \\ & \text{s.t. } h(\Delta z_f) \text{ is SOS} \end{aligned} \quad (6.16)$$

$$-J_+^*(\Delta z_f[k]) - h(\Delta z_f[k])(\rho - J^*(\Delta z_f[k])) \text{ is SOS}$$

where $h(\Delta z_f)$ is a positive definite polynomial of Δz_f , acting as a Lagrange multiplier. The sign of $(\rho - J^*(\Delta z_f[k]))$ is positive for all $\Delta z_f \in \mathcal{D}(\rho)$ by definition, and is negative outside this region. As a result, if (6.16) holds for any $h(\Delta z_f[k]) \geq 0$, then $-J_+^*(\Delta z_f[k]) > 0$ is satisfied, i.e., $J^*(\Delta z_f[k+1]) - J^*(\Delta z_f[k]) < 0$.

Note that the SOS algorithm requires $J_+^*(\Delta z_f[k])$ to be a polynomial [103]. However, in our case,

$$\begin{aligned} & J_+^*(\Delta z_f[k]) \\ &= \Delta z_f[k+1]'S\Delta z_f[k+1] - \Delta z_f[k]'S\Delta z_f[k] \\ &= \mathcal{P}_3^{\text{cl}}(z_f[k])'S\mathcal{P}_3^{\text{cl}}(z_f[k]) - \Delta z_f[k]'S\Delta z_f[k] , \end{aligned} \quad (6.17)$$

in which $\mathcal{P}_3^{\text{cl}}(z_f[k])$ is not available analytically; it is obtained through numerical integration. Hence, to proceed with the method, we approximate the return map (6.13) by expanding $\mathcal{P}_3^{\text{cl}}$ in Taylor series keeping terms up to second order; i.e.,

$$\mathcal{P}_3^{\text{cl}}(\Delta z_f[k]) \approx T_1\Delta z_f[k] + \Delta z_f[k]'T_2\Delta z_f[k] \quad (6.18)$$

where

$$T_1 = \left. \frac{\partial \mathcal{P}_3^{\text{cl}}}{\partial \Delta z_{f,i}} \right|_{\Delta z_f=0}, T_2 = \left. \frac{\partial^2 \mathcal{P}_3^{\text{cl}}}{\partial \Delta z_{f,i} \partial \Delta z_{f,j}} \right|_{\Delta z_f=0} \quad (6.19)$$

for $i, j \in \{1, 2, \dots, 6\}$. Substituting (6.18) into (6.17) yields

$$\begin{aligned} J_+^*(\Delta z_f[k]) &= (T_1\Delta z_f[k] + \Delta z_f[k]'T_2\Delta z_f[k])'S(T_1\Delta z_f[k] + \Delta z_f[k]'T_2\Delta z_f[k]) \\ &\quad - \Delta z_f[k]'S\Delta z_f[k] \end{aligned} \quad (6.20)$$

Given the polynomial expression (6.20), the SOS feasibility program in (6.16) can be solved by an available SOS toolbox, such as SOSTOOLS [103], and the maximum

value of ρ , i.e., ρ^{\max} , can be determined by searching for the value above which the SOS feasibility problem is infeasible.

With the value of ρ_0^{\max} available for a fixed point $\bar{z}_{f,0}$, a simple condition can be checked to determine if another fixed point $\bar{z}_{f,i}$ can “reach” \mathcal{D}_0 ; namely,

$$(\bar{z}_{f,i} - \bar{z}_{f,0})' S_0 (\bar{z}_{f,i} - \bar{z}_{f,0}) \leq \rho_0^{\max} . \quad (6.21)$$

Fig. 6.5 compares—for the bounding gait with double stance—the estimated domain of attractions by the Lyapunov-SOS method and the simulation-based method. In the simulation-based method, given the target fixed point, other source fixed points are taken as initial conditions and the hybrid controller Γ associated with the target fixed point is applied. If after 15 strides the error of the states from the nominal values is less than 5%, then the source fixed point $\bar{z}_{f,i}$ is regarded within the domain of attraction of the target fixed point. It can be seen that, although the Lyapunov-SOS method is more conservative than the simulation-based method, the estimated domain

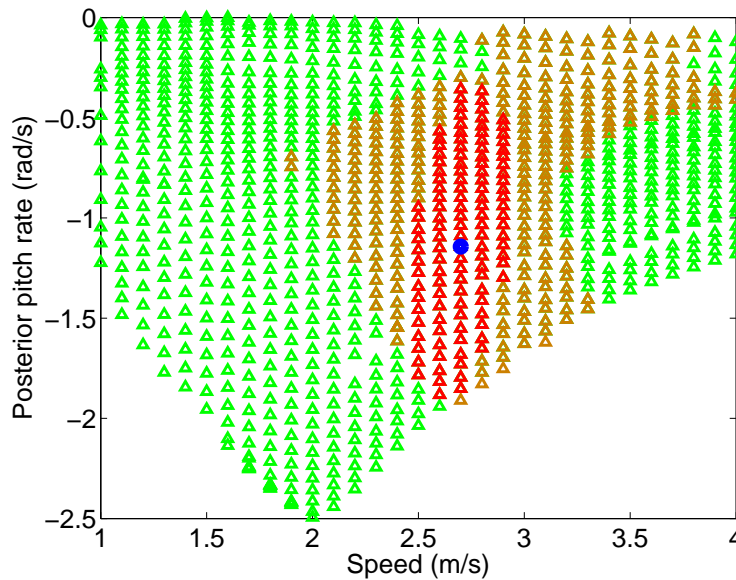


Figure 6.5: Fixed points that can be driven to a target fixed point (blue) within the bounding gait with double stance. The brown points are tested using the simulation-based method while the red points are predicted by the Lyapunov-SOS method.

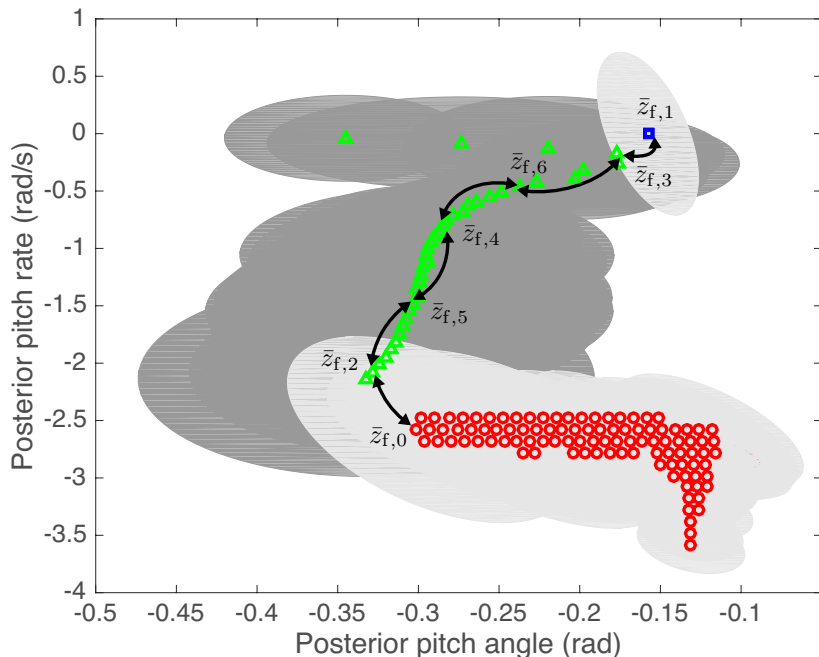


Figure 6.6: The transition between pronking and bounding without double stance in the $(\theta_p, \dot{\theta}_p)$ section. The blue square, red circle and green triangles represent the fixed points corresponding to pronking, bounding without double stance and bounding with double stance, respectively. The black arrows show one of the transition routes. The grey area represents the projection of the domain of attraction on the $(\theta_p, \dot{\theta}_p)$ plane.

of attraction is still reasonably large. In fact, as the next section shows, feasible gait transitions can be found based on the estimated domains of attraction obtained using the Lyapunov-SOS method.

6.5.2 Transitions Between Pronking and Bounding

Without loss of generality, we explore gait transitions at running speed 2.4m/s; see Fig. 6.6. It can be seen that within a gait – for example, bounding with double stance or bounding without double stance – transitions can be easily realized. In contrast, transitions from pronking to bounding without double flight are infeasible, i.e., $\bar{z}_0 \notin \mathcal{D}_1$ and $\bar{z}_1 \notin \mathcal{D}_0$, which confirms the predictions of Fig. 6.3(c). To bridge this gap, the bounding with double stance serves as intermediate gait between pronking and bounding without double stance, resulting in the following transition sequence:

$$\bar{z}_{f,0} \begin{array}{c} \xrightarrow{\Gamma_2} \\ \xleftarrow{\Gamma_0} \end{array} \bar{z}_{f,2} \begin{array}{c} \xrightarrow{\Gamma_5} \\ \xleftarrow{\Gamma_2} \end{array} \bar{z}_{f,5} \begin{array}{c} \xrightarrow{\Gamma_4} \\ \xleftarrow{\Gamma_5} \end{array} \bar{z}_{f,4} \begin{array}{c} \xrightarrow{\Gamma_6} \\ \xleftarrow{\Gamma_4} \end{array} \bar{z}_{f,6} \begin{array}{c} \xrightarrow{\Gamma_3} \\ \xleftarrow{\Gamma_6} \end{array} \bar{z}_{f,3} \begin{array}{c} \xrightarrow{\Gamma_1} \\ \xleftarrow{\Gamma_3} \end{array} \bar{z}_{f,1} \quad (6.22)$$

In Fig. 6.6, the arrows illustrate the two-way transition between pronking and bounding without double stance. In both directions, the transitions can be finished within 50 strides.

We remark that the proposed transition strategy can be used to enlarge the domain of attraction of the fixed points, drastically improving the capability of the system to reject large perturbations. For instance, when the bounding motion $\bar{z}_{f,0}$ is perturbed out of its original domain of attraction, the states cannot converge back to their nominal values by mere use of the corresponding controller Γ_0 . Yet, if the states are located within the domain of attraction of $\bar{z}_{f,5}$, then Fig. 6.6 shows that implementing Γ_5 , Γ_2 and Γ_0 sequentially realizes convergence to $\bar{z}_{f,0}$, provided that the system “spends” sufficiently long time in each mode. In fact, the two-way transition sequence (6.22) indicates that any states located within the domain of attraction of one of the fixed points in the sequence can be driven to any other fixed points in the sequence by suitably switching the parameters of the controller in (6.11). This requires that the system spends sufficiently long time with the control parameters tuned to a given fixed point, so that convergence is achieved; i.e., to go from $\bar{z}_{f,1}$ to $\bar{z}_{f,6}$ we switch to $\bar{z}_{f,3}$ first, then wait for sufficiently long time to enter the domain of attraction of $\bar{z}_{f,6}$ and then switch to $\bar{z}_{f,6}$. We cannot switch to $\bar{z}_{f,6}$ immediately after starting switch to $\bar{z}_{f,3}$. This implies that switching cannot be arbitrarily frequent; see [86] for more details on constrained switching for stability.

Chapter 7

ENERGETICS OF QUADRUPEDAL BOUNDING

To examine the relationship between elastic elements within the torso and the energy requirement for maintaining a gait, the basic model in Fig. 1.1(a) and 1.1(b) is extended to include non-trivial mass¹ in the legs, resulting in the model shown in Fig. 1.1(c), which is the model studied in this chapter. Section 7.1 describes, in a non-dimensional setting, two reductive quadrupedal models, one with and one without torso compliance; see also [23, 27]. Section 7.2 discusses the computation of cyclic bounding gaits in the context of the proposed models, and Section 7.3 proposes two energy efficiency metrics – namely, the mechanical and the metabolic cost of transport – to assess the energy requirements of the computed motions. Section 7.4 presents a comparison between the flexible- and rigid-torso models in the context of the mechanical cost of transport, and Section 7.5 demonstrates the ability of the flexible-torso model to predict the metabolic cost of transport of different quadrupedal animals.

7.1 Non-dimensional Reduced-order Models

To investigate the influence of torso compliance on the energetics of bounding, two sagittal-plane quadrupedal models with different torso configurations – one with a rigid non-deformable torso and one with a flexible segmented torso – are introduced; see Fig. 7.1. Both models have the same leg structure: an upper segment with mass m_{leg} and moment of inertia J_{leg} about its center of mass (COM) and a lower segment represented by a massless prismatic spring of stiffness k_{leg} . The natural length of the leg is denoted by l_0 , corresponding to the distance between the hip and the toe when

¹ That is, the COM of the leg is not located at the hip joint.

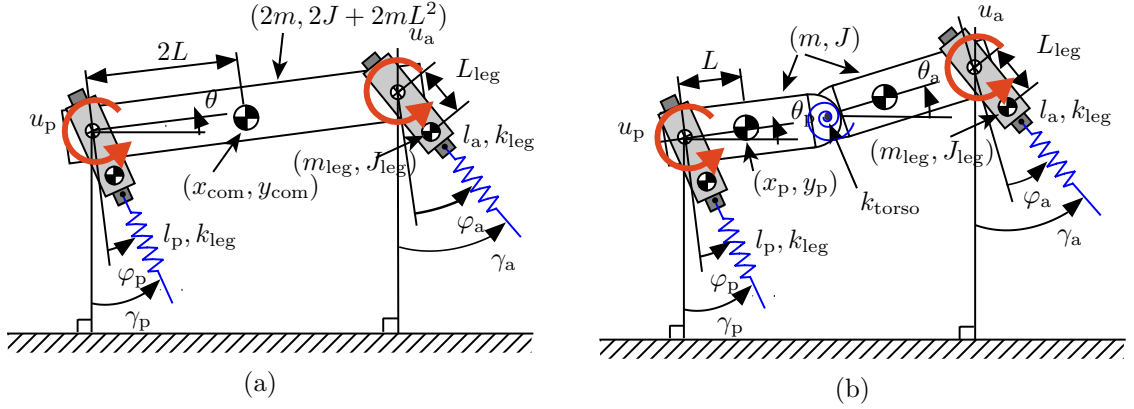


Figure 7.1: Two sagittal-plane quadrupedal models used to study the energetics of bounding motion. (a) Rigid-torso model; (b) Flexible-torso model. The red arrows at the hip joints represent actuator inputs. In the flexible-torso model, the torso joint is not actuated.

the leg spring is uncompressed. The distance between the COM of a leg and the corresponding hip joint is L_{leg} . In both models, the interaction between the toe and the ground is modeled as an unactuated, frictionless pin joint.

The two models of Fig. 7.1 differ only in their torso structure. In the flexible-torso model of Fig. 7.1(b), the torso consists of two identical segments: the anterior and posterior parts with mass m , moment of inertia J about their COM and hip-to-COM spacing L . A rotational spring is inserted between the two segments to introduce flexibility, producing a torque

$$\tau_{\text{torso}} = k_{\text{torso}} [(\theta_a - \theta_p) - \theta_{\text{rest}}] \quad , \quad (7.1)$$

where θ_a, θ_p are the pitch angles of the two segments as shown in Fig. 7.1(b), $\theta_{\text{rest}} < 0$ is the rest angle of the spring and k_{torso} is its stiffness. For fair comparison, the torso mass, hip-to-COM distance and moment of inertia of the torso about the COM in the rigid-torso model are $2m, 2L$ and $2J + 2mL^2$, respectively.

7.1.1 Continuous-time Dynamics in Non-dimensional Form

The bounding gait is the same as shown in Fig. 4.2, and we denote the gathered flight and extended flight as “fg” and “fe”, respectively. With reference to Fig. 7.1,

in each stance phase $i \in \{\text{sp}, \text{sa}\}$, the configuration space Q_i can be parameterized by the length of the leg in contact with the ground – that is, $l_p \in \mathbb{R}$ for the posterior and $l_a \in \mathbb{R}$ for the anterior stance phases – the leg angles $(\varphi_p, \varphi_a) \in \mathbb{S}^2$ relative to the torso, and the angles describing the configuration of the torso – namely, $(\theta_p, \theta_a) \in \mathbb{S}^2$ for the flexible-torso and θ for the rigid-torso model – i.e.,

$$q_i := \begin{cases} (l_p, \varphi_p, \varphi_a, \theta_p, \theta_a)' \in Q_i & \text{for } i = \text{sp}, \\ (l_a, \varphi_p, \varphi_a, \theta_p, \theta_a)' \in Q_i & \text{for } i = \text{sa}, \end{cases} \quad (7.2)$$

for the flexible-torso model, and

$$q_i := \begin{cases} (l_p, \varphi_p, \varphi_a, \theta)' \in Q_i & \text{for } i = \text{sp}, \\ (l_a, \varphi_p, \varphi_a, \theta)' \in Q_i & \text{for } i = \text{sa}, \end{cases} \quad (7.3)$$

for the rigid-torso model.

The flexible-torso model exhibits extended and gathered flight phases. In each of these phases, the configuration space Q_i , $i \in \{\text{fg}, \text{fe}\}$, can be parameterized by the Cartesian coordinates $(x_p, y_p) \in \mathbb{R}^2$ of the COM of the posterior part of the torso, the pitch angles $(\theta_p, \theta_a) \in \mathbb{S}^2$ of the posterior and anterior parts of the torso, together with the angles $(\varphi_p, \varphi_a) \in \mathbb{S}^2$ of the legs relative to the torso; i.e.,

$$q_i := (x_p, y_p, \varphi_p, \varphi_a, \theta_p, \theta_a)' \in Q_i \quad \text{for } i \in \{\text{fg}, \text{fe}\} . \quad (7.4)$$

Similarly, the flight phases of the rigid-torso model can be parameterized by the Cartesian coordinates $(x_{\text{com}}, y_{\text{com}}) \in \mathbb{R}^2$ of the COM of the torso, its pitch angle $\theta \in \mathbb{S}^1$, and the angles $(\varphi_a, \varphi_p) \in \mathbb{S}^2$ of the legs with respect to the torso; i.e.,

$$q_i := (x_{\text{com}}, y_{\text{com}}, \varphi_p, \varphi_a, \theta)' \in Q_i \quad \text{for } i \in \{\text{fg}, \text{fe}\} . \quad (7.5)$$

The equations that govern the motion of both models in all phases can be brought in state-space form as

$$\begin{aligned} \dot{x}_i &= f_i(x_i) + g_i(x_i)u_i \\ &= f_i(x_i) + g_{i,a}(x_i)u_{i,a} + g_{i,p}(x_i)u_{i,p} \end{aligned} \quad (7.6)$$

where $x_i := (q'_i, \dot{q}'_i)'$ is the state vector for each phase $i \in \{\text{sp, sa, fg, fe}\}$ evolving in $TQ_i := \{(q'_i, \dot{q}'_i)' \mid q_i \in Q_i, \dot{q}_i \in \mathbb{R}^{\dim(q_i)}\}$. The input $u_i := (u_{i,p}, u_{i,a})'$ includes the torques $u_{i,p}$ and $u_{i,a}$ applied at the posterior and anterior hip joints, respectively; see Fig. 7.1. Note that in both models, the hip torques are the only continuous-time inputs; the torso joint of the flexible-torso model in Fig. 7.1(b) is unactuated, and the torque developed between the posterior and anterior parts of the torso is solely due to the spring (7.1).

In (7.6), the physical properties of the each model are captured by the following parameters

$$\{m, m_{\text{leg}}, J, J_{\text{leg}}, l_0, L_{\text{leg}}, L, k_{\text{torso}}, k_{\text{leg}}\} . \quad (7.7)$$

As in Section 4.3.1, the number of physical parameters can be reduced by transforming the dynamics (7.6) to a non-dimensional form. Choosing the same characteristic time scale τ as in (4.5), the configuration variables defined in (7.2)-(7.5) and their derivatives with respect to time obtain the non-dimensional form:

$$\zeta^* := \frac{\zeta}{l_0}, \quad \dot{\zeta}^* := \frac{\tau \dot{\zeta}}{l_0}, \quad \ddot{\zeta}^* := \frac{\tau^2 \ddot{\zeta}}{l_0}, \quad (7.8)$$

for $\zeta \in \{x_p, y_p, x_{\text{com}}, y_{\text{com}}, l_p, l_a\}$ and

$$\psi^* := \psi, \quad \dot{\psi}^* := \tau \dot{\psi}, \quad \ddot{\psi}^* := \tau^2 \ddot{\psi}, \quad (7.9)$$

for $\psi \in \{\varphi_p, \varphi_a, \theta_p, \theta_a, \theta\}$ where the superscript “*” denotes a dimensionless quantity. Based on these transformations, the non-dimensional input torque u_i^* is defined as:

$$u_i^* := \frac{u_i}{mgl_0} . \quad (7.10)$$

Substitution of (7.8) and (7.9) into (7.6) reduces the parameters in (7.7) to the following seven dimensionless quantities:

$$\{I, M_{\text{leg}}, I_{\text{leg}}, d, d_{\text{leg}}, \kappa_{\text{torso}}, \kappa_{\text{leg}}\} , \quad (7.11)$$

the definitions of which are collected in Table 7.1 for convenience.

Table 7.1: Non-dimensional Parameters

Parameter	Value
Relative torso moment of inertia	$I := \frac{J}{mL^2}$
Relative leg mass	$M_{\text{leg}} := \frac{m_{\text{leg}}}{m}$
Relative leg moment of inertia	$I_{\text{leg}} := \frac{J_{\text{leg}}}{m_{\text{leg}}l_0^2}$
Relative hip-to-torso COM distance	$d := \frac{L}{l_0}$
Relative hip-to-leg COM distance	$d_{\text{leg}} := \frac{L_{\text{leg}}}{l_0}$
Relative torso stiffness	$\kappa_{\text{torso}} := \frac{k_{\text{torso}}}{mgl_0}$
Relative leg stiffness	$\kappa_{\text{leg}} := \frac{k_{\text{leg}}l_0}{mg}$

7.1.2 Event-based Transitions

The continuous-time phases are separated by the event-based transitions; namely, the touchdown and liftoff of the legs as in Fig. 4.2. The flight phase terminates when the vertical distance between the toe of either the posterior or the anterior leg and the ground becomes zero. Due to the non-negligible mass of the upper leg, an impact occurs at touchdown. To avoid complexity, the impacts will be modeled as in [142, Section 3.4] under the following assumptions:

- the toe colliding the ground neither rebounds nor slips;
- impacts are instantaneous;
- the actuator inputs can be ignored over an instantaneous impact;
- the forces applied by the ground during the impact can be represented by impulses;
- the impulsive forces result in instantaneous changes in velocities, but there is no instantaneous change in the configuration of the model.

Based on these assumptions, the flight phase dynamics can be integrated over the infinitesimally small duration of the impact to result in a linear map that is used to compute the states right after impact based on those right before; namely, $x_{\text{sa}}^{*+} = \Delta_{\text{fe} \rightarrow \text{sa}}(x_{\text{fe}}^{*-})$ for the anterior touchdown and $x_{\text{sp}}^{*+} = \Delta_{\text{fg} \rightarrow \text{sp}}(x_{\text{fg}}^{*-})$ for the posterior touchdown.

In general, transitions from stance to flight occur when the vertical ground reaction force (GRF) becomes zero and the vertical acceleration of the toe is directed upwards. To simplify the analysis, we will assume that liftoff occurs when the leg spring extends to its natural length, as adopted in [50].

7.1.3 Hybrid Dynamics of Bounding

Echoing the passive dynamics (4.1) of the energy-conservative model in Fig. 1.1 (a), the hybrid dynamics of bounding for the models in Fig. 7.1 that incorporate leg inertia and hip actuation can be represented by

$$\Sigma : \begin{cases} \dot{x}_i^* = f_i^*(x_i^*) + g^*(x_i^*)u_i^*, & x_i^{*-} \notin \mathcal{S}_{i \rightarrow i+1}^*, \\ x_{i+1}^{*+} = \Delta_{i \rightarrow i+1}(x_i^{*-}), & x_i^{*-} \in \mathcal{S}_{i \rightarrow i+1}^*, \\ \mathcal{S}_{i \rightarrow i+1}^* = \{x_i^* \in \mathcal{X}_i^* \mid H_{i \rightarrow i+1}(x_i^*) = 0, \dot{H}_{i \rightarrow i+1}(x_i^*) < 0\}, \end{cases} \quad (7.12)$$

for $i \in \{\text{fe, sa, fg, sp, f}\}$. In (7.12), u_i^* denotes the (non-dimensional) input torque at the hip joints in the continuous time and $H_{i \rightarrow i+1}$ represents the threshold function which can be easily determined according to Section 4.3.2.

7.2 Generation of Efficient Bounding Motions

Our purpose is to characterize the effect of torso flexibility on energy consumption and to assess the capacity of the flexible-torso model in predicting the energetic cost of transport in quadrupedal animal running. As a result, the objective of the controller used here to generate bounding is merely to recirculate the legs after liftoff and to replace the energy lost at impacts. No control action is developed for the leg that is in contact with the ground; the corresponding hip joint is *passive*, similarly to the passive bounding models studied in [89, 99, 35].

To make the comparison between the rigid-torso and the flexible-torso models as fair as possible, the proposed controllers will be developed using feedback linearization as in [142], and all the control parameters will be incorporated in the formulation of an optimization problem for computing running motions, thereby making their selection more systematic than manual gain tuning. Note that the generated bounding motions

are not necessarily stable, and further control action will be required in order to reject disturbances.

Finally, to avoid cumbersome notation, hereafter we neglect “ * ” with the understanding that all the variables are the non-dimensional ones defined in (7.8), (7.9) and (7.10).

7.2.1 Leg Recirculation Control

As was mentioned above, the leg that is in contact with the ground is completely passive. Control action is developed only at the hip joint of the leg that is in flight, and the objective of the controller is to recirculate the leg in anticipation of touchdown. In what follows, we describe the controller for the flexible-torso model; the corresponding controller for the rigid-torso model can be derived in an analogous fashion, and is omitted for brevity. Figure 7.2 summarizes the control inputs applied at the hip joints in each phase. Note that other control methods such as the PID controllers proposed by [34] can also be used.

The design of the controller begins by associating a scalar output function of the form

$$y_i = h_i(q_i, \alpha_i) := q_{c,i} - h_i^d(s_i(q_i), \alpha_i) , \quad (7.13)$$

to the dynamics (7.6) where $i \in \{\text{sa}, \text{fg}, \text{sp}, \text{fe}\}$. In (7.13), $q_{c,i}$ is the controlled variable and h_i^d represents its desired evolution that is parameterized via a set of parameters α_i as detailed below. The controlled variables are defined by

$$q_{c,i} := \begin{cases} \gamma_p = \varphi_p + \theta_p & \text{for } i \in \{\text{sa}, \text{fe}\}, \\ \gamma_a = \varphi_a + \theta_a & \text{for } i \in \{\text{sp}, \text{fg}\}. \end{cases} \quad (7.14)$$

In words, the controlled variable is selected to be

- the posterior absolute leg angle in the anterior stance and in the extended flight phases,
- the anterior absolute leg angle in the posterior stance and in the gathered flight phases.

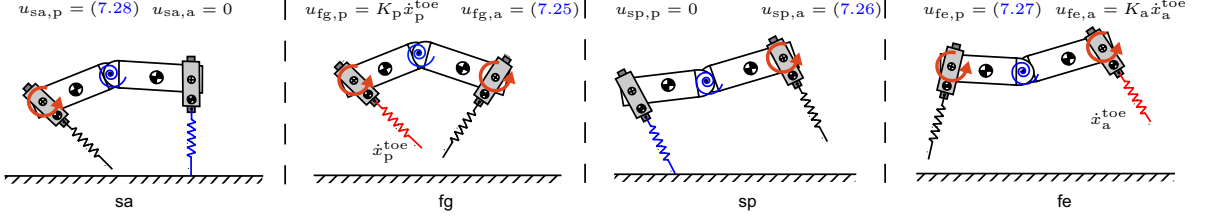


Figure 7.2: Summary of the control actions in different phases. From left to right: anterior stance, gathered flight, posterior stance and extended flight. The arrows at the hip joints signify the application of torque and the blue, red and black colors of the leg springs correspond to the hip actuation patterns that are employed at different phases: (i) The blue color implies that the corresponding hip joint is passive. (ii) The red color means that a swing-leg retraction controller is applied at the corresponding hip joint. (iii) The black color indicates that the absolute leg angle of the corresponding leg is selected as the controlled variable, $q_{c,i}$, in (7.13) to enforce coordination between the motion of the legs.

Designing the Constraints. In each phase $i \in \{sa, fg, sp, fe\}$, the desired evolution h_i^d in (7.13) is described via a 5-th order Beziér polynomial with coefficients $\alpha_i := \{\alpha_{i,k}\}_{k=0,\dots,5}$; i.e.,

$$h_i^d(s_i(q_i), \alpha_i) = \sum_{k=0}^5 b_{i,k}(s_i(q_i)) \alpha_{i,k} , \quad (7.15)$$

where the terms $b_{i,k}$ are given by

$$b_{i,k}(s_i) := \frac{5!}{k!(5-k)!} s_i^k (1-s_i)^{5-k} , \quad (7.16)$$

in which the dependence on q_i has been suppressed, and s_i is the strictly monotonic quantity

$$s_i := \frac{\gamma^{\max} - \gamma}{\gamma^{\max} - \gamma^{\min}} . \quad (7.17)$$

In (7.17),

$$\gamma := \begin{cases} \gamma_p & \text{for } i \in \{sp, fg\}, \\ \gamma_a & \text{for } i \in \{sa, fe\}, \end{cases} \quad (7.18)$$

and γ^{\max} and γ^{\min} are the maximum and minimum values of γ in the corresponding phase.

To provide more intuition, (7.13)-(7.18) imply that, in each phase, the evolution of the absolute angle of one leg (depicted in black color in Fig. 7.2) is determined by that of the other leg, which is either passive (blue color in Fig. 7.2) or follows a retraction controller (red color in 7.2) as is detailed below. For example, in the stance-anterior phase, the controlled variable is the absolute angle γ_p of the posterior leg according to (7.14) and its desired evolution h_{sa}^d is a function of the absolute angle γ_a of the anterior leg, as (7.17)-(7.18) imply. As a result, the output functions (7.13) depend only on the configuration variables q_i and the parameters α_i associated with the polynomials (7.15), and can therefore be interpreted as (virtual) holonomic constraints that coordinate the motion of the legs.

In what follows, we restrict our attention to bounding gaits in which the variable s_i defined by (7.17) is strictly monotonic with respect to time. This condition does not limit the motions that can be realized by the model, and it allows replacing time, effectively coordinating the motions of the legs with respect to an “internal” clock, as in [142]. In the stance phases, the monotonicity of s_i for $i \in \{sa, sp\}$ implies that the stance leg is continuously swept backward, as is normally the case in natural bounding motions. During the flight phases, the monotonicity of s_i can be guaranteed through proper choice of the coefficients of the Beziér polynomials in (7.15), in conjunction with a swing-leg retraction controller², such as the one proposed in [124].

To provide more details on ensuring the monotonicity of s_i , consider the gathered flight; i.e., s_{fg} . Prior to entering the gathered flight – that is, at the end of the anterior stance – known properties of the Beziér polynomials [142, Section 6.2] can be used to write the swing velocity of the posterior leg as

$$\dot{\gamma}_p = 5(\alpha_{sa,5} - \alpha_{sa,4})\dot{s}_{sa} . \quad (7.19)$$

² This controller has the additional advantage that it minimizes the horizontal speed of the toe relative to the ground at touchdown, thereby reducing the energy lost due to the impact and increasing the overall energy efficiency [50].

Since s_{sa} is strictly monotonically increasing in stance anterior³, i.e., $\dot{s}_{sa} > 0$, choosing $\alpha_{sa,5} < \alpha_{sa,4}$ will force the posterior leg to swing backward (that is, $\dot{\gamma}_p < 0$) at the beginning of the ensuing gathered flight phase. Choosing the input torque $u_{fg,p}$ during the gathered flight according to the prescription

$$u_{fg,p} = K_p \dot{x}_p^{toe} \quad , \quad (7.20)$$

where $K_p < 0$ and \dot{x}_p^{toe} is the forward velocity of the posterior toe relative to the ground allows us to make γ_p monotonically decreasing during the gathered flight. A similar procedure can be used to ensure the monotonicity of s_{fe} in the extended flight phase, resulting in introducing Beziér polynomial coefficients $\alpha_{sp,5} < \alpha_{sp,4}$ such that $\dot{\gamma}_a$ is negative at the end of posterior stance phase, i.e.,

$$\dot{\gamma}_a = 5(\alpha_{sp,5} - \alpha_{sp,4})\dot{s}_{sp} < 0 \quad , \quad (7.21)$$

and a gain $K_a < 0$ for the swing retraction controller, i.e.,

$$u_{fe,a} = K_a \dot{x}_a^{toe} \quad . \quad (7.22)$$

Note that K_p and K_a are incorporated in the parameters that are used in the optimization problem of section 7.3.

Imposing the Constraints. To impose the constraints (7.13) on the dynamics (7.6) we differentiate (7.13) twice with respect to (non-dimensional) time τ to obtain

$$\begin{aligned} \frac{d^2 y_i}{dt^2} &= L_{f_i}^2 h_i(x_i, \alpha_i) + L_{g_{i,a}} L_{f_i} h_i(q_i, \alpha_i) u_{i,a} \\ &\quad + L_{g_{i,p}} L_{f_i} h_i(q_i, \alpha_i) u_{i,p} \quad , \end{aligned} \quad (7.23)$$

where, in accordance with the notation in [142], $L_{f_i}^2 h_i$, $L_{g_{i,a}} L_{f_i} h_i$ and $L_{g_{i,p}} L_{f_i} h_i$ are the Lie derivatives of the output function h_i defined by (7.13) along the vector fields f_i , $g_{i,a}$ and $g_{i,p}$ that participate in (7.6). Since in each phase one of the hip torques in u_i is

³ This is because the anterior leg is continuously swept backwards during the stance-anterior phase.

either zero or determined by the swing-leg retraction controller (7.20) and (7.22), the other hip torque that participates in (7.23) can be determined so that

$$\frac{d^2 y_i}{dt^2} = 0 . \quad (7.24)$$

In more detail, in the gathered flight phase, the posterior torque $u_{fg,p}$ is determined by (7.20). Then, provided that $L_{g_{fg,a}} L_{f_{fg}} h_{fg}$ is invertible, the anterior hip input is given by

$$u_{fg,a} = -(L_{g_{fg,a}} L_{f_{fg}} h_{fg})^{-1} (L_{f_{fg}}^2 h_{fg} + L_{g_{fg,p}} L_{f_{fg}} h_{fg} u_{fg,p}) . \quad (7.25)$$

In the ensuing posterior stance phase, since the posterior leg is kept passive and no hip torque is applied, the anterior hip input is simply

$$u_{sp,a} = -(L_{g_{sp,a}} L_{f_{sp}} h_{sp})^{-1} L_{f_{sp}}^2 h_{sp} . \quad (7.26)$$

The input at the posterior joint in the extended flight and anterior flight phases can be derived in the same manner, resulting in

$$u_{fe,p} = -(L_{g_{fe,p}} L_{f_{fe}} h_{fe})^{-1} (L_{f_{fe}}^2 h_{fe} + L_{g_{fe,a}} L_{f_{fe}} h_{fe} u_{fe,a}) \quad (7.27)$$

and

$$u_{sa,p} = -(L_{g_{sa,p}} L_{f_{sa}} h_{sa})^{-1} L_{f_{sa}}^2 h_{sa} . \quad (7.28)$$

Closed-loop System. Fig. 7.2 summarizes the control action that is applied at the hip joints of the model in each phase. The same control strategy is employed to recirculate the legs in the rigid-torso model; the legs are actuated only when they are in flight, and the hip torque of the leg providing support is equal to zero. With the inputs at the hip joints as in Fig. 7.2, the dynamics (7.6) in each phase can be written in closed-loop form as

$$\dot{x}_i = f_i^{\text{cl}}(x_i, \alpha_i^{\text{cl}}) . \quad (7.29)$$

where $\alpha_i^{\text{cl}} = \alpha_i$ for $i \in \{\text{sa}, \text{sp}\}$, $\alpha_i^{\text{cl}} = \{\alpha_i, K_a, K_p\}$ for $i \in \{\text{fg}, \text{fe}\}$, and α_i includes all the parameters associated with the output functions for each phase. Consequently, the hybrid dynamic obtains the form:

$$\Sigma : \begin{cases} \dot{x}_i = f_i^{\text{cl}}(x_i, \alpha_i^{\text{cl}}), & x_i^- \notin \mathcal{S}_{i \rightarrow i+1}, \\ x_{i+1}^+ = \Delta_{i \rightarrow i+1}(x_i^-), & x_i^- \in \mathcal{S}_{i \rightarrow i+1}, \\ \mathcal{S}_{i \rightarrow i+1} = \{x_i \in \mathcal{X}_i \mid H_{i \rightarrow i+1}(x_i) = 0, \dot{H}_{i \rightarrow i+1}(x_i) < 0\}, \end{cases} \quad (7.30)$$

7.2.2 Poincaré Return Map

The Poincaré section is taken at liftoff of the anterior leg, i.e.,

$$\mathcal{S}_{\text{sa} \rightarrow \text{fg}} := \{x_{\text{sa}} \in TQ_{\text{sa}} \mid l_a - 1 = 0, \dot{l}_a > 0\} , \quad (7.31)$$

and the corresponding Poincaré return map $\mathcal{P} : \mathcal{S}_{\text{sa} \rightarrow \text{fg}} \rightarrow \mathcal{S}_{\text{sa} \rightarrow \text{fg}}$ is obtained by numerically integrating the closed-loop dynamics for each phase according to the phase sequence of Fig. 4.2. As a result,

$$x_{\text{sa}}[k+1] = \mathcal{P}(x_{\text{sa}}[k], \alpha^{\text{cl}}) , \quad (7.32)$$

where $x_{\text{sa}}[k]$ is the state at the end of the k -th anterior stance phase, and $\alpha^{\text{cl}} = \{\alpha_{\text{sa}}^{\text{cl}}, \alpha_{\text{fg}}^{\text{cl}}, \alpha_{\text{sp}}^{\text{cl}}, \alpha_{\text{fe}}^{\text{cl}}\}$ includes the parameters introduced by the continuous-time controllers of Section 7.2.1. Then, the problem of computing periodic bounding gaits becomes equivalent to finding a state vector x_{sa} so that

$$x_{\text{sa}} - \mathcal{P}(x_{\text{sa}}, \alpha^{\text{cl}}) = 0 \quad (7.33)$$

for suitable parameter values α^{cl} .

7.3 Methods: Searching for Fixed Points

We are interested in computing fixed points that minimize energy consumption at different speeds for the two models of Fig. 7.1. As a measure of the energy required to generate cyclic bounding motions, we use the *cost of transport (COT)*, a dimensionless quantity defined as the energy consumed over a distance divided by that distance and

the weight of the system; see Section 3.1.3. Depending on whether the energy dissipated within the motor units and the springs is considered, two variations of the COT are used.

7.3.1 Mechanical Cost of Transport

The mechanical COT, c_{mc} , characterizes the power delivered at the joints of the system, and is computed by

$$c_{\text{mc}} = \frac{1}{2(1 + M_{\text{leg}})TFr} \int_0^T (|u_{\text{a}}\dot{\varphi}_{\text{a}}| + |u_{\text{p}}\dot{\varphi}_{\text{p}}|)d\tau , \quad (7.34)$$

where T is the non-dimensional stride period and the rest of the variables have been defined in Section 7.1.1. The mechanical COT (7.34) is useful in comparing the rigid- and flexible-torso models of Fig. 7.1 from an “output” perspective – that is, from the point of view of the mechanics of the generated motion. Such comparison can determine the effect of various model parameters – including torso compliance – on the energetics of bounding, without relying on the specific characteristics of the actuators – motors or muscles – that are used to deliver the required power to the system’s joints.

7.3.2 Metabolic Cost of Transport

To assess the capacity of the proposed models to capture energy consumption in animal running, the definition of the COT needs to be extended so that it incorporates the efficiency of the motor units and the compliant members in injecting and recycling the energy required to sustain the motion. This is necessary because the mechanical COT is difficult to compute based on experimental data from animal running [3]. Instead, it is more convenient to measure oxygen consumption in experiments with running animals, from which the metabolic COT can be obtained; see Section 7.5.1 below for more details.

To capture the metabolic COT in animal running, we modify (7.34) in two ways. First, the efficiency of the motor units in performing positive and negative work is taken into account, so that the power required at the hip joints is computed as

$$P_1 = \frac{1}{\eta_1}([u_a \dot{\phi}_a]^+ + [u_p \dot{\phi}_p]^+) + \frac{1}{\eta_2}([u_a \dot{\phi}_a]^- + [u_p \dot{\phi}_p]^-) , \quad (7.35)$$

where

$$[P]^+ = \begin{cases} P & \text{if } P \geq 0, \\ 0 & \text{if } P < 0, \end{cases} \quad \text{and} \quad [P]^- = \begin{cases} 0 & \text{if } P \geq 0, \\ -P & \text{if } P < 0, \end{cases}$$

for $P \in \{u_a \dot{\phi}_a, u_p \dot{\phi}_p\}$ and η_1 and η_2 are the corresponding efficiencies. The definition of P_1 is based on the assumption that the metabolic energy consumed by muscles is roughly proportional to the mechanical power they generate, albeit with different efficiencies for positive and negative work [80]. Following [80], the coefficients η_1 and η_2 are then set as

$$\eta_1 = 0.25 \quad \text{and} \quad \eta_2 = 1.2 ,$$

where $\eta_2 > 1$ reflects the fact that muscles recycle part of the energy when doing negative work.

The second modification to (7.34) is modeling the leg and torso compliance via non-ideal springs that dissipate part of the mechanical energy as they deform during leg compression and decompression and torso flexion and extension.

Following [50], we will assume that the mechanical power dissipated in non-ideal springs is proportional to the power recycled by ideal springs so that

$$P_2 = \eta_3 \kappa_{\text{leg}} (|(1 - l_a)\dot{l}_a| + |(1 - l_p)\dot{l}_p|)$$

$$P_3 = \eta_3 \kappa_{\text{torso}} |(\theta_a - \theta_p - \theta_{\text{rest}})(\dot{\theta}_a - \dot{\theta}_p)| ,$$

where η_3 is a coefficient, which, based on physiological data regarding tendon efficiency provided by [96], is selected as

$$\eta_3 = 0.1 .$$

It should be emphasized that η_1 , η_2 and η_3 are *not* free parameters chosen by an optimization algorithm to achieve the best fit between simulation and experimental data from animal running. Instead, these coefficients are kept *constant* and equal to the biologically plausible values provided above, representing the efficiency of muscles when performing positive and negative work, and the efficiency of tendons in recycling mechanical energy. With these modifications to (7.34), the metabolic COT can be estimated by

$$c_{\text{mt}} = \frac{1}{2(1 + M_{\text{leg}})TFr} \int_0^T (P_1 + P_2 + P_3)d\tau . \quad (7.36)$$

7.3.3 Optimization

With the mechanical and metabolic COT defined by (7.34) and (7.36), respectively, the search for efficient bounding motions can be cast as a constrained optimization problem, in which the task is to find fixed points to (7.33) that minimize the corresponding COT; i.e.,

$$\begin{aligned} \mathbf{min} \{ & c_{\text{mc}}(x_{\text{sa}}, \alpha^{\text{cl}}) \text{ or } c_{\text{mt}}(x_{\text{sa}}, \alpha^{\text{cl}}) \} \\ \text{such that } & x_{\text{sa}} = \mathcal{P}(x_{\text{sa}}, \alpha^{\text{cl}}). \end{aligned} \quad (7.37)$$

This problem is solved using MATLAB's `fmincon`.

7.4 Results: Mechanical COT

In this section, the effect of torso compliance on the mechanical COT of bounding will be discussed in the context of the two models introduced in Section 7.1. Through detailed parametric studies, the main factors that affect the mechanical COT of the system are investigated and conclusions that are helpful in designing efficient quadrupedal robots with torso compliance are drawn.

7.4.1 Comparison of the Mechanical COT

Using the optimization framework described in Section 7.2, the mechanical COT of bounding gaits that are realized in both the rigid and flexible torso models can be compared for different speeds and physical parameters.

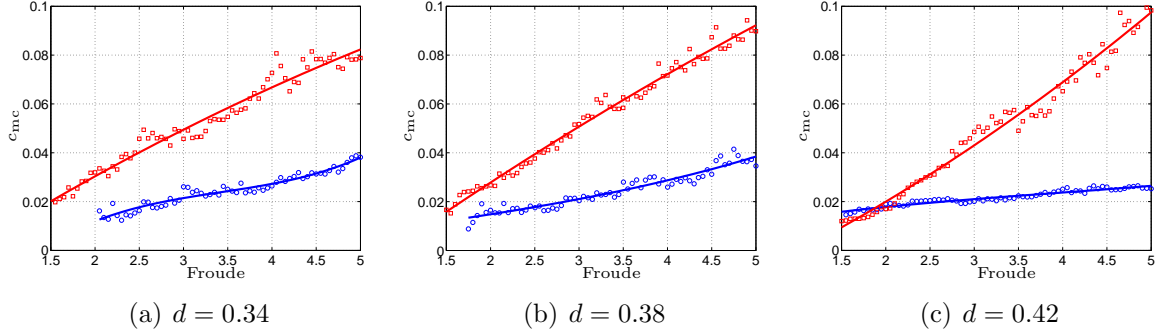


Figure 7.3: The mechanical COT of flexible-torso (blue circles) and rigid-torso (red squares) models of different speeds and relative hip-to-COM distances. The continuous lines are fitted third degree polynomials.

We begin our discussion with Fig. 7.3, which shows the mechanical COT computed for different dimensionless hip-to-COM distances $d \in \{0.34, 0.38, 0.42\}$ and for various traveling velocities, as these are captured by the Froude number $Fr \in [1.5, 5.0]$, which roughly describes the running speed range of most animals [2]. In interpreting these results, note that $d := L/l_0$, so that a large value of d corresponds to a longer torso relative to the leg length. The rest of the parameters are kept constant and are given in Table 7.2. It should be mentioned that all the bounding motions computed based on the flexible-torso model and depicted in Fig. 7.3 exhibit pronounced torso oscillations.

It is clear from Fig. 7.3 that the energy consumption increases with the traveling speed in both models. Furthermore, there exists a threshold value for the Froude

Table 7.2: Non-dimensional Mechanical Parameters of the Models

Parameters	Values
I	1.8
M_{leg}	0.1
I_{leg}	0.01
d_{leg}	0.25
κ_{leg}	25.8
κ_{tor}	5.5
θ_{rest}	-0.17

number, below which it was either impossible to compute fixed points in the flexible-torso model, as in Fig. 7.3(a) and 7.3(b), or the fixed points resulted in relatively higher mechanical COT than those of the rigid-torso model, as in Fig. 7.3(c). This observation implies that the benefits of torso flexibility in terms of energy efficiency are most appreciated at higher traveling speeds. This is evident from Fig. 7.3, where it is seen that the difference between the mechanical COT for the flexible- and rigid-torso models is amplified at higher Froude numbers.

Finally, Fig. 7.3(c) shows that the threshold value for the Froude number beyond which the flexible-torso model becomes more efficient is approximately equal to 1.8. It is interesting to note that this value corresponds to the transition from trotting to galloping, which is the same in animals with drastically different morphologies [2], such as horses and dogs [62, 77].

7.4.2 Torso Oscillation and Energy Efficiency

The models of Section 7.1 effectively capture the energetic cost of recirculating the legs in flight, and thus allow the assessment of the contribution of the flexible torso to the efficiency of the gait. In fact, the improved efficiency of the flexible-torso model observed in Fig. 7.3 can be attributed to the torso’s dorsoventral oscillations: as the torso flexes it facilitates the motion of the anterior leg backward and of the posterior leg forward, and vice versa when the torso extends.

In more detail, Fig. 7.4 shows the evolution of the absolute and relative leg angles for one of the fixed points of Fig. 7.3(c); namely, the fixed point corresponding to $d = 0.42$ and $Fr = 3.0$. It can be seen from Fig. 7.4 that, for the rigid-torso model, the evolution of the absolute angle of the posterior, γ_p , and anterior, γ_a , legs does not differ significantly from that of the corresponding relative angles φ_p and φ_a . By way of contrast, the differences between γ_p and φ_p , and γ_a and φ_a are much larger in the flexible-torso model. Note that the relative and absolute leg angles of fixed points of the flexible-torso model shown in Fig. 7.3(c) corresponding to $Fr > 1.8$ present similar behavior to that in Fig. 7.4.

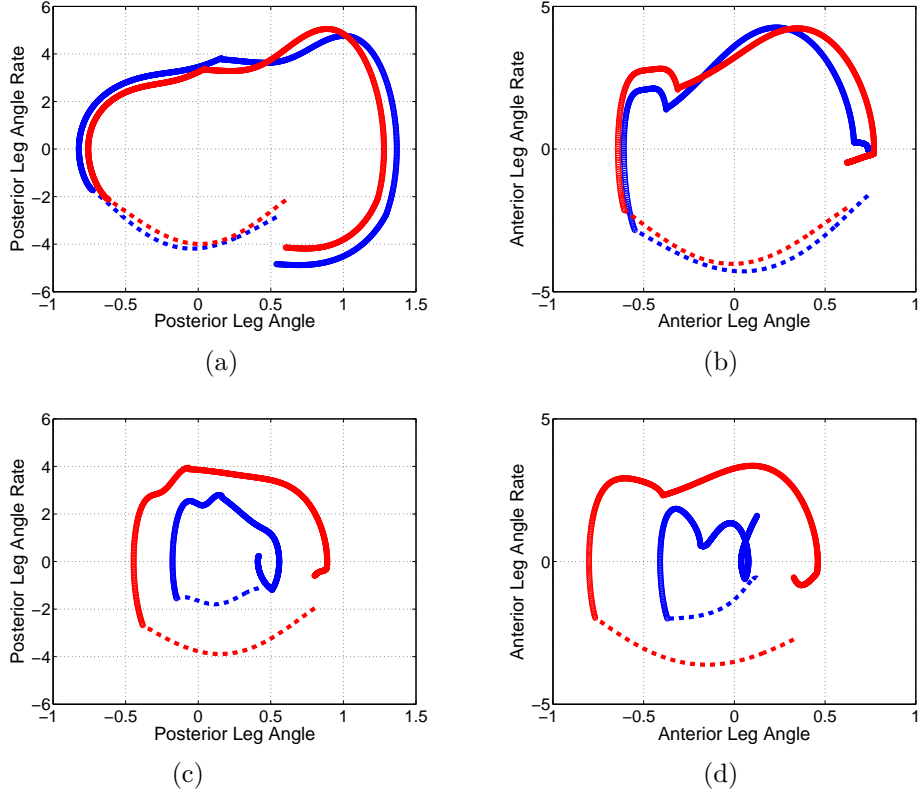
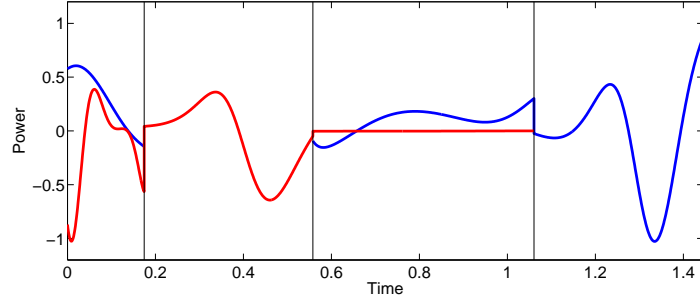
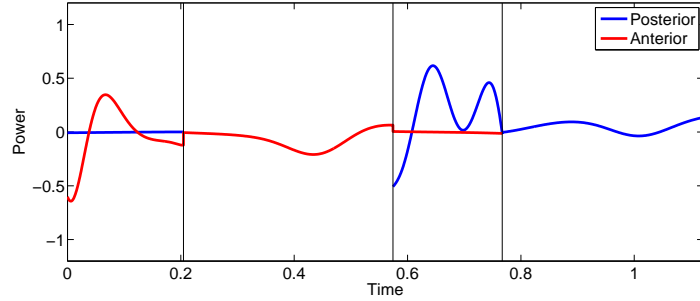


Figure 7.4: Absolute (red) and relative (blue) leg angles for a bounding gait at $Fr = 3.0$ with $d = 0.42$ for rigid-torso (a, b), and flexible-torso (c, d) models. The dotted line represent the stance phase. The discontinuity in leg angle rate is due to the impacts at touchdown.

Unlike the pitch motion of the rigid-torso model – which shows little effect on leg recirculation – the torso’s oscillation in the flexible-torso model significantly contributes to repositioning the leg during flight. Note though that as the value of the Froude number decreases, the difference between γ and φ in the flexible-torso model becomes smaller due to the decreased amplitude of the torso oscillation, the contribution of which to energy efficiency is reduced until it diminishes for $Fr < 1.8$. Fig. 7.5 shows the input power during one stride of the fixed points depicted in Fig. 7.4. During the stance phases “sa” and “sp”, Figs. 7.5(a) and 7.5(b) show that the hip power required to place the corresponding swing leg forward in anticipation of touchdown is much smaller when torso flexibility is present indicating that it acts as



(a)



(b)

Figure 7.5: Power of the posterior (blue) and anterior actuators (red) in one stride of the rigid-torso model (a) and the flexible-torso model (b). The vertical lines separate the four phases; from left to right: flight-gathered (fg), stance-posterior (sp), flight-extended (fe), and stance-anterior (sa).

an effective energy-saving mechanism. It is reminded that during the stance phase no torque is applied at the hip joint of the leg providing support.

Finally, figure 7.6 shows the stride frequency and length of the bounding motions presented in Fig. 7.3. It can be seen that as the forward speed increases, the stride frequency of the flexible-torso model remains almost constant. Correspondingly, a linear increasing relationship exist between the forward speed and the stride length for the flexible-torso model. This observation is consistent with biological data in [59, 77] showing that, at high-speed running gaits, quadrupedal mammals increase their velocity by increasing stride length instead of stride frequency.

7.4.3 Other Parameters

Torso Stiffness. In Chapter 4, it was shown that the stiffness of the torso

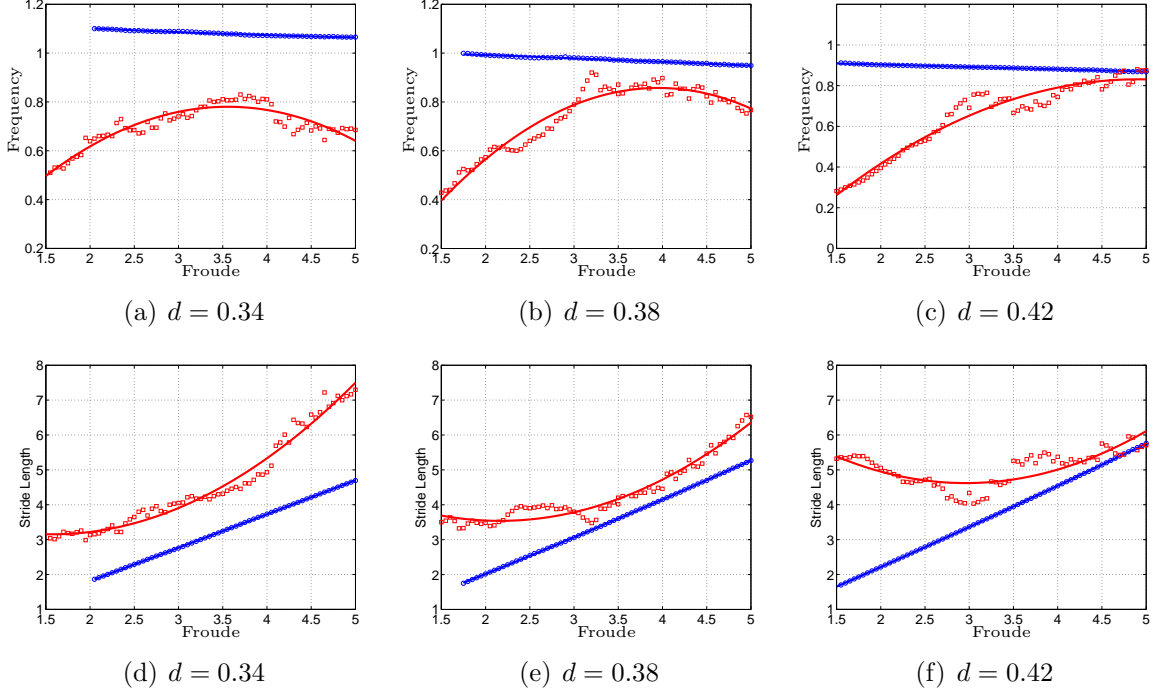


Figure 7.6: The stride frequency (a, b, c) and stride length (d, e, d) of flexible-torso (blue circles) and rigid-torso (red circles) models at different speed and relative hip-to-COM distance. The continuous lines are fitted 3rd-order polynomials.

spring has a significant effect on both motion generation and gait stability; here, we investigate its relationship with gait efficiency as shown in Fig. 7.7(a). For low stiffness, the mechanical COT increases linearly as the Froude number increases. However, for stiffer torso springs, the linear relationship between the mechanical COT and the Froude number becomes parabolic. This implies that when the torso stiffness is high enough, there is an optimal velocity that results in minimum energy consumption. Note that this parabolic dependence resembles the COT of a galloping horse [62, 84]. Furthermore, it is interesting to note that within the parabolic dependency region ($\kappa_{\text{torso}} > 5.5$), the mechanical COT achieves its minima at a specific Froude number (≈ 3.0), which is independent of the value of the torso stiffness as indicated by Fig. 7.7(a).

Finally, figure 7.7(b) shows the *dimensionless* stride frequency of the fixed points in Fig. 7.7(a). It can be seen that, for the same *relative* torso stiffness, κ_{tor} , the

dimensionless stride frequency is almost constant over a range of values of the Froude number, as was seen in Figs 7.6(a)–7.6(c). Furthermore, as the relative torso stiffness increases, the nearly constant relationship between the stride frequency and the Froude number shifts to higher frequency values.

Leg Mass. Another factor significantly affecting the mechanical COT is the mass of the leg. Larger mass requires larger torque to recirculate the leg, and it also results in larger energy dissipation at impacts [9, 122]. As expected, Fig. 7.8 shows that the mechanical COT of the flexible-torso model increases with the leg mass. Furthermore, increasing the mass of the leg appears to have a larger effect at higher speeds, suggesting that light leg design is critical for quadrupedal robots that are intended to realize high-performance, efficient running motions [9, 122].

7.5 Results: Metabolic COT

In previous sections, the influence of certain model parameters on the energetics of bounding with and without torso flexibility has been examined in the context of the mechanical COT. In this section, we turn our attention to assessing the ability of the proposed models to capture the energetics of quadrupedal *animal* running. In particular, the usefulness of the flexible-torso and the rigid-torso models as predictive

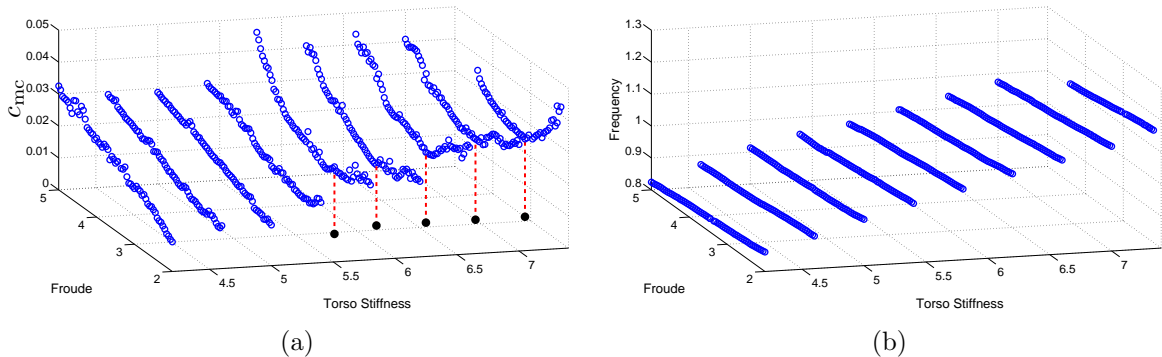


Figure 7.7: (a) The relationship between the torso stiffness and the mechanical COT at different speeds. The black dots are the projections of the points with minimal mechanical COT. (b) The relationship between the torso stiffness and the stride frequency at different speeds.

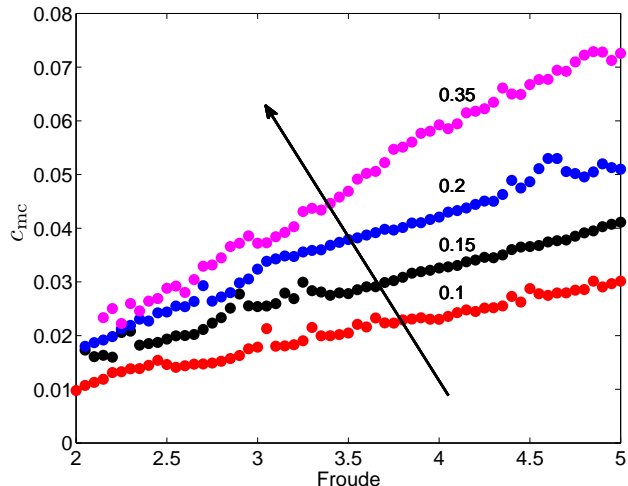


Figure 7.8: COT of the flexible-torso model with relative leg mass $M_{\text{leg}} \in \{0.1, 0.15, 0.2, 0.35\}$, $d = 0.38$ and $k_{\text{tor}} = 5.5$. Note that $M_{\text{leg}} := m_{\text{leg}}/m$.

tools for computing the efficiency of fast running motions of quadrupedal animals of different morphological characteristics is investigated. Most important, it is deduced that the flexible-torso model, suitably adapted to the geometric and morphological characteristics of different quadrupedal animals, can capture their metabolic COT, as this is estimated based on experimental data.

7.5.1 Animal Data and Computations

In our analysis, four animal species – namely, the horse (*Equus caballus*), the cheetah (*Acinonyx jubatus*), the gazelle (*Gazella gazella*) and the dog (*Canis familiaris*) – are considered, primarily due to the availability of data of oxygen consumption while running at high speeds.

Metabolic COT and Froude Number. In general, the mechanical COT is difficult to obtain using animal data [3]; instead, the metabolic COT is more easily accessible on the basis of measurements of oxygen consumption. In more detail, the metabolic COT of animal running is computed from data on the mass-specific rate of oxygen consumption given the energy produced by a unit volume of oxygen and the corresponding running speed as in [84], see also (3.4).

In more detail, the oxygen consumption rate of the horse is taken from [37] with running speeds in the range $\{7, 8, 9, 10, 11, 12, 13\}$ m/s. The Froude number corresponding to each speed is computed under the assumption that the leg length is 1.3m, the same as the Dutch Warmblood horse with a similar weight (500kg) [18]. The metabolic COT of the dog is obtained from [72], where data from running at $\{5, 6, 7\}$ m/s are provided. The leg length is set at 0.5m based on the morphological measurements of a dog with similar weight (25kg) in [39]. Finally, the oxygen consumption rate of the cheetah and the gazelle are obtained from [131], at speeds $\{4.75, 5.52\}$ m/s for the cheetah and $\{5.02, 5.28, 5.71, 6.13\}$ m/s for the gazelle. The corresponding leg lengths are obtained from the same paper. Note that for all the animals, only the metabolic data at high running speeds ($Fr > 1.8$) are included for comparison with the model prediction.

Non-dimensional Model Parameters. For a fair comparison between the model-predicted metabolic COT and the one estimated from biological data (3.4), the non-dimensional parameters that participate in the definition of the models, and are listed in Table 7.1, must be computed using the corresponding inertia, geometric and stiffness properties of the animals for which metabolic data are available. Clearly, it is difficult – if not impossible – to obtain measurements of all the required animal properties from the relevant literature. Yet, some non-dimensional parameters can be computed directly based on animal data; these parameters are given in bold in Table 7.3. Other parameters – such as the relative torso stiffness κ_{tor} , for example – are not accessible from animal data. For these parameters, a range of values is examined when computing the model-predicted metabolic COT as is described below.

Table 7.3: Non-dimensional Physical Parameters of Certain Animals

Species	I	d	M_{leg}	I_{leg}	d_{leg}	κ_{leg}	κ_{tor}
Horse	1.2	0.34	0.24	0.03	0.30	28	[4.0, 7.0]
Dog	1.1	0.36	0.21	0.06	0.32	22	[4.0, 7.0]
Cheetah	[0.9, 1.3]	0.36	0.40	[0.02, 0.08]	0.25	[20, 30]	[4.0, 7.0]
Gazelle	[0.9, 1.3]	0.36	0.31	[0.02, 0.08]	0.03	[20, 30]	[4.0, 7.0]

In more detail, all the geometric and inertia⁴ properties of the horse are calculated from anatomic data that are available for the Dutch Warmblood horse [18]. The corresponding leg stiffness is adopted from [57]. For the dog, the torso mass, length and moment of inertia are taken from [116] and [115] and the leg stiffness is obtained from [39]. The COM position of the leg and the leg mass are based on data from magnetic resonance image analysis provided in [8]. Finally, for the cheetah and the gazelle, the torso mass, leg length, leg mass and the COM position of the leg are taken from [131], resulting in the values of $\{d, M_{\text{leg}}, d_{\text{leg}}\}$ that are given in table 7.3.

As was mentioned above, not all the required model parameters are accessible from animal data published in the relevant literature. Thus, a range of possible values for these unknown parameters is considered. One such parameter is the relative torso stiffness κ_{tor} , which in all the four species is assumed to take values in the range [4.0, 7.0]. Furthermore, for the cheetah and the gazelle, it was not possible to extract values for the relative moment of inertia of the torso segments and the leg as well as the relative stiffness of the leg. For these animals, the range of values for I and I_{leg} were chosen as [0.9, 1.3] and [0.02, 0.08] respectively to include the corresponding values of the horse and the dog; see Table 7.3. The range of κ_{leg} was selected as [20, 30] capturing the leg stiffness values of many quadrupedal animals [39]. It is important to mention that in computing the metabolic COT, the overall range of values of the parameters $\{I, I_{\text{leg}}, \kappa_{\text{leg}}, \kappa_{\text{torso}}\}$ is discretized and all possible combinations of values are considered, as is detailed in the following section.

Computations. With the parameter values of Table 7.3, both the flexible- and the rigid-torso models are particularized to the morphology of each of the animals in consideration, for which measurements of oxygen consumption are available. The

⁴ Note that the moment of inertia J of half the torso is required in order to compute the dimensionless moment of inertia I ; see Table 7.1 for the definition of I . However, J is not directly available from animal data; yet, the moment of inertia of the whole torso can be found in the relevant literature. Then, a reasonable approximation of J can be obtained given the torso mass m and the torso length L by assuming the moment of inertia of the whole torso is $2J + 2mL^2$ and solving for J as mentioned in Section 7.1.

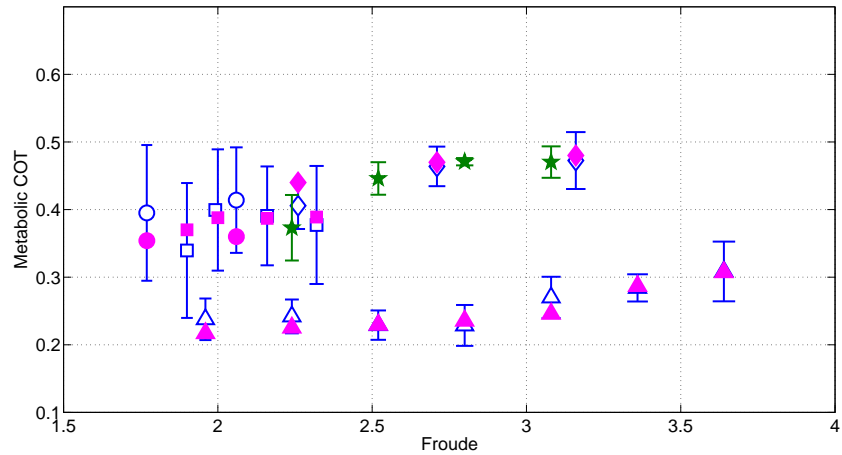
resulting models are then used to compute energy-efficient bounding motions that minimize the metabolic COT defined by (7.36) according to the procedure outlined in Section 7.3. The results are shown in Fig. 7.9, which – at different values of the Froude number – presents the metabolic COT predicted based on the flexible-torso (Fig. 7.9(a)) and on the rigid-torso (Fig. 7.9(b)) models together with the one obtained by (3.4) using measurements of oxygen consumption found in the relevant literature.

In interpreting Fig. 7.9 note that for each of the animals considered, and at each value of the Froude number, a collection of values of the (minimum) model-predicted metabolic COT is computed; each of these values corresponds to a different combination of model parameters I , I_{leg} , κ_{leg} and κ_{tor} , in the range given in Table 7.3. To ease computations, the ranges of the parameters are discretized as $\{0.9, 1.1, 1.3\}$ for I , $\{0.02, 0.04, 0.06, 0.08\}$ for I_{leg} , $\{20, 25, 30\}$ for κ_{leg} , and $\{4.0, 5.0, 6.0, 7.0\}$ for κ_{tor} . Note that not all the combinations of these discrete parameter values result in cyclic bounding motions; hence, Fig. 7.9 presents the average value and the corresponding standard deviation of the (minimum) metabolic COT corresponding to all the combinations of parameters for which bounding motions can be generated. The animal data are shown in magenta color while the model predicted data are shown in blue and red for the flexible-torso model and the rigid-torso model, respectively.

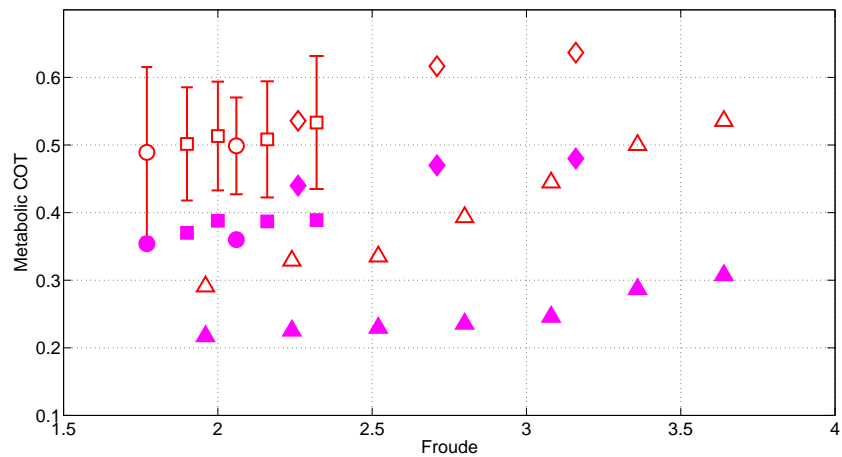
7.5.2 Discussion

The main conclusion from Fig. 7.9 is that the metabolic COT predicted by the flexible-torso model is in striking agreement – given the simplicity of the model as well as the inaccuracy of the parameter values – with the one computed using measurements of oxygen consumption from experiments with running animals. The largest deviation is observed in the gazelle and the cheetah – see also Table 7.4 – and is attributed to the fact that, for these two cases, only three out of the seven physical parameters required by the model are available based on direct morphological measurements; for the rest of the parameters, a range of possible values is considered, as shown in Table 7.3. On the other hand, the metabolic COT predicted by the rigid-torso model is consistently

larger than the one estimated using animal data. Particularly for the dog and the horse where animal data at larger values of the Froude number are available, the discrepancy between the rigid-torso model prediction of the metabolic COT and the one computed



(a)



(b)

Figure 7.9: The metabolic COT computed by (3.4) using oxygen consumption measurements (magenta filled symbols in both Fig.s) and the corresponding model-predicted values at different running speeds. (a) Flexible-torso model (blue open symbols); (b) Rigid-torso model (red open symbols). Four animal species are considered in the analysis; cheetah (circles), dog (diamonds), horse (triangles) and gazelle (squares). The metabolic COT values for the “test” model are represented by green stars. In both figures, the error bars signify the standard variation of the model-predicted data due to the range of the parameter values considered in the corresponding computations.

Table 7.4: Average deviation of model-predicted metabolic COT from animal data

Species	Flexible-torso model	Rigid-torso model
Horse	+13%	+38%
Dog	-4%	+29%
Cheetah	-2%	+34%
Gazelle	+3%	+60%

by animal data becomes more pronounced.

To further explore the differences between the flexible- and the rigid-torso models in predicting the metabolic COT, Fig. 7.10 provides information regarding the stride length and the non-dimensional stride frequency of the computed optimal motions and compares them with animal values for the cases of the dog and the horse, for which the corresponding data are available in [77] and in [37], respectively. It can be seen from Figs 7.10(a) and 7.10(b) that at sufficiently high values of the Froude number (above 2.6), the flexible-torso model captures the stride length and stride frequency of the horse more accurately than the rigid-torso model. For the case of the dog morphology, Figs 7.10(c) and 7.10(d) indicate that the rigid-torso model takes longer strides at lower frequency compared to the animal data, while the introduction of torso flexibility results in more accurate predictions of the stride length and frequency for the available speeds, which are all above 2.26.

Generally, to maintain high speeds in the absence of torso flexibility, the rigid-torso model requires larger angular excursions of the legs relative to the torso (flatter touchdown and liftoff angles) and sufficient angular rates. Clearly, this requirement increases the cost of transport due to the energy lost in the hip actuators to sustain leg recirculation. On the other hand, the flexible-torso model requires smaller angular excursions relative to the torso to maintain these high speeds; in this case, leg recirculation is facilitated by the torsos flexion and extension oscillations. Given that the torso oscillations are sustained by the non-ideal torso spring, which contributes less to the COT than the non-ideal motors that supply the hip torques required for leg recirculation, the flexible-torso model requires less energy to maintain high speeds.

In summary, the results in Figs 7.9 and 7.10 suggest that animals employ their torso at high speeds to avoid more pronounced leg motions that would otherwise be necessary to sustain such speeds. These leg motions would increase the energetic cost of transport due to the fact that fast and pronounced leg motions in the absence of torso flexion-extension oscillations would have to be realized primarily by the hip muscle units, the recruitment of which comes at a higher cost than that of elastic elements located in the animal's back – this issue is also discussed in Section 7.5.3 below; see also Fig. 7.11. Hence, the flexible-torso model offers a more reliable predictive tool of quadrupedal animal running than the rigid-torso model.

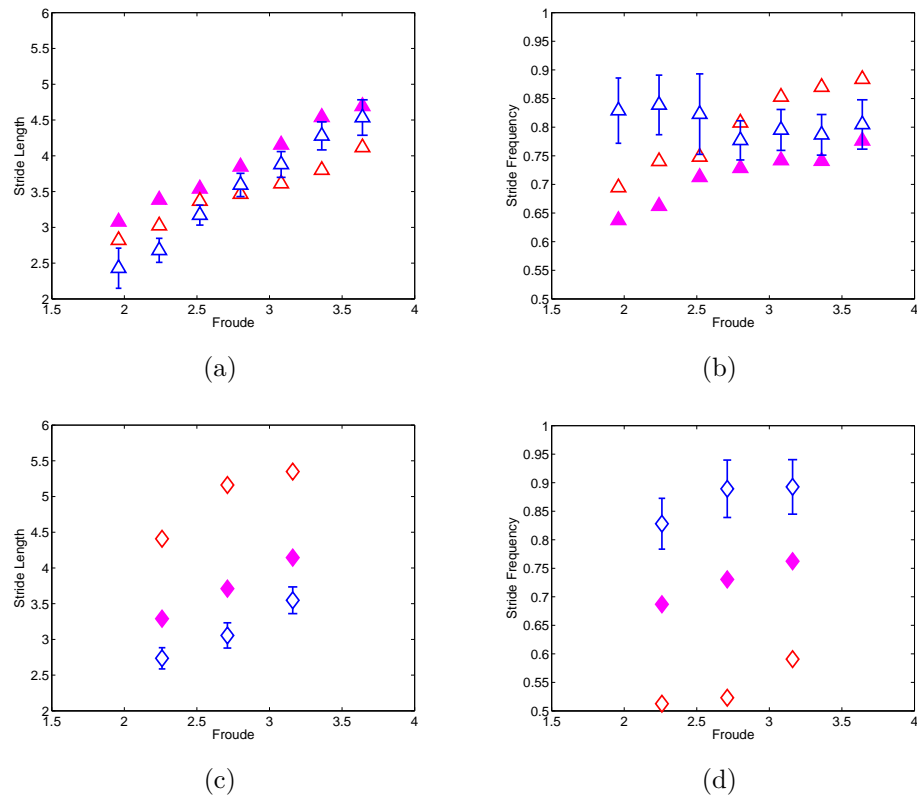


Figure 7.10: The stride length and the non-dimensional stride frequency of the energy efficient motions corresponding to the horse (a, b) and the dog (c, d) in Fig. 7.9. The animal data is represented by magenta filled symbols while the values predicted by the flexible torso and the values predicted by the rigid-torso are represented by blue and red symbols, respectively.

It should be emphasized that the computation of the metabolic COT for *different* animals using the *same* reduced-order model is conducted in a direct manner; that is, without relying on empirical formulas and data fitting *specific* to an animal as in [56, 57], for example. In our case, the energy required to sustain the motion is calculated directly from the model by incorporating non-ideal torque sources and elastic elements, with efficiencies that are kept constant and equal to the biologically plausible values of muscle and tendon efficiency provided in Section 7.3.2. Given that estimating the metabolic COT from oxygen consumption measurements of running animals requires cumbersome experimental procedures, the proposed approach offers a simple way to predict, in a relatively reliable fashion, the energetic requirements of running for different quadrupedal animals running at different velocities.

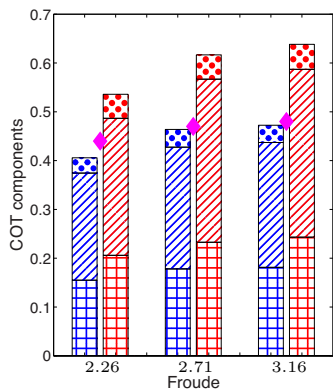
Finally, note that the inertia properties of the leg with respect to the hip joint dramatically affect energy economy. As Fig. 7.9 shows, regardless of the value of the Froude number, the metabolic COT of the dog is much larger – nearly double – than that of the horse, despite the fact that the relative leg mass of the dog, M_{leg} , is smaller than that of the horse. At first sight, this appears to contradict the results of Fig. 7.8, which shows that increasing the relative leg mass, M_{leg} , increases the mechanical COT. The reason is that Fig. 7.8 was obtained by changing M_{leg} *only*, keeping the rest of the parameters constant. Clearly though, the horse and the dog models differ in other parameters, which significantly influence energy consumption. In particular, the (dimensionless) moment of inertia of the leg with respect to the hip joint $M_{\text{leg}}d_{\text{leg}}^2 + I_{\text{leg}}$ in the two models is significantly different: 0.05 for the horse and 0.08 for the dog, i.e., 1.6 times that for the horse. This discrepancy, not only in the value of the relative mass, but in the distribution of the leg’s inertia about the hip joint can explain the lower efficiency of the dog model considered relative to the horse.

To further explore the dependence of the metabolic COT on the inertia properties of the leg – not just the relative mass M_{leg} – consider a “test” flexible-torso model in which the dimensionless quantities $\{M_{\text{leg}}, I_{\text{leg}}, d_{\text{leg}}\}$ characterizing the inertia properties of the leg obtain values equal to those of the dog model, while the rest

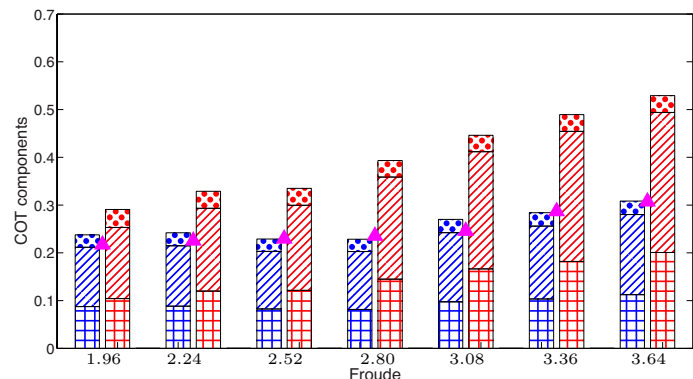
of the parameters $\{I, d, \kappa_{\text{leg}}, \kappa_{\text{tor}}\}$ are kept equal to those of the horse model considered. The corresponding metabolic COT for this test model is depicted in Fig. 7.9 for $Fr \in \{2.24, 2.52, 2.80, 3.08\}$. It can be seen that, despite the great discrepancy between the test and the dog models, the corresponding values of the metabolic COT are very close. This implies that the inertia properties of the leg $\{M_{\text{leg}}, I_{\text{leg}}, d_{\text{leg}}\}$ dominate the value of the metabolic COT. These observations indicate that a light-weight and small-inertia leg is crucial to energy economy, in agreement with [9, 122].

7.5.3 Metabolic and Mechanical COTs

To provide further intuition on how individual factors – i.e., the mechanics of the motion itself and the non-ideal actuators and springs used to sustain it – contribute to the computation of the metabolic COT, Fig. 7.11 presents the metabolic COT and its components. The data shown in Fig. 7.11 are obtained based on the flexible- and



(a) Model adapted to the morphology of the dog.



(b) Model adapted to the morphology of the horse.

Figure 7.11: The comparison of mechanical COT and metabolic COT for the flexible-torso (blue) and rigid-torso (red) models with the dog and horse physical parameters. The square pattern represents the mechanical COT. The diagonal pattern represents the increased value in COT when considering the efficiency of the actuators. The dot pattern represents the contribution of the non-ideal springs in the metabolic COT. The sum of these three component constitutes the metabolic COT shown in Fig. 7.9(a) and Fig. 7.9(b). The metabolic COT estimated based on animal data is represented by diamonds for the dog and by triangles for the horse, as in Fig. 7.9.

rigid-torso models adapted to the dog and the horse morphologies, for values of the Froude number at which animal data are available.

The mechanical COT captures merely the cost of leg recirculation, assuming ideal torque generating and elastic energy storing elements. Clearly, at the Froude number values of Fig. 7.11 the mechanical COT is larger for the rigid-torso model implying that torso flexibility reduces the energy requirement. Notice, however, that as the Froude number decreases, the difference between the mechanical COT predicted by the rigid-torso and the flexible-torso models decreases as well; see Fig. 7.11(b) at $Fr = 1.96$ for example. This is consistent with the comparison in Fig. 7.3.

As Fig. 7.11 shows, when non-ideal hip actuators are considered, the difference between the rigid-torso and the flexible-torso models is further amplified, particularly as the Froude number increases. This is clear from Fig. 7.11(b) and can be explained by the fact that leg recirculation in the rigid-torso model is realized predominantly through the hip actuators, which entail an energy cost that is higher compared to that of non-ideal springs in the torso. In fact, it is evident from Fig. 7.11 that the contribution of non-ideal springs to the metabolic COT is relatively smaller in size, implying that energy-efficient running can be achieved either by incorporating flexible elements in the torso to relief the hip actuators or by the design of highly-efficient actuators as in [122].

On a final note, a simple relation between the metabolic and the mechanical COT for a given periodic motion can be established. Under the assumption of a periodic motion, the energy supplied by the actuators doing positive work over a stride is equal to the energy lost in the actuators doing negative work plus the energy lost at the impacts with the ground during that stride, i.e.,

$$\int_0^T ([u_a \dot{\varphi}_a]^+ + [u_p \dot{\varphi}_p]^+) d\tau - \int_0^T ([u_a \dot{\varphi}_a]^- + [u_p \dot{\varphi}_p]^-) d\tau - |\Delta E_{\text{imp}}| = 0,$$

where ΔE_{imp} is the total energy lost at impacts over the stride. This implies,

$$\int_0^T ([u_a \dot{\varphi}_a]^- + [u_p \dot{\varphi}_p]^-) d\tau < \int_0^T ([u_a \dot{\varphi}_a]^+ + [u_p \dot{\varphi}_p]^+) d\tau,$$

and thus, the mechanical COT defined in (7.34) satisfies

$$c_{\text{mc}} < \frac{1}{2(1 + M_{\text{leg}})TFr} \int_0^T 2([u_{\text{a}}\dot{\varphi}_{\text{a}}]^+ + [u_{\text{p}}\dot{\varphi}_{\text{p}}]^+)d\tau . \quad (7.38)$$

On the other hand, for the metabolic COT defined in (7.34), since $P_2, P_3 > 0$

$$\begin{aligned} c_{\text{mt}} &> \frac{1}{2(1 + M_{\text{leg}})TFr} \int_0^T P_1 d\tau \\ &> \frac{1}{2(1 + M_{\text{leg}})TFr} \int_0^T \frac{1}{\eta_1} ([u_{\text{a}}\dot{\varphi}_{\text{a}}]^+ + [u_{\text{p}}\dot{\varphi}_{\text{p}}]^+) d\tau , \end{aligned}$$

where (7.35) and the facts that $\eta_2 > 0$ and $([u_{\text{a}}\dot{\varphi}_{\text{a}}]^- + [u_{\text{p}}\dot{\varphi}_{\text{p}}]^-) > 0$ have been used. In view of (7.38), the last inequality results in the simple relation

$$c_{\text{mt}} > \frac{1}{2\eta_1} c_{\text{mc}} . \quad (7.39)$$

Note that for the case where the efficiency of performing positive work is $\eta_1 = 0.25$ as in Section 7.3.2, (7.39) takes the particularly simple form

$$c_{\text{mt}} > 2c_{\text{mc}} . \quad (7.40)$$

A closer look at Fig. 7.11 reveals that at a given speed the minimum metabolic COT of a model is always more than two times of the mechanical COT, confirming (7.40). Given that the mechanical COT cannot be easily obtained in experiments with animals [3], (7.40) could be used to provide an upper bound of the mechanical COT on the basis of estimates of the metabolic COT using oxygen consumption measurements from running animals.

Chapter 8

EXTENSIONS TO HIGHER-DIMENSIONAL MODELS

This chapter completes the modeling and control hierarchy of Fig. 1.1 by incorporating torso actuation into the model in Fig. 1.1(c) to study the control of quadrupedal bounding with non-trivial leg inertia and torso flexibility, resulting in the model shown in Fig. 1.1(d). In Section 8.3, periodic bounding motions are generated simply by positioning the legs during flight via suitable (virtual) holonomic constraints that are imposed on the evolution of the leg angles; as in Chapter 7, no control effort is developed on legs that are in contact with ground, resulting in efficient, nearly passive, bounding gaits. In Section 8.4, the resulting motions are stabilized by a hybrid control law which coordinates the movement of the torso and the legs in continuous time, and updates the leg touchdown angles in an event-based fashion. Finally, in Section 8.5, sums-of-squares (SOS) programming is used to obtain formally verified estimates of the domain of attraction of stable fixed points, which are then employed to realize speed transitions by switching among different bounding gaits in a sequential fashion.

8.1 Model

Based on the quadrupedal model used to study energetic of bounding; see Fig. 7.1(b) and Fig. 1.1(c), an actuator is incorporated at the spinal joint which operates in parallel with the torsional spring in order to actively regulate the torso oscillation, resulting in the model shown in Fig. 1.1(d). The physical parameters of the model is shown in Table 8.1. Note that this model differs from the passive model in Fig. 4.1 in the non-zero leg mass and inertia, the values of which are shown in bold in Table 8.1.

8.2 Hybrid Dynamics of Bounding

With reference to Fig. 7.1(b), the configuration space of bounding dynamics can be defined by (7.2) for the stance phases and (7.4) for the flight phases. The equation that governs the motion of the model in all phases can be derived using Lagrangian method and are written in state-space form as

$$\begin{aligned}\dot{x}_i &= f_i(x_i) + g_i(x_i)u_i \\ &= f_i(x_i) + g_i^a(x_i)u_i^a + g_i^p(x_i)u_i^p + g_i^t(x_i)u_i^t\end{aligned}\tag{8.1}$$

where $x_i := (q'_i, \dot{q}'_i)'$ is the state vector for each phase $i \in \{\text{sp, sa, fg, fe}\}$ evolving in $TQ_i := \{(q'_i, \dot{q}'_i)' \mid q_i \in Q_i, \dot{q}_i \in \mathbb{R}^{\dim(q_i)}\}$ and $u_i := (u_i^p, u_i^a, u_i^t)'$ is the input vector. Note that compared with the continuous-time dynamics (7.6) of the model in Fig. 7.1(b), torso actuation u_i^t is incorporated into u_i in (8.1).

The continuous-time phases are separated by the event-based transitions, which are modeled the same as those in Section 7.1.2. Then, the hybrid dynamics of bounding obtains the same form as (7.12) except that all the quantities participate with their dimensions, as in Table 8.1.

8.3 Leg Recirculation: Generating Periodic Motions

The objective of this section is to generate periodic bounding motions with the model in Fig. 7.1(b). As was mentioned in Chapter 7, because of the leg mass and

Table 8.1: Mechanical Parameters of the Model

Parameter	Value	Units
Torso Mass (m)	10.432	kg
Torso Inertia (J)	0.36	kgm ²
Hip-to-COM Spacing (L)	0.138	m
Nominal Leg Length (l_0)	0.36	m
Leg Spring Constant (k_{leg})	7329	N/m
Torso Spring Constant (k_{torso})	203	Nm/rad
Leg Mass (m_{leg})	1	kg
Leg Inertia (I_{leg})	0.001	kgm ²
Hip-to-Leg COM Spacing (L_{Leg})	0.09	m

inertia introduced in this model, periodic motions cannot be generated passively, as was the case in Section 4. However, we can still take advantage of the passive dynamics associated with the torso and leg springs in exciting periodic motions. In more detail, as was the case in Section 7.2.1, in generating bounding motions, the torso joint will be unactuated throughout the phases while the hip joint is actuated only when the corresponding leg is in flight so that the controller merely swings the leg forward to the desired touchdown angle.

The design of the controller begins by associating an output function of the form

$$y_i = q_{c,i} - h_i^{\text{dl}}(s_i(q_i), \alpha_i, \beta_i) , \quad (8.2)$$

to the dynamics (8.1) where $i \in \{\text{sa}, \text{fg}, \text{sp}, \text{fe}\}$. In (8.2), $q_{c,i}$ is the controlled variable and h_i^{dl} represents its desired evolution that is parameterized via a set of parameters α_i, β_i as detailed below. The controlled variables are defined by

$$q_{c,i} := \begin{cases} \gamma_p = \varphi_p + \theta_p & \text{for } i = \text{sa}, \\ \gamma_a = \varphi_a + \theta_a & \text{for } i = \text{sp}, \\ (\gamma_p, \gamma_a)' & \text{for } i \in \{\text{fe}, \text{fg}\}. \end{cases} \quad (8.3)$$

In (8.2), $s_i \in [0, 1]$ is a monotonically increasing quantity defined as

$$s_i := \frac{x_{p,i}^{\text{max}} - x_p}{x_{p,i}^{\text{max}}} \quad (8.4)$$

where $x_{p,i}^{\text{max}}$ is the travelled distance of the COM of the posterior torso in each phase. Note that y_i is only a function of q_i and thus can be interpreted as a holonomic constraint imposed on the system via the hip actuators as described below.

8.3.1 Designing the Constraints

Posterior Stance. As was mentioned above, during the posterior stance phase, the hip joint of the leg in contact with the ground is unactuated $u_{\text{sp}}^p = 0$, and the only input acting on the system is applied at the hip of the anterior leg with the objective of placing the anterior leg at a desired touchdown angle. Hence, the dynamics (8.1) becomes

$$\dot{x}_{\text{sp}} = f_{\text{sp}}(x_{\text{sp}}) + g_{\text{sp}}^a(x_{\text{sp}})u_{\text{sp}}^a \quad (8.5)$$

The desired evolution $h_{\text{sp}}^{\text{d1}}$ of the absolute anterior leg angle is parameterized via a 3rd-order Beziér polynomial with coefficients $\alpha_{\text{sp}} := \{\alpha_{\text{sp},k}\}_{k=0,1}$ and $\beta_{\text{sp}} := \{\beta_{\text{sp},k}\}_{k=0,1}$; i.e.,

$$h_{\text{sp}}^{\text{d1}}(s_{\text{sp}}(q_{\text{sp}}), \alpha_{\text{sp}}, \beta_{\text{sp}}) = \sum_{k=0}^1 b_{\text{sp},k}(s_{\text{sp}}(q_{\text{sp}}))\alpha_{\text{sp},k} + b_{\text{sp},2}(s_{\text{sp}}(q_{\text{sp}}))\beta_{\text{sp},0} + b_{\text{sp},3}(s_{\text{sp}}(q_{\text{sp}}))\beta_{\text{sp},1} \quad , \quad (8.6)$$

where the terms $b_{\text{sp},k}$ are given by

$$b_{\text{sp},k}(s_{\text{sp}}) := \frac{3!}{k!(3-k)!} s_{\text{sp}}^k (1-s_{\text{sp}})^{3-k} \quad .$$

Using the properties of the Beziér polynomials,

$$h_{\text{sp}}^{\text{d1}}(1) = \beta_{\text{sp},1}, \quad \left. \frac{\partial h_{\text{sp}}^{\text{d1}}}{\partial s_{\text{sp}}} \right|_{s_{\text{sp}}=1} = 3(\beta_{\text{sp},1} - \beta_{\text{sp},0}) \quad . \quad (8.7)$$

which implies that selecting $\beta_{\text{sp},0} = \beta_{\text{sp},1}$ results in nominal bounding gaits where the anterior leg touches down at an angle equal to $\beta_{\text{sp},1}$ and with zero angular velocity.

Extended Flight. During the extended flight, the posterior leg swings forward while the anterior leg maintains a constant angle $\beta_{\text{sp},1}$ in anticipation of touchdown. The corresponding hip torques u_{sa}^{p} and u_{sa}^{a} are both available for control, and the output is defined as

$$h_{\text{fe}}^{\text{d1}}(s_{\text{fe}}(q_{\text{fe}}), \alpha_{\text{fe}}) = \begin{bmatrix} \sum_{k=0}^3 b_{\text{fe},k}(s_{\text{fe}}(q_{\text{fe}}))\alpha_{\text{fe},k} \\ \beta_{\text{sp},1} \end{bmatrix} \quad . \quad (8.8)$$

where α_{fe} includes the Beziér polynomial coefficients and b_{fe} is determined in a way analogous to (8.7).

Anterior Stance. During the anterior stance phase, the leg in contact with the ground is unactuated $u_{\text{sa}}^{\text{a}} = 0$, so that

$$\dot{x}_{\text{sa}} = f_{\text{sa}}(x_{\text{sa}}) + g_{\text{sa}}^{\text{p}}(x_{\text{sa}})u_{\text{sa}}^{\text{p}} \quad (8.9)$$

The desired evolution of the posterior leg angle is

$$h_{\text{sa}}^{\text{d1}}(s_{\text{sa}}(q_{\text{sa}}), \alpha_{\text{sa}}, \beta_{\text{sa}}) = \sum_{k=0}^1 b_{\text{sa},k}(s_{\text{sa}}(q_{\text{sa}}))\alpha_{\text{sa},k} + b_{\text{sa},2}(s_{\text{sa}}(q_{\text{sa}}))\beta_{\text{sa},0} + b_{\text{sa},3}(s_{\text{sa}}(q_{\text{sa}}))\beta_{\text{sa},1} \quad . \quad (8.10)$$

Again, we set $\beta_{\text{sa},0} = \beta_{\text{sa},1}$ so that the posterior leg arrives at the angle $\beta_{\text{sa},1}$ with zero angular velocity at the end of the anterior stance.

Gathered Flight. Similar to the extended flight phase, in the gathered flight phase, the posterior leg maintains a constant angle while the anterior leg evolves according to the output

$$h_{\text{fg}}^{\text{d1}}(s_{\text{fg}}(q_{\text{fg}}), \alpha_{\text{fg}}) = \begin{bmatrix} \beta_{\text{sa},1} \\ \sum_{k=0}^3 b_{\text{fg},k}(s_{\text{fg}}(q_{\text{fg}}))\alpha_{\text{fg},k} \end{bmatrix}. \quad (8.11)$$

Imposing the Constraints. To impose the constraints (8.2) on the dynamics (8.1) we differentiate (8.2) twice with respect to time to obtain

$$\frac{d^2 y_i}{dt^2} = L_{f_i}^2 y_i(x_i, \alpha_i, \beta_i) + L_{g_{i,a}} L_{f_i} y_i(q_i, \alpha_i, \beta_i) u_{i,a} + L_{g_{i,p}} L_{f_i} y_i(q_i, \alpha_i, \beta_i) u_{i,p}, \quad (8.12)$$

where $L_{f_i}^2 y_i$, $L_{g_{i,a}} L_{f_i} y_i$ and $L_{g_{i,p}} L_{f_i} y_i$ are the Lie derivatives of the output function y_i defined by (8.2) along the vector fields f_i , $g_{i,a}$ and $g_{i,p}$ that participate in (8.1); see [142] for detailed definitions. In each phase, the inputs available – i.e., $(u_{i,p}, u_{i,a})$ in the gathered and extended flight phases, $u_{i,p}$ in the anterior stance and $u_{i,a}$ in the posterior stance – are selected to ensure $\frac{d^2 y_i}{dt^2} = 0$.

8.3.2 Poincaré Map

The Poincaré section is taken at liftoff of the anterior leg, i.e.,

$$\mathcal{S} := \{x_{\text{fg}} \in TQ_{\text{fg}} \mid y_p - y_p^* = 0\}, \quad (8.13)$$

where $y_p^* = l_0 \cos(\theta_a + \varphi_a) + 2L \cos \theta_a - L \cos \theta_p$. By projecting out the monotonically increasing horizontal coordinate x_p from the state vector x_{fg} and substituting y_p through the condition defining (8.13), the (reduced) Poincaré map can be defined as

$$z[k+1] = \mathcal{P}_1(z[k], \alpha[k], \beta[k]), \quad (8.14)$$

where z represents the remaining states in x_{fg} , i.e.,

$$z := [\theta_p, \theta_a, \varphi_p, \varphi_a, \dot{x}_p, \dot{y}_p, \dot{\theta}_p, \dot{\theta}_a, \dot{\varphi}_p, \dot{\varphi}_a] \quad (8.15)$$

and $\alpha = \{\alpha_i, x_{p,i}^{\max}, x_{p,i}^{\min}\}$ for $i \in \{\text{sp, sa, fe, fg}\}$, $\beta = \{\beta_{\text{sa}}, \beta_{\text{sp}}\}$ including all the parameters participating in the development of leg recirculation controller. Then, the problem of computing periodic bounding gaits becomes equivalent to finding a state vector z so that

$$z - \mathcal{P}_1(z, \alpha, \beta) = 0 \quad (8.16)$$

for suitable parameter values α and β and is solved numerically using MATLAB's `fmincon`.

Fig. 8.1 shows the evolution of forward velocity x_p , torso oscillation $\theta_a - \theta_p$, absolute leg angles (γ_p, γ_a) and the hip torque input (u^p, u^a) of a representative fixed points. Note that in Fig. 8.1(b) there is only one complete torso oscillation in one stride, the same as the passively generated bounding motion in Chapter 4. Also, the maximum and minimum torso angle occur in the extended and gathered flight phases, corresponding to the concave and convex configurations, respectively.

8.3.3 Local Stability

To analyze the local stability properties of bounding, we linearize (8.16) at a fixed point \bar{z} assuming α and β are constants:

$$\Delta z[k+1] = A_1 \Delta z[k], \quad (8.17)$$

where $\Delta z = z - \bar{z}$ and $A_1 = \left. \frac{\partial \mathcal{P}_1}{\partial z} \right|_{z=\bar{z}}$. When the eigenvalues of A_1 are all within the unit disc, the corresponding fixed point is locally exponentially stable. The generated fixed points are not stable, thus a controller is necessary to sustain periodic bound orbits in the presence of perturbations.

8.4 Leg-torso Coordination: Stabilizing Periodic Motions

In Chapter 5, a hybrid controller has been proposed to stabilize nearly passive bounding motions in a model with massless legs. The controller introduces an active component u_i^t of the torso joint torque that acts in parallel with the torsional spring connecting the posterior and anterior parts of the torso. Then, u_i^t is used as a control

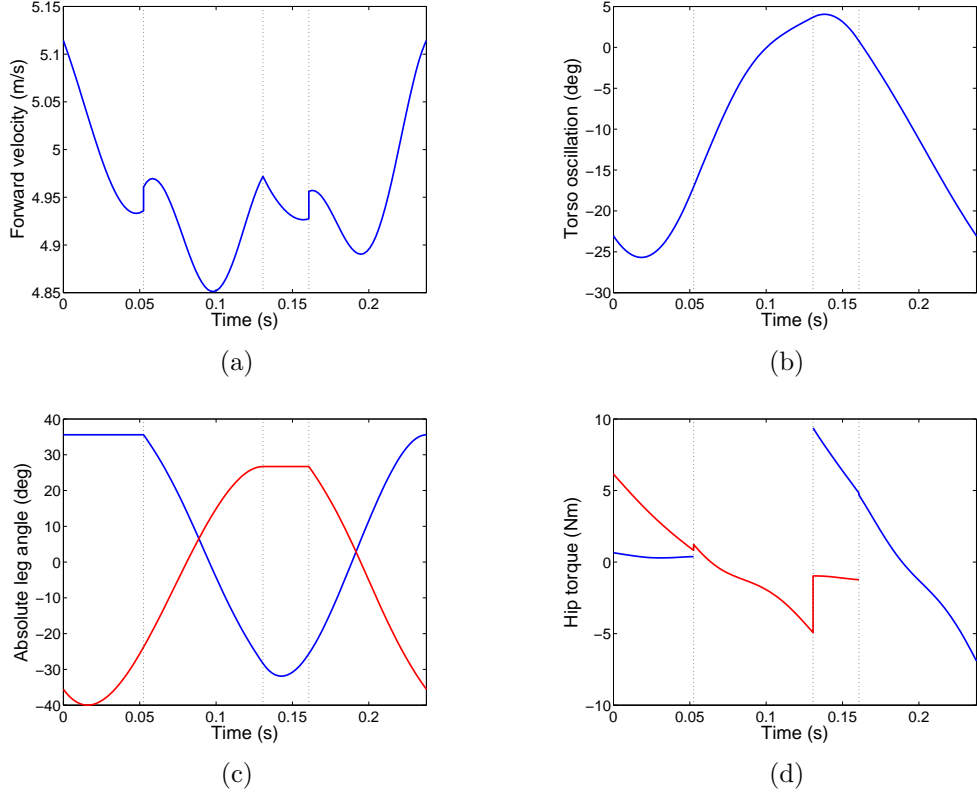


Figure 8.1: Evolution of forward velocity (a), torso oscillation (b), absolute leg angles (c) and hip joint torque (d) of a fixed point. In (c) and (d), the red and blue lines correspond to the anterior and posterior legs, respectively. The vertical lines separate one cycle into four phases: from left to right, fg, sp, fe and sa. The discontinuities are due to the impact at touchdown.

input to influence the coordination between the torso’s flexion-extension oscillations and the motion of the legs. In this chapter, a similar control approach is adopted in the higher-dimensional setting of the model of Fig. 7.1(b) to stabilize the bounding motions generated with the leg recirculation controller of Section 8.3.

In more detail, in each phase of the bounding cycle, the system (8.14) in closed loop with the corresponding action of the leg recirculation controller takes the form

$$\dot{x}_i = f_i^{\text{cl}}(x_i) + g_i^{\text{t}}(x_i)u_i^{\text{t}}, \quad (8.18)$$

where u_i^{t} represents the input torque acting in parallel with the torso spring; recall that u_i^{t} was not used in the controller of Section 8.3 that generates bounding motions.

Here, u_i^\dagger is employed in the stance phases to impose holonomic constraints on (8.18) that coordinate the motion of the torso and legs according to a nominal bounding orbit, as was generated in Section 8.3. Finally, a discrete-time controller is engaged to ensure local exponential stability of the resulting motions.

8.4.1 Continuous-time Control

For the stance phases $i \in \{\text{sp}, \text{sa}\}$ we associate to the continuous dynamics (8.18) the output function

$$y_i = (\theta_a - \theta_p) - h_i^{\text{d2}}(\varsigma_i(q_i), \eta_i) \quad (8.19)$$

where h_i^{d2} is the desired output of the relative pitch angle $\theta_a - \theta_p$. Through designing h_i^{d2} , the information about the leg-torso coordination pattern that characterizes the selected generated gait is passed to the feedback controller. In more detail, h_i^{d2} is designed through a suitable parameterization of the evolution of the relative pitch angle $\theta_a - \theta_p$ at the desired gait generated in Section 8.3, i.e.,

$$h_i^{\text{d2}}(\varsigma_i(q_i)) = \sum_{k=0}^3 c_{i,k}(\varsigma_i(q_i)) \eta_{i,k} \ , \quad (8.20)$$

where $\eta_{i,k}$ are the Beziér coefficients and the terms $c_{i,k}$ are given by

$$c_{i,k}(\varsigma_i) := \frac{3!}{k!(3-k)!} \varsigma_i^k (1 - \varsigma_i)^{3-k} \ , \quad (8.21)$$

in which ς_i is the strictly monotonic quantity defined as:

$$\varsigma_i := \frac{\gamma_j^{\text{max}} - \gamma_j}{\gamma_j^{\text{max}} - \gamma_j^{\text{min}}} \ . \quad (8.22)$$

where

$$j := \begin{cases} \text{a} & \text{for } i = \text{sa}, \\ \text{p} & \text{for } i = \text{sp}. \end{cases}$$

In (8.22), γ_a^{max} and γ_a^{min} are the maximum and minimum values of γ_a and similarly γ_p^{max} and γ_p^{min} are the corresponding values for γ_p . In words, the evolution of the relative

pitch angle during the stance phases is determined by the absolute leg angle of the unactuated leg in contact with the ground.

Finally, as in [142], the constraints (8.20) are imposed on the system in an asymptotic fashion via the control law

$$u_i^{\dagger} = (L_{g_i^{\dagger}} L_{f_i^{\text{cl}}} y_i)^{-1} [\nu(y_i, \dot{y}_i, \epsilon) - L_{f_i^{\text{cl}}}^2 y_i(x_i)] \quad (8.23)$$

where $\nu = -\frac{1}{\epsilon^2} K_P y_i - \frac{1}{\epsilon} K_V \dot{y}_i$. K_P, K_V are positive gains and $\epsilon > 0$.

8.4.2 Discrete-time Control

A discrete Linear Quadratic Regulator (LQR) is employed that positions the legs during flight based on feedback of the states at the Poincaré section. In more detail, denoting $\eta = \{\eta_{\text{sa}}, \eta_{\text{sp}}, \gamma_{\text{p}}^{\text{max}}, \gamma_{\text{a}}^{\text{max}}, \gamma_{\text{p}}^{\text{min}}, \gamma_{\text{a}}^{\text{min}}\}$, the Poincaré return map in closed loop with the continuous-time controller becomes

$$z[k+1] = \mathcal{P}_1(z[k], \alpha[k], \beta[k], \eta[k]) .$$

In what follows, the parameters α and η are kept constant and equal to their nominal values, while the touchdown angles $\beta[k]$ will be updated in a step-by-step fashion. To emphasize the fact that $\beta[k]$ includes inputs available for control in discrete time, we define

$$z[k+1] = \mathcal{P}_2(z[k], \beta[k]) . \quad (8.24)$$

Linearizing (8.24) at a fixed point \bar{z} results in

$$\Delta z[k+1] = A_2 \Delta z[k] + B_2 \Delta \beta[k] \quad (8.25)$$

where $\Delta z = z - \bar{z}$, $\Delta \beta = \beta - \bar{\beta}$, $A_2 = \frac{\partial \mathcal{P}_2}{\partial z} \Big|_{z=\bar{z}, \beta=\bar{\beta}}$ and $B_2 = \frac{\partial \mathcal{P}_2}{\partial \beta} \Big|_{z=\bar{z}, \beta=\bar{\beta}}$. Define a cost function

$$J(\Delta z) = \sum_{i=k}^{\infty} (\Delta z' Q \Delta z + \Delta \beta' R \Delta \beta), \quad (8.26)$$

where $Q = Q' \geq 0, R = R' > 0$. It can be shown that the optimal cost-to-go J^* is given by

$$J^*(\Delta z) = \Delta z' S \Delta z, \quad S' = S > 0 \quad (8.27)$$

where S is the solution of the associated discrete-time Riccati equation. The optimal feedback policy updates the swing-leg retraction angles according to

$$\Delta\beta[k] = -K\Delta z[k] \text{ .} \quad (8.28)$$

where K is derived from S as

$$K = (B_2'SB_2 + R)^{-1}(B_2'SA_2) \text{ ,}$$

and K and S are given by MATLAB's `d1qr`. With the controller (8.28), the closed-loop return map becomes

$$z[k+1] = \mathcal{P}_2(z[k], \bar{\beta} - K\Delta z[k]) := \mathcal{P}_3(z[k]) \text{ ,} \quad (8.29)$$

and all the eigenvalues of the Jacobian $\frac{\partial \mathcal{P}_3}{\partial z}$ are located within the unit disc. To illustrate the orbit's local stability, the state prior to liftoff of the bounding motion in Fig. 8.1 is perturbed away from the fixed point by an initial error of $+0.1\text{m/s}$ in \dot{x}_p and -3deg in θ_a . The system converges back to the nominal motion as shown in Fig. 8.2.

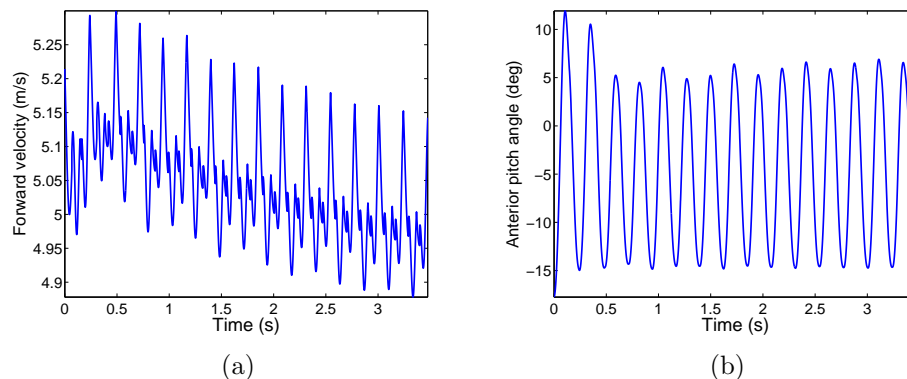


Figure 8.2: The evolution of the forward velocity and the anterior pitch angle when the system is perturbed with $+0.1\text{m/s}$ in \dot{x}_p and -3deg in θ_a .

8.5 Speed Transitions

In this section, speed transitions will be realized by switching between limit cycles according to the idea depicted in Fig. 6.1. In our speed transition setting, the

limit cycles ϕ_0 and ϕ_1 of Fig. 6.1 represent periodic bounding motions at different running speeds, the surfaces \mathcal{S}_0 and \mathcal{S}_1 denote the suitable Poincaré sections and \bar{z}_0 and \bar{z}_1 are the corresponding fixed points. The domain of attraction of each of the fixed points \bar{z}_0 and \bar{z}_1 on \mathcal{S}_0 and \mathcal{S}_1 is denoted¹ by \mathcal{D}_0 and \mathcal{D}_1 , respectively. By examining the relationship between the domains of attraction and the fixed points, the feasibility of generating a transition can be determined. For example, as shown in Fig. 6.1, if $\bar{z}_0 \in \mathcal{D}_1$, then employing the switching controller $\Gamma_{0 \rightarrow 1}$,

$$\Gamma_{0 \rightarrow 1}((\alpha_0, \beta_0, \eta_0, K_0) \rightarrow (\alpha_1, \beta_1, \eta_1, K_1)) \quad (8.30)$$

which effectively changes the controller parameters from those corresponding to the orbit ϕ_0 to those of ϕ_1 , resulting in the motion of the system being attracted by the target orbit ϕ_1 . The transition can be symbolically written as: if $\bar{z}_0 \in \mathcal{D}_1$, then $\bar{z}_0 \xrightarrow{\Gamma_{0 \rightarrow 1}} \bar{z}_1$. Furthermore, if $\bar{z}_1 \in \mathcal{D}_0$, then two-way transitions can be realized enabling both speed increasing and speed decreasing, denoted as $\bar{z}_0 \xleftrightarrow[\Gamma_{1 \rightarrow 0}]{\Gamma_{0 \rightarrow 1}} \bar{z}_1$.

8.5.1 Estimation of Domain of Attraction

To obtain estimates of the domain of attraction of the fixed points, we use the SOS method described in Chapter 6. First, the fixed point is translated to the origin:

$$\Delta z[k+1] = \mathcal{P}_4(\Delta z[k]) \quad (8.31)$$

where $\Delta z[k] = z[k] - \bar{z}$.

Then, by defining $V(\Delta z) := J^*(\Delta z)$, the problem of estimating the domain of attraction reduces to

$$\begin{aligned} & \max \rho \\ & \text{s.t. } \forall \Delta z \in \mathcal{D}(\rho), J_+^*(\Delta z[k]) < 0 \end{aligned} \quad (8.32)$$

where $J_+^*(\Delta z[k]) = J^*(\Delta z[k+1]) - J^*(\Delta z[k])$ and the domain \mathcal{D} is defined as

$$\mathcal{D}(\rho) := \{\Delta z \mid 0 \leq V(\Delta z) \leq \rho\} \quad (8.33)$$

¹ Note that \mathcal{D}_0 and \mathcal{D}_1 do not represent the domains of attraction of the entire periodic orbits ϕ_0 and ϕ_1 .

where ρ is a positive scalar. Using SOS programming, the following feasibility problem can be formulated

$$\begin{aligned} & \max \rho \\ & \text{s.t. } h(\Delta z) \text{ is SOS} \\ & -J_+^*(\Delta z[k]) - h(\Delta z[k])(\rho - J^*(\Delta z[k])) \text{ is SOS} \end{aligned} \quad (8.34)$$

where $h(\Delta z)$, a positive definite polynomial of Δz , is SOS. Given ρ^{\max} , the largest magnitude of tolerable single perturbation can be calculated for all the states:

$$\Delta z^{\max}(i) = \sqrt{\frac{\rho^{\max}}{S(i,i)}} \quad (8.35)$$

for $i = 1, 2, \dots, 10$, which provides an indication of the capability of the system in dealing with perturbations. We solved the SOS feasibility program (8.34) using SOSTOOLS and obtained Δz^{\max} for the fixed point in Fig. 8.2:

$$\Delta z^{\max} = (0.03, 0.03, 0.30, 0.04, 0.15, 0.13, 0.31, 0.37, 0.91, 0.90). \quad (8.36)$$

Figure 8.3 shows the ratio of these values to the values obtained from simulation for the representative fixed point. In the simulation method, a disturbance is regarded

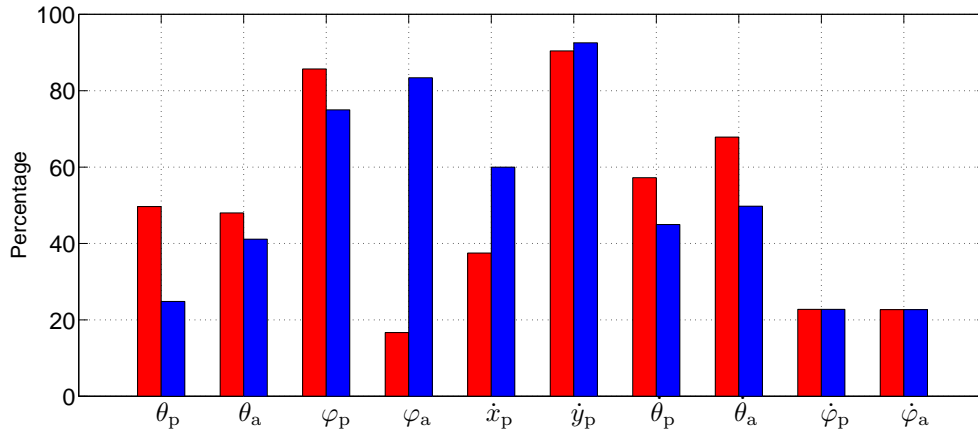


Figure 8.3: Ratio of the largest tolerable single perturbation predicted by the SOS method to their nominal values obtained through simulation for the presentative fixed point. The red and blue bars correspond to the positive and negative disturbances, respectively.

as tolerable if the error in the sates is less that 5% after 15 strides. It can be seen from Fig. 8.3 that the ratio is very diverse among different states. For instance, in the positive direction of φ_a , the SOS method can only capture less than 20% of the nominal value. On the other hand, in the negative direction of \dot{y}_p , more than 90% can be described by Δz^{\max} , meaning that ρ^{\max} is constrained by the capability of the system in dealing with negative disturbance in \dot{y}_p . This observation is consistent with the results in Chapter 4, implying that perturbations that tend to decrease hopping height may result in toe stubbing and failure to run due to the lack of active control over leg length.

8.5.2 Realization of Speed Transitions

If the estimate of the domain of attraction – which is determined through SOS programming as in Section 8.5.1 above – of a “target” fixed point is large enough to include the “source” fixed point, then transition between the two fixed points can be realized by simply switching the parameters of the corresponding controllers, from those of the “source” to those of the “target” motion. In this section, we illustrate the procedure in the context of transitioning between fixed points at different running speeds. As shown in Fig. 8.4, the fixed point \bar{z}_0 is computed and its domain of attraction \mathcal{D}_0 is estimated. Because the estimate of the domain of attraction lies in a high dimensional state space, Fig. 8.4 only shows its projection on the (\dot{x}_p, \dot{y}_p) plane. The fixed points \bar{z}_1 and \bar{z}_2 are both located within \mathcal{D}_0 , and have been computed by adding an inequality constraint when searching for them that characterizes their “distance” from \bar{z}_0 ; namely,

$$(\bar{z}_i - \bar{z}_0)' S_0 (\bar{z}_i - \bar{z}_0) \leq \rho_0^{\max} \quad (8.37)$$

or $i \in \{1, 2\}$. The forward running speed of \bar{z}_1 and \bar{z}_2 is 5.9m/s and 5.5m/s, respectively. After estimating the domains of attraction \mathcal{D}_1 and \mathcal{D}_2 of \bar{z}_1 and \bar{z}_2 respectively, transitions between the fixed points can be easily realized.

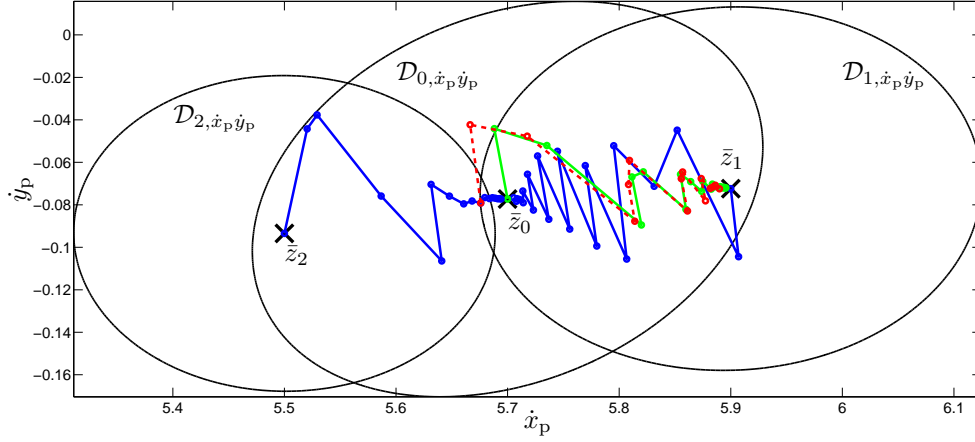


Figure 8.4: Transition between fixed points \bar{z}_0 , \bar{z}_1 and \bar{z}_2 of different running speeds. $\mathcal{D}_0, \mathcal{D}_1, \mathcal{D}_2$ are the projection of their estimated domain of attraction on the (\dot{x}_p, \dot{y}_p) planes when they are only perturbed in this plane. The blue line represents the transition from \bar{z}_1, \bar{z}_2 to \bar{z}_0 while the red line represents the transitions from \bar{z}_1 to \bar{z}_0 . The dotted red line represents a “shortcut” in transition from \bar{z}_2 to \bar{z}_1 .

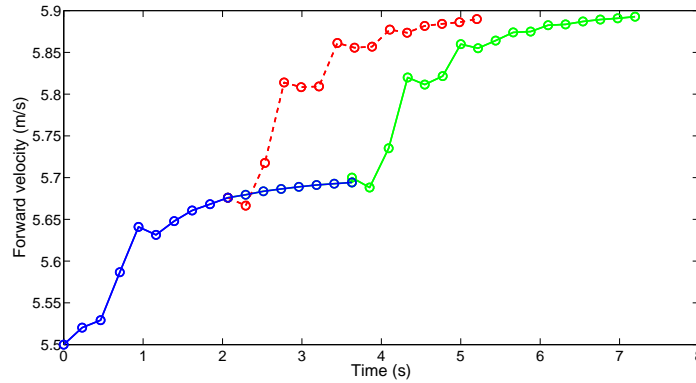


Figure 8.5: Two routes of transition from \bar{z}_2 to \bar{z}_1 in Fig. 8.4.

First, since $\bar{z}_1, \bar{z}_2 \in \mathcal{D}_0$, then the transitions $\bar{z}_1 \xrightarrow{\Gamma_{1 \rightarrow 0}} \bar{z}_0$ and $\bar{z}_2 \xrightarrow{\Gamma_{2 \rightarrow 0}} \bar{z}_0$ are both feasible; these transitions are represented by the blue solid lines in Fig. 8.4. Reversely, $\bar{z}_0 \xrightarrow{\Gamma_{0 \rightarrow 1}} \bar{z}_1$ can be realized, as the green solid line in Fig. 8.4 shows, while $\bar{z}_0 \xrightarrow{\Gamma_{0 \rightarrow 2}} \bar{z}_2$ is not possible since $\bar{z}_0 \notin \mathcal{D}_1$. To realize the transition from \bar{z}_0 to \bar{z}_2 , an intermediate fixed point can be computed that is closer to \bar{z}_0 so that its domain of attraction includes \bar{z}_0 .

By concatenating the basic transitions described above, multi-hop transitions

can be realized between fixed points that are further apart, provided that each transition is given sufficient time to be completed. For example, a transition from \bar{z}_2 to \bar{z}_1 can be achieved using \bar{z}_0 as a “bridge” (that is, $\bar{z}_2 \xrightarrow{\Gamma_{2 \rightarrow 0}} \bar{z}_0 \xrightarrow{\Gamma_{0 \rightarrow 1}} \bar{z}_1$) corresponding to an increase in the running speed from 5.5m/s to 5.9m/s. It should be mentioned that the duration of a transition can be decreased by tracking the “distance” to the “target” fixed point. For example, in switching from \bar{z}_2 to \bar{z}_1 , if the states enter the domain of attraction of \bar{z}_1 before converging to \bar{z}_0 , then the switching controller will adopt the controller information of \bar{z}_1 in advance, and the evolution of the states will follow the dotted red line without spending time to first converge to \bar{z}_0 . As shown in Fig. 8.4, this shortcut decreases the transition time by 28% from 7.2s to 5.2s. More generally, the transition dynamics can be modeled via a switching system and less conservative conditions on switching can be obtained as in [86]. Finally, we remark that, similar to the expansion of LQR-trees [132], the above procedure can be conducted iteratively such that more fixed points can be connected via their domain of attraction to cover a much larger range of running speeds, provided again that stability is respected by the switching system.

Chapter 9

CONCLUSIONS AND FUTURE WORK

9.1 Conclusions

A variety of conceptual models has been introduced to study legged locomotion. Such models offer unifying descriptions of task-level locomotion behaviors, and inform control design for legged robots. This thesis focused on models for quadrupedal running, with the objective to better understand the effect of torso compliance on gait stability and efficiency.

Along the philosophy of the SLIP, our analysis begins with a sagittal-plane quadrupedal model with a segmented flexible torso and compliant massless legs. Despite the sensitive dependence of the motion on the torso's bending oscillations, return map studies reveal that a large variety of cyclic bounding motions can be realized passively, through the natural interaction of the model with its environment. Furthermore, self-stable bounding motions emerge for certain combinations of the torso and leg relative stiffness. The implications of self-stable bounding orbits to control design are also discussed in the context of a hybrid control law that coordinates the torso bending oscillations with the movements of the legs. When the leg mass is considered negligible, a single actuator at the torso is enough to stabilize the four-degree-of-freedom system, rejecting significantly large disturbances without excessive effort. It turns out that the same principle of coordinating the torso bending movements with the leg hybrid oscillations is sufficient to stabilize bounding motions in a model with non-negligible leg mass. Utilizing the sums-of-squares programming, the domain of attraction of these bounding motions is estimated so that acceleration and deceleration can be realized by composing sequentially limit cycles that correspond to different running speeds in

a guaranteed fashion. This hybrid controller can also be extended to stabilize other running gaits, such as pronking and gait transitions can be realized when the domain of attraction of these gaits at the Poincaré section can be estimated.

Another aspect that was examined in this work was the relationship between elastic elements within the torso and the energy requirement for maintaining a gait. To do this, the basic model was extended to include non-trivial mass in the legs. By comparing the cost of transport with a rigid-torso model with the same leg mass, it is deduced that torso compliance significantly enhances energy efficiency, but *only* when the Froude number exceeds a particular value. Interestingly, this value corresponds to the Froude number at which transitions from trotting to galloping are observed in animals with drastically different morphological characteristics. Furthermore, by considering non-ideal torque generating and compliant elements with efficiencies corresponding to muscles and tendons, the flexible torso model was able to provide an accurate, *direct* prediction of the metabolic cost of transport of animals calculated using oxygen consumption.

9.2 Perspectives on Future Work

9.2.1 Experimental Validation

The most natural next step is to implement the hybrid controller developed in Chapter 5 on a quadrupedal robot with flexible-torso. The development of the robot is currently in progress and a leg prototype has been built and tested in hopping motion [75], see Fig. 9.1. To capture the dynamics associated with this leg, modeling studies need to be extended for segmented legs with switchable leg compliance and the controller also needs to be modified accordingly. The mechanical design of the flexible torso is another challenging task. The structure of the spine should be able to provide sufficient stiffness so that one complete oscillation of the torso can be finished in one stride. In addition, the actuation scheme at the torso should also be determined. Once the quadrupedal robot is available, parameter identification experiments need to be performed so that the physical parameters can be well measured. With these

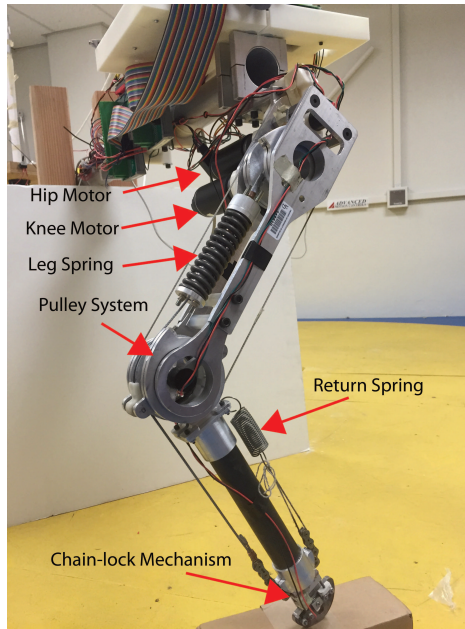


Figure 9.1: The manufactured leg [75]. A cable-pulley system is used to move the knee actuator more close to the hip axis. The engagement of the leg spring in the system dynamics is controlled by a chain-lock mechanism.

parameters, extensive testing of the controller in Chapter 5 needs to be performed in a more accurate simulation environment that considers actuator limitations and more realistic ground contact models. Finally, a transition controller needs to be developed to initialize bounding motion from static standing.

9.2.2 Extension of Modeling Work

Besides hardware validation, there is still work to be done in the modeling framework. First, more physical configurations of the quadrupedal model can be studied. The model in this work only considers the rotational degree of freedom at the torso joint. However, except from rotation, relative translation also exists between the segments of the torso, which allows the torso to contract and extend. Such a translation can be realized using a prismatic spring. Combining both degrees of freedom will result in a better understanding of the contribution of compliance to running performance and will provide a more accurate physiological description of the dorsoventral spinal oscillations observed in quadrupedal animal running.

Second, actuation in the torso has not been fully investigated based on the current models. When high speeds are desired—for example when hunting for prey or escaping from predators—torso actuation may facilitate the recirculation of the legs to cover larger distance during one stride, resulting in large energy consumption over a short period. It would therefore be interesting to compare various configurations of torso compliance and actuation, such as series-elastic actuation, parallel-elastic actuation, or switchable parallel-elastic actuation [75], in terms of energy efficiency and running performance.

Finally, this flexible-torso model can be extended to study more complex gaits, such as trotting and galloping in a reductive planar setting, by assuming all the legs move in the sagittal plane [89], see also Fig. 9.2. These gaits can be stabilized within the same control framework as introduced in Section 5, i.e., enforcing (virtual) holonomic constraints to coordinate the motion of the legs and the oscillation of the torso and update touchdown angles. In particular, to simplify the controller design of the galloping gait, especially the selection of the monotonic quantity, the gait can be roughly divided into four phases: gathered flight, when all the legs are in the air and the torso shows a concave configuration; extended flight, when all the legs are in the air and the torso shows a convex configuration; anterior stance, when one or two anterior legs are on the ground; and posterior stance, when one or two posterior legs are on the ground. Once stable trotting and galloping motions can be generated, they can be integrated

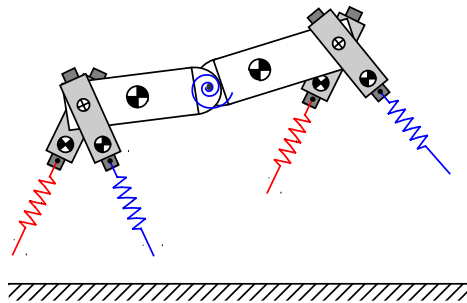


Figure 9.2: A pseudo three-dimensional model that can be used to study trotting and galloping gaits. Both the left (red) and right (blue) limbs will swing in the sagittal plane.

into the gait transition sequence to create more complex running behaviors.

In summary, there are many opportunities for future research in developing systematic methods for the design of feedback control laws that exploit compliant elements in the structure of legged robots to generate and sustain high-performance, naturally appealing dynamic running motions. This work should be considered as a step toward this direction for the case of quadrupedal robots.

BIBLIOGRAPHY

- [1] R. Alexander, *Elastic Mechanisms in Animal Movement*. Cambridge: Cambridge University Press, 1988.
- [2] —, “Optimization and gaits in the locomotion of vertebrates,” *Physiological Reviews*, vol. 69, no. 4, pp. 1199–1227, 1989.
- [3] —, “Models and the scaling of energy costs for locomotion,” *Journal of Experimental Biology*, vol. 208, no. 9, pp. 1645–1652, 2005.
- [4] R. Alexander, N. Dimery, and R. Ker, “Elastic structures in the back and their role in galloping in some mammals,” *Journal of Zoology*, vol. 207, no. 4, pp. 467–482, 1985.
- [5] R. Alexander, “Optimization and gaits in the locomotion of vertebrates,” *Physiological Reviews*, vol. 69, no. 4, pp. 1199–1227, 1989.
- [6] R. Alexander and A. Jayes, “A dynamic similarity hypothesis for the gaits of quadrupedal mammals,” *Journal of Zoology*, vol. 201, no. 1, pp. 135–152, 1983.
- [7] R. Altendorfer, D. E. Koditschek, and P. Holmes, “Stability analysis of legged locomotion models by symmetry-factored return maps,” *The International Journal of Robotics Research*, vol. 23, no. 10-11, pp. 979–999, 2004.
- [8] T. Amit, B. Gombert, J. Milgram, and R. Shahar, “Segmental inertial properties in dogs determined by magnetic resonance imaging,” *The Veterinary Journal*, vol. 182, no. 1, pp. 94–99, 2009.
- [9] A. Ananthanarayanan, M. Azadi, and S. Kim, “Towards a bio-inspired leg design for high-speed running,” *Bioinspiration & Biomimetics*, vol. 7, no. 4, p. 046005, 2012.
- [10] M. Ankarali and U. Saranlı, “Control of underactuated planar pronking through an embedded spring-mass hopper template,” *Autonomous Robots*, vol. 30, pp. 217–231, 2011.
- [11] S. Aoi, D. Katayama, S. Fujiki, N. Tomita, T. Funato, T. Yamashita, K. Senda, and K. Tsuchiya, “A stability-based mechanism for hysteresis in the walk–trot transition in quadruped locomotion,” *Journal of The Royal Society Interface*, vol. 10, no. 81, p. 20120908, 2013.

- [12] Ö. Arslan, U. Saranlı, and Ö. Morgul, “An approximate stance map of the spring mass hopper with gravity correction for nonsymmetric locomotions,” in *Proceedings of the IEEE/RSJ International Conference on Intelligent Robots and Systems*, 2009, pp. 2388–2393.
- [13] M. Berkemeier, “Modeling the Dynamics of Quadrupedal Running,” *The International Journal of Robotics Research*, vol. 17, no. 9, pp. 971–85, Sept. 1998.
- [14] A. A. Biewener and C. R. Taylor, “Bone strain: a determinant of gait and speed?” *Journal of Experimental Biology*, vol. 123, no. 1, pp. 383–400, 1986.
- [15] R. Blickhan, “The spring-mass model for running and hopping,” *Journal of Biomechanics*, vol. 22, no. 11-12, pp. 1217–1227, 1989.
- [16] R. Blickhan and R. J. Full, “Similarity in multi-legged locomotion: Bouncing like a monopode,” *Journal of Comparative Physiology A*, vol. 173, no. 5, pp. 509–517, 1993.
- [17] Boston Dynamics. (2012) CHEETAH - fastest legged robot. Mar. 15, 2013. [Online]. Available: <http://www.bostondynamics.com/>
- [18] H. Buchner, H. Savelberg, H. Schamhardt, and A. Barneveld, “Inertial properties of Dutch Warmblood horses,” *Journal of Biomechanics*, vol. 30, no. 6, pp. 653–658, 1997.
- [19] B. Buss, A. Ramezani, K. Hamed, B. Griffin, K. Galloway, and J. Grizzle, “Preliminary walking experiments with underactuated 3D bipedal robot MARLO,” in *Proceedings of the IEEE/RSJ International Conference on Intelligent Robots and Systems*, Sept 2014, pp. 2529–2536.
- [20] K. Byl, B. Satzinger, T. Strizic, P. Terry, and J. Pusey, “Toward agile control of a flexible-spine model for quadruped bounding,” in *SPIE Defense+ Security*. International Society for Optics and Photonics, 2015, pp. 94 680C–94 680C.
- [21] Q. Cao and I. Poulakakis, “Passive quadrupedal bounding with a segmented flexible torso,” in *Proceedings of the IEEE/RSJ International Conference on Intelligent Robots and Systems*, 2012, pp. 2484–2489.
- [22] —, “Passive stability and control of quadrupedal bounding with a flexible torso,” in *Proceedings of the IEEE/RSJ International Conference on Intelligent Robots and Systems*, 2013, pp. 6037–6043.
- [23] —, “On the energetics of quadrupedal bounding with and without torso compliance,” in *Proceedings of the IEEE/RSJ International Conference on Intelligent Robots and Systems*, 2014, pp. 4901–4906.

- [24] Q. Cao, A. T. van Rijn, and I. Poulakakis, “On the control of gait transitions in quadrupedal running,” in *Proceedings of the IEEE/RSJ International Conference on Intelligent Robots and Systems*, 2015, pp. 5136–5141.
- [25] Q. Cao and I. Poulakakis, “Quadrupedal bounding with a segmented flexible torso: passive stability and feedback control,” *Bioinspiration & Biomimetics*, vol. 8, no. 4, p. 046007, 2013.
- [26] —, “Control of quadrupedal bounding with flexible torso and speed transition with sums of squares verification,” in *The 1st International Symposium on Swarm Behaviour and Bio-inspired Robotics*, 2015.
- [27] —, “On the energetics of quadrupedal running: predicting the metabolic cost of transport via a flexible-torso model,” *Bioinspiration & Biomimetics*, vol. 10, no. 5, p. 056008, 2015.
- [28] P. Chatzakos and E. Papadopoulos, “Self-stabilizing quadrupedal running by mechanical design,” *Applied Bionics and Biomechanics*, vol. 6, no. 1, pp. 73–85, 2009.
- [29] G. Chesi, “Estimating the domain of attraction via union of continuous families of Lyapunov estimates,” *Systems & Control letters*, vol. 56, no. 4, pp. 326–333, 2007.
- [30] —, *Domain of attraction: analysis and control via SOS programming*. London: Springer Science & Business Media, 2011.
- [31] H.-D. Chiang, M. W. Hirsch, and F. F. Wu, “Stability regions of nonlinear autonomous dynamical systems,” *IEEE Transactions on Automatic Control*, vol. 33, no. 1, pp. 16–27, 1988.
- [32] S. H. Collins, A. Ruina, R. Tedrake, and M. Wisse, “Efficient bipedal robots based on passive-dynamic walkers,” *Science*, vol. 307, no. 5712, pp. 1082–1085, 2005.
- [33] S. H. Collins, M. Wisse, and A. Ruina, “A three-dimensional passive-dynamic walking robot with two legs and knees,” *The International Journal of Robotics Research*, vol. 20, no. 7, pp. 607–15, July 2001.
- [34] U. Culha and U. Saranlı, “Quadrupedal bounding with an actuated spinal joint,” in *Proceedings of the IEEE International Conference on Robotics and Automation*, 2011, pp. 1392–1397.
- [35] Q. Deng, S. Wang, W. Xu, J. Mo, and Q. Liang, “Quasi passive bounding of a quadruped model with articulated spine,” *Mechanism and Machine Theory*, vol. 52, pp. 232–242, 2012.

- [36] M. Dickinson, C. Farley, R. Full, M. Koehel, R. Kram, and S. Lehman, “How animals move: An integrative view,” *Science*, vol. 288, pp. 100–106, 2000.
- [37] M. D. Eaton, D. L. Evans, D. R. Hodgson, and R. J. Rose, “Effect of treadmill incline and speed on metabolic rate during exercise in thoroughbred horses,” *Journal of Applied Physiology*, vol. 79, no. 3, pp. 951–957, 1995.
- [38] J. Estremera and K. Waldron, “Thrust control, stabilization and energetics of a quadruped running robots,” *The International Journal of Robotics Research*, vol. 27, no. 10, p. 1135, 2008.
- [39] C. T. Farley, J. Glasheen, and T. A. McMahon, “Running springs: speed and animal size,” *Journal of Experimental Biology*, vol. 185, no. 1, pp. 71–86, 1993.
- [40] C. T. Farley and C. R. Taylor, “A mechanical trigger for the trot-gallop transition in horses,” *Science*, vol. 253, no. 5017, pp. 306–308, 1991.
- [41] Y. Fukuoka, H. Kimura, and A. H. Cohen, “Adaptive dynamic walking of a quadruped robot on irregular terrain based on biological concepts,” *The International Journal of Robotics Research*, vol. 23, no. 10-11, pp. 1059–1073, 2004.
- [42] R. Full and D. E. Koditschek, “Templates and anchors: Neuromechanical hypotheses of legged locomotion on land,” *Journal of Experimental Biology*, vol. 202, pp. 3325–3332, 1999.
- [43] G. Gabrielli and T. von Karman, “What price speed? specific power required for propulsion of vehicles,” *Mechanical Engineering*, vol. 72, no. 10, pp. 775–781, 1950.
- [44] P. P. Gambaryan, *How Mammals Run: Anatomical Adaptations*. New York: Wiley, 1974.
- [45] Z. Gan and C. Remy, “A passive dynamic quadruped that moves in a large variety of gaits,” in *Proceedings of the IEEE/RSJ International Conference on Intelligent Robots and Systems*, Sept. 2014, pp. 4876–4881.
- [46] H. Geyer, A. Seyfarth, and R. Blickhan, “Spring-mass running: Simple approximate solution and application to gait stability,” *Journal of Theoretical Biology*, vol. 232, pp. 315–328, 2005.
- [47] R. M. Ghigliazza, R. Altendorfer, P. Holmes, and D. E. Koditschek, “A simply stabilized running model,” *SIAM Review*, vol. 47, no. 3, pp. 519–549, 2005.
- [48] J. W. Grizzle, G. Abba, and F. Plestan, “Asymptotically Stable Walking for Biped Robots: Analysis via Systems with Impulse Effects,” *IEEE Transactions on Automatic Control*, vol. 46, no. 1, pp. 51–64, 2001.

- [49] J. Guckenheimer and P. Holmes, *Nonlinear Oscillations, Dynamical Systems, and Bifurcations of Vector Fields*, ser. Applied Mathematical Sciences. New York: Springer-Verlag, 1996, vol. 42.
- [50] M. Haberland, J. G. D. Karssen, S. Kim, and M. Wisse, “The effect of swing leg retraction on running energy efficiency,” in *Proceedings of the IEEE/RSJ International Conference of Intelligent Robots and Systems*, 2011, pp. 3957–3962.
- [51] R. Hackert, N. Schilling, and M. S. Fischer, “Mechanical self-stabilization, a working hypothesis for the study of the evolution of body proportions in terrestrial mammals?” *Comptes Rendus Palevol*, vol. 5, no. 34, pp. 541–549, 2006.
- [52] B. M. Haueisen, “Investigation of an Articulated Spine in a Quadruped Robotic System,” Ph.D. dissertation, The University of Michigan, 2011.
- [53] G. C. Haynes, J. Pusey, R. Knopf, A. M. Johnson, and D. E. Koditschek, “Laboratory on legs: An architecture for adjustable morphology with legged robots,” in *Proceedings of the SPIE Defense, Security, and Sensing Conference, Unmanned Systems Technology XIV (8387)*, 2012.
- [54] N. C. Heglund and C. R. Taylor, “Speed, stride frequency and energy cost per stride: how do they change with body size and gait?” *Journal of Experimental Biology*, vol. 138, no. 1, pp. 301–318, 1988.
- [55] D. Henrion, D. Peaucelle, D. Arzelier, and M. Sebek, “Ellipsoidal approximation of the stability domain of a polynomial,” *IEEE Transactions on Automatic Control*, vol. 48, no. 12, pp. 2255–2259, 2003.
- [56] H. M. Herr and T. A. McMahon, “A galloping horse model,” *The International Journal of Robotics Research*, vol. 20, no. 1, pp. 26–37, 2001.
- [57] H. M. Herr, G. T. Huang, and T. A. McMahon, “A model of scale effects in mammalian quadrupedal running,” *Journal of Experimental Biology*, vol. 205, no. 7, pp. 959–967, 2002.
- [58] M. Hildebrand, “Motions of the running cheetah and horse,” *Journal of Mammalogy*, vol. 40, no. 4, pp. 481–495, 1959.
- [59] —, “Further studies on locomotion of the cheetah,” *Journal of Mammalogy*, vol. 42, no. 1, pp. 84–91, 1961.
- [60] —, “The quadrupedal gaits of vertebrates,” *BioScience*, vol. 39, no. 11, p. 766, 1989.
- [61] P. Holmes, R. J. Full, D. E. Koditschek, and J. Guckenheimer, “The dynamics of legged locomotion: models, analyses, and challenges,” *SIAM Review*, vol. 48, no. 2, pp. 207–304, 2006.

- [62] D. F. Hoyt and C. R. Taylor, “Gait and the energetics of locomotion in horses,” *Nature*, vol. 292, pp. 239 – 240, 1981.
- [63] M. Hutter, H. Sommer, C. Gehring, M. Hoepflinger, M. Bloesch, and R. Siegwart, “Quadrupedal locomotion using hierarchical operational space control,” *The International Journal of Robotics Research*, vol. 33, no. 8, pp. 1047–1062, 2014.
- [64] A. J. Ijspeert, “Central pattern generators for locomotion control in animals and robots: a review,” *Neural Networks*, vol. 21, no. 4, pp. 642–653, 2008.
- [65] A. Isidori, *Nonlinear Control Systems*, 3rd ed. Berlin: Springer-Verlag, 1995.
- [66] Z. Jarvis-Wloszek, R. Feeley, W. Tan, K. Sun, and A. Packard, “Some controls applications of sum of squares programming,” in *IEEE Conference on Decision and Control*, vol. 5, 2003, pp. 4676–4681.
- [67] J. Karssen and M. Wisse, “Running with improved disturbance rejection by using non-linear springs,” *The International Journal of Robotics Research*, vol. 30, no. 13, pp. 1585–1595, 2011.
- [68] H. K. Khalil, *Nonlinear Systems*, 3rd ed. Upper Saddle River, NJ: Prentice Hall, 2002.
- [69] L. Khodadadi, B. Samadi, and H. Khaloozadeh, “Estimation of region of attraction for polynomial nonlinear systems: A numerical method,” *ISA transactions*, vol. 53, no. 1, pp. 25–32, 2014.
- [70] M. Khoramshahi, A. Sprowitz, A. Tuleu, M. Ahmadabadi, and A. Ijspeert, “Benefits of an active spine supported bounding locomotion with a small compliant quadruped robot,” in *Proceedings of the IEEE International Conference on Robotics and Automation*, 2013, pp. 3329–3334.
- [71] S. Kim. (2013) Cheetah-inspired quadruped. Mar. 15, 2013. [Online]. Available: <http://biomimetics.mit.edu:8100/wordpress/>
- [72] R. Kram and C. R. Taylor, “Energetics of running: a new perspective,” *Nature*, vol. 346, no. 6281, pp. 265–267, 1990.
- [73] D. P. Krasny and D. E. Orin, “Generating high-speed dynamic running gaits in a quadruped robot using an evolutionary search,” *IEEE Transactions on Systems, Man, and Cybernetics, Part B: Cybernetics*, vol. 34, no. 4, pp. 1685–1696, 2004.
- [74] K. F. Leeser, “Locomotion experiments on a planar quadruped robot with articulated spine,” Master’s thesis, Massachusetts Institute of Technology, February 1996.

- [75] X. Liu, A. Rossi, and I. Poulakakis, “SPEAR: A monopedal robot with switchable parallel elastic actuator,” in *Proceedings of the IEEE/RSJ International Conference on Intelligent Robots and Systems*, Hamburg, Germany, Sept. 2015, pp. 5142–5147.
- [76] J. Löfberg, “YALMIP: A toolbox for modeling and optimization in MATLAB,” in *IEEE International Symposium on Computer Aided Control Systems Design*, 2004, pp. 284–289.
- [77] L. D. Maes, M. Herbin, R. Hackert, V. L. Bels, and A. Abourachid, “Steady locomotion in dogs: temporal and associated spatial coordination patterns and the effect of speed,” *Journal of Experimental Biology*, vol. 211, no. 1, pp. 138–149, 2008.
- [78] A. Majumdar, A. Ahmadi, and R. Tedrake, “Control and verification of high-dimensional systems with DSOS and SDSOS programming,” in *Proceedings of IEEE Conference on Decision and Control*, 2014, pp. 394–401.
- [79] I. R. Manchester, M. M. Tobenkin, M. Levashov, and R. Tedrake, “Regions of attraction for hybrid limit cycles of walking robots,” *arXiv:1010.2247*, 2010.
- [80] R. Margaria, *Biomechanics and Energetics of Muscular Exercise*. Oxford: Clarendon Press, 1976.
- [81] T. McGeer, “Passive dynamic walking,” *The International Journal of Robotics Research*, vol. 9, no. 2, pp. 62–82, 1990.
- [82] T. A. McMahon and G. C. Cheng, “The mechanics of running: How does stiffness couple with speed?” *Journal of Biomechanics*, vol. 23, pp. 65–78, 1990, suppl. 1.
- [83] B. Miller, J. Schmitt, and J. Clark, “Quantifying disturbance rejection of SLIP-like running systems,” *The International Journal of Robotics Research*, vol. 31, no. 5, pp. 573–587, 2012.
- [84] A. Minetti, L. Ardigo, E. Reinach, and F. Saibene, “The relationship between mechanical work and energy expenditure of locomotion in horses,” *Journal of Experimental Biology*, vol. 202, no. 17, pp. 2329–2338, 1999.
- [85] J. Moore, R. Cory, and R. Tedrake, “Robust post-stall perching with a simple fixed-wing glider using LQR-trees,” *Bioinspiration & Biomimetics*, vol. 9, no. 2, p. 025013, 2014.
- [86] M. S. Motahar, S. Veer, and I. Poulakakis, “Stable navigation of 3D limit cycle bipedal walkers,” in *IEEE Conference on Decision and Control*, 2016, submitted.
- [87] K. N. Murphy, “Trotting and bounding in a simple planar model,” Carnegie Mellon University, The Robotics Institute, Tech. Rep., 1985.

- [88] K. N. Murphy and M. H. Raibert, “Trotting and bounding in a planar two-legged models,” in *5th Symposium on Theory and Practice of Robots and Manipulators*, K. K. A. Morecki, G. Bianchi, Ed. MA: MIT Press, 1985, pp. 411–420.
- [89] P. Nanua and K. Waldron, “Energy comparison between trot, bound and gallop using a simple model,” *Journal of Biomechanical Engineering*, vol. 117, no. 4, pp. 466–473, 1995.
- [90] P. Nanua, “Dynamics of a Galloping Quadruped,” Ph.D. dissertation, Ohio State University, 1992.
- [91] H. W. Park, S. Park, and S. Kim, “Variable-speed quadrupedal bounding using impulse planning: Untethered high-speed 3D running of MIT Cheetah 2,” in *Proceedings of the IEEE International Conference on Robotics and Automation*, May 2015, pp. 5163–5170.
- [92] H.-W. Park and S. Kim, “Quadrupedal galloping control for a wide range of speed via vertical impulse scaling,” *Bioinspiration & Biomimetics*, vol. 10, no. 2, p. 025003, 2015.
- [93] H.-W. Park, A. Ramezani, and J. Grizzle, “A finite-state machine for accommodating unexpected large ground-height variations in bipedal robot walking,” *IEEE Transactions on Robotics*, vol. 29, no. 2, pp. 331–345, April 2013.
- [94] H.-W. Park, P. Wensing, and S. Kim, “Online planning for autonomous running jumps over obstacles in high-speed quadrupeds,” in *Proceedings of Robotics: Science and Systems*, 2015.
- [95] P. A. Parrilo, “Structured semidefinite programs and semialgebraic geometry methods in robustness and optimization,” Ph.D. dissertation, California Institute of Technology, 2000.
- [96] C. M. Pollock and R. E. Shadwick, “Relationship between body mass and biomechanical properties of limb tendons in adult mammals,” *American Journal of Physiology*, vol. 266, no. 3, pp. 1016–1021, 1994.
- [97] I. Poulakakis, “Stabilizing Monopedal Robot Running: Reduction-by-Feedback and Compliant Hybrid Zero Dynamics,” Ph.D. dissertation, Department of Electrical Engineering and Computer Science, University of Michigan, December 2008.
- [98] I. Poulakakis, E. Papadopoulos, and M. Buehler, “On the stable passive dynamics of quadrupedal running,” in *Proceedings of the IEEE International Conference on Robotics and Automation*, vol. 1, 2003, pp. 1368–1373.

- [99] I. Poulakakis, E. G. Papadopoulos, and M. Buehler, “On the stability of the passive dynamics of quadrupedal running with a bounding gait,” *The International Journal of Robotics Research*, vol. 25, no. 7, pp. 669–687, 2006.
- [100] I. Poulakakis, J. Smith, and M. Buehler, “Modeling and experiments of untethered quadrupedal running with a bounding gait: The Scout II robots,” *The International Journal of Robotics Research*, vol. 24, no. 4, pp. 239–256, 2005.
- [101] I. Poulakakis, J. A. Smith, and M. Buehler, “On the dynamics of bounding and extensions: Towards the half-bound and gallop gaits,” in *Adaptive Motion of Animals and Machines*. Springer, 2006, pp. 79–88.
- [102] S. Prajna, A. Papachristodoulou, P. Parrilo, *et al.*, “Introducing SOSTOOLS: A general purpose sum of squares programming solver,” in *Proceedings of IEEE Conference on Decision and Control*, vol. 1, 2002, pp. 741–746.
- [103] S. Prajna, A. Papachristodoulou, and P. A. Parrilo, “SOSTOOLS: sum of squares optimization toolbox for MATLAB—users guide,” *Control and Dynamical Systems, California Institute of Technology, Pasadena, CA*, 2004.
- [104] M. H. Raibert, *Legged Robots that Balance*. Cambridge, MA: MIT Press, 1986.
- [105] ———, “Trotting, pacing and bounding by a quadruped robots,” *Journal of Biomechanics*, vol. 23, pp. 79–98, 1990, suppl. 1.
- [106] M. H. Raibert, M. Chepponis, and J. Brown, H., “Running on four legs as though they were one,” *IEEE Transactions on Robotics and Automation*, vol. 2, no. 2, pp. 70–82, 1986.
- [107] M. Raibert, K. Blankespoor, G. Nelson, R. Playter, and the BigDog Team, “BigDog, the rough-terrain quadruped robot,” in *Proceedings of the 17th IFAC World Congress*, 2008, pp. 10 822–10 825.
- [108] C. D. Remy, K. Buffinton, and R. Siegwart, “Stability analysis of passive dynamic walking of quadrupeds,” *The International Journal of Robotics Research*, vol. 29, no. 9, pp. 1173–1185, 2010.
- [109] C. D. Remy, K. Buffinton, and R. Y. Siegwart, “Energetics of passivity based running with high-compliance series elastic actuation,” in *Proceedings of Mechatronics Forum Biennial International Conference*, 2010.
- [110] J. Rummel and A. Seyfarth, “Stable running with segmented legs,” *The International Journal of Robotics Research*, vol. 27, no. 8, pp. 919–934, 2008.
- [111] C. P. Santos and V. Matos, “Gait transition and modulation in a quadruped robot: A brainstem-like modulation approach,” *Robotics and Autonomous Systems*, vol. 59, no. 9, pp. 620–634, 2011.

- [112] U. Saranli and D. E. Koditschek, “Template based control of hexapedal running,” in *Proceedings of the IEEE International Conference on Robotics and Automation*, vol. 1, 2003, pp. 1374–1379.
- [113] U. Saranli, W. Schwind, and D. E. Koditschek, “Toward the control of a multi-jointed, monopod runner,” in *Proceedings of the IEEE International Conference on Robotics and Automation*, 1998, pp. 2676–2682.
- [114] N. Schilling and R. Hackert, “Sagittal spine movements of small therian mammals during asymmetrical gaits,” *Journal of Experimental Biology*, vol. 209, pp. 3925–3939, 2006.
- [115] J. P. Schmiedeler and L. Funke, “Unfinished business: Impulsive models of quadrupedal running gaits,” in *Advances in Mechanisms, Robotics and Design Education and Research*. Springer, 2013, pp. 295–304.
- [116] J. P. Schmiedeler, R. Siston, and K. J. Waldron, “The significance of leg mass in modeling quadrupedal running gaits,” in *ROMANSY 14: Theory and Practice of Robots and Manipulators*, G. Bianchi, J. C. Guinot, and C. Rzymkowski, Eds. Vienna: Springer, 2002, pp. 481–488.
- [117] A. Schwab and M. Wisse, “Basin of attraction of the simplest walking model,” in *Proceedings of the ASME Design Engineering Technical Conference*, vol. 6, 2001, pp. 531–539.
- [118] W. J. Schwind, “Spring Loaded Inverted Pendulum Running: A Plant Model,” Ph.D. dissertation, University of Michigan, 1998.
- [119] J. E. Seipel, “Analytic-holistic two-segment model of quadruped back-bending in the sagittal plane,” in *Proceedings of ASME Mechanisms and Robotics Conference*, vol. 6, 2011, pp. 855–861.
- [120] C. Semini, N. G. Tsagarakis, E. Guglielmino, M. Focchi, F. Cannella, and D. G. Caldwell, “Design of HyQ - a hydraulically and electrically actuated quadruped robot,” *Proceedings of the IMechE Part I: Journal Systems and Control Engineering*, vol. 225, no. 6, pp. 831–849, 2011.
- [121] C. Semini, V. Barasuol, T. Boaventura, M. Frigerio, M. Focchi, D. G. Caldwell, and J. Buchli, “Towards versatile legged robots through active impedance control,” *The International Journal of Robotics Research*, vol. 34, no. 7, pp. 1003–1020, 2015.
- [122] S. Seok, A. Wang, M. Y. Chuah, D. Otten, J. Lang, and S. Kim, “Design principles for highly efficient quadrupeds and implementation on the MIT Cheetah robots,” in *Proceedings of IEEE International Conference on Robotics and Automation*, 2013, pp. 3307–3312.

- [123] A. Seyfarth, H. Geyer, M. Gunther, and R. Blickhan, “A movement criterion for running,” *Journal of Biomechanics*, vol. 35, no. 5, pp. 649–55, 2002.
- [124] A. Seyfarth, H. Geyer, and H. Herr, “Swing leg retraction: A simple control model for stable running,” *Journal of Experimental Biology*, vol. 206, pp. 2547–2555, 2003.
- [125] Z. Shen and J. Seipel, “Animals prefer leg stiffness values that may reduce the energetic cost of locomotion,” *Journal of Theoretical Biology*, vol. 364, pp. 433–438, 2015.
- [126] ———, “The leg stiffnesses animals use may improve the stability of locomotion,” *Journal of theoretical biology*, vol. 377, pp. 66–74, 2015.
- [127] A. Smith and M. Berkemeier, “Passive dynamic quadrupedal walking,” in *Proceedings of the IEEE International Conference on Robotics and Automation*, vol. 1, Apr. 1997, pp. 34–39.
- [128] M. W. Spong, S. Hutchinson, and M. Vidyasagar, *Robot Modeling and Control*. New York: Wiley, 2005.
- [129] A. Spröwitz, A. Tuleu, M. Vespignani, M. Ajallooeian, E. Badri, and A. J. Ijspeert, “Towards dynamic trot gait locomotion: Design, control, and experiments with cheetah-cub, a compliant quadruped robot,” *The International Journal of Robotics Research*, vol. 32, no. 8, pp. 932–950, 2013.
- [130] K. Sreenath, H.-W. Park, I. Poulakakis, and Grizzle, “Embedding active force control within the compliant hybrid zero dynamics to achieve stable, fast running on MABEL,” *The International Journal of Robotics Research*, vol. 32, no. 3, pp. 324–345, 2012.
- [131] C. R. Taylor, A. Shkolnik, R. Dmiel, D. Baharav, and A. Borut, “Running in cheetahs, gazelles, and goats: energy cost and limb configuration,” *American Journal of Physiology*, vol. 227, no. 4, pp. 848–850, 1974.
- [132] R. Tedrake, I. R. Manchester, M. Tobenkin, and J. W. Roberts, “LQR-trees: Feedback motion planning via sums-of-squares verification,” *The International Journal of Robotics Research*, vol. 29, no. 8, pp. 1038–1052, 2010.
- [133] U. Topcu, A. Packard, and P. Seiler, “Local stability analysis using simulations and sum-of-squares programming,” *Automatica*, vol. 44, no. 10, pp. 2669–2675, 2008.
- [134] K. Tsujita, T. Kobayashi, T. Inoura, and T. Masuda, “Gait transition by tuning muscle tones using pneumatic actuators in quadruped locomotion,” in *Proceedings of the IEEE/RSJ International Conference on Intelligent Robots and Systems*, 2008, pp. 2453–2458.

- [135] K. Tsujita, K. Tsuchiya, and A. Onat, “Adaptive gait pattern control of a quadruped locomotion robot,” in *Proceedings of the IEEE/RSJ International Conference on Intelligent Robots and Systems*, vol. 4, 2001, pp. 2318–2325.
- [136] V. A. Tucker, “The energetic cost of moving about,” *American Scientist*, vol. 63, no. 4, pp. 413–419, 1975.
- [137] A. K. Valenzuela and S. Kim, “Optimally scaled hip-force planning: A control approach for quadrupedal running,” in *Proceedings of the IEEE International Conference on Robotics and Automation*, 2012, pp. 1901–1907.
- [138] A. Vannelli and M. Vidyasagar, “Maximal lyapunov functions and domains of attraction for autonomous nonlinear systems,” *Automatica*, vol. 21, no. 1, pp. 69–80, 1985.
- [139] H. Vejdani, Y. Blum, M. Daley, and J. Hurst, “Bio-inspired swing leg control for spring-mass robots running on ground with unexpected height disturbance,” *Bioinspiration & Biomimetics*, vol. 8, no. 4, p. 046006, 2013.
- [140] R. M. Walter and D. R. Carrier, “Ground forces applied by galloping dogs,” *Journal of Experimental Biology*, vol. 210, no. 2, pp. 208–216, 2007.
- [141] X. Wang, M. Li, P. Wang, and L. Sun, “Running and turning control of a quadruped robot with compliant legs in bounding gait,” in *Proceedings of the IEEE International Conference on Robotics and Automation*, 2011, pp. 511–518.
- [142] E. R. Westervelt, J. W. Grizzle, C. Chevallereau, J. H. Choi, and B. Morris, *Feedback Control of Dynamic Bipedal Robot Locomotion*. Taylor & Francis/CRC Press, 2007.
- [143] E. R. Westervelt, B. Morris, and K. D. Farrell, “Analysis results and tools for the control of planar bipedal gaits using hybrid zero dynamics,” *Autonomous Robots*, vol. 23, no. 2, pp. 131–145, 2007.
- [144] E. R. Westervelt, J. W. Grizzle, and D. E. Koditschek, “Hybrid zero dynamics of planar biped walkers,” *IEEE Transactions on Automatic Control*, vol. 48, no. 1, pp. 42–56, 2003.
- [145] R. Yamasaki, Y. Ambe, S. Aoi, and F. Matsuno, “Quadrupedal bounding with spring-damper body joint,” in *Proceedings of the IEEE/RSJ International Conference on Intelligent Robots and Systems*, 2013, pp. 2345–2350.
- [146] Z. G. Zhang, Y. Fukuoka, and H. Kimura, “Stable quadrupedal running based on a spring-loaded two-segment legged models,” in *Proceedings of the IEEE International Conference on Robotics and Automation*, vol. 3, 2005, pp. 2601–2606.

- [147] Z. G. Zhang, H. Kimura, and Y. Fukuoka, “Autonomously generating efficient running of a quadruped robot using delayed feedback control,” *Advanced Robotics*, vol. 20, no. 6, pp. 607–629, 2006.

Appendix

REPRINT PERMISSIONS

This dissertation includes results published by the author in conference proceedings [21, 22, 23, 26] and journals [25, 27]. The reuse of material from [25, 27] in this present dissertation is permitted under the Creative Commons Attribution 3.0 (CC BY 3.0) license. Reprint permissions to reuse material from [21, 22, 23, 26] have been granted by the publisher and are attached in the following pages.



[Creative Commons](#)

Creative Commons License Deed

Attribution 3.0 Unported (CC BY 3.0)

This is a human-readable summary of (and not a substitute for) the [license](#).
[Disclaimer](#)



You are free to:



Share — copy and redistribute the material in any medium or format



Adapt — remix, transform, and build upon the material
for any purpose, even commercially.

The licensor cannot revoke these freedoms as long as you follow the license terms.

Under the following terms:



Attribution — You must give [appropriate credit](#), provide a link to the license, and [indicate if changes were made](#). You may do so in any reasonable manner, but not in any way that suggests the licensor endorses you or your use.

No additional restrictions — You may not apply legal terms or [technological measures](#) that legally restrict others from doing anything the license permits.

Notices:

You do not have to comply with the license for elements of the material in the public domain or where your use is permitted by an applicable [exception or limitation](#).

No warranties are given. The license may not give you all of the permissions necessary for your intended use. For example, other rights such as [publicity, privacy, or moral rights](#) may limit how you use the material.



RightsLink®

[Home](#)
[Create Account](#)
[Help](#)


Title: Passive quadrupedal bounding with a segmented flexible torso

Conference Proceedings: Intelligent Robots and Systems (IROS), 2012 IEEE/RSJ International Conference on

Author: Q. Cao; I. Poulakakis

Publisher: IEEE

Date: 7-12 Oct. 2012

Copyright © 2012, IEEE

[LOGIN](#)

If you're a **copyright.com user**, you can login to RightsLink using your copyright.com credentials. Already a **RightsLink user** or want to [learn more?](#)

Thesis / Dissertation Reuse

The IEEE does not require individuals working on a thesis to obtain a formal reuse license, however, you may print out this statement to be used as a permission grant:

Requirements to be followed when using any portion (e.g., figure, graph, table, or textual material) of an IEEE copyrighted paper in a thesis:

- 1) In the case of textual material (e.g., using short quotes or referring to the work within these papers) users must give full credit to the original source (author, paper, publication) followed by the IEEE copyright line © 2011 IEEE.
- 2) In the case of illustrations or tabular material, we require that the copyright line © [Year of original publication] IEEE appear prominently with each reprinted figure and/or table.
- 3) If a substantial portion of the original paper is to be used, and if you are not the senior author, also obtain the senior author's approval.

Requirements to be followed when using an entire IEEE copyrighted paper in a thesis:

- 1) The following IEEE copyright/ credit notice should be placed prominently in the references: © [year of original publication] IEEE. Reprinted, with permission, from [author names, paper title, IEEE publication title, and month/year of publication]
- 2) Only the accepted version of an IEEE copyrighted paper can be used when posting the paper or your thesis on-line.
- 3) In placing the thesis on the author's university website, please display the following message in a prominent place on the website: In reference to IEEE copyrighted material which is used with permission in this thesis, the IEEE does not endorse any of [university/educational entity's name goes here]'s products or services. Internal or personal use of this material is permitted. If interested in reprinting/republishing IEEE copyrighted material for advertising or promotional purposes or for creating new collective works for resale or redistribution, please go to http://www.ieee.org/publications_standards/publications/rights/rights_link.html to learn how to obtain a License from RightsLink.

If applicable, University Microfilms and/or ProQuest Library, or the Archives of Canada may supply single copies of the dissertation.

[BACK](#)
[CLOSE WINDOW](#)

Copyright © 2016 Copyright Clearance Center, Inc. All Rights Reserved. [Privacy statement](#). [Terms and Conditions](#). Comments? We would like to hear from you. E-mail us at customer@copyright.com



RightsLink®

[Home](#)
[Create Account](#)
[Help](#)


Title: Passive stability and control of quadrupedal bounding with a flexible torso

Conference Proceedings: Intelligent Robots and Systems (IROS), 2013 IEEE/RSJ International Conference on

Author: Q. Cao; I. Poulakakis

Publisher: IEEE

Date: 3-7 Nov. 2013

Copyright © 2013, IEEE

LOGIN
If you're a copyright.com user, you can login to RightsLink using your copyright.com credentials. Already a **RightsLink user** or want to [learn more?](#)

Thesis / Dissertation Reuse

The IEEE does not require individuals working on a thesis to obtain a formal reuse license, however, you may print out this statement to be used as a permission grant:

Requirements to be followed when using any portion (e.g., figure, graph, table, or textual material) of an IEEE copyrighted paper in a thesis:

- 1) In the case of textual material (e.g., using short quotes or referring to the work within these papers) users must give full credit to the original source (author, paper, publication) followed by the IEEE copyright line © 2011 IEEE.
- 2) In the case of illustrations or tabular material, we require that the copyright line © [Year of original publication] IEEE appear prominently with each reprinted figure and/or table.
- 3) If a substantial portion of the original paper is to be used, and if you are not the senior author, also obtain the senior author's approval.

Requirements to be followed when using an entire IEEE copyrighted paper in a thesis:

- 1) The following IEEE copyright/ credit notice should be placed prominently in the references: © [year of original publication] IEEE. Reprinted, with permission, from [author names, paper title, IEEE publication title, and month/year of publication]
- 2) Only the accepted version of an IEEE copyrighted paper can be used when posting the paper or your thesis on-line.
- 3) In placing the thesis on the author's university website, please display the following message in a prominent place on the website: In reference to IEEE copyrighted material which is used with permission in this thesis, the IEEE does not endorse any of [university/educational entity's name goes here]'s products or services. Internal or personal use of this material is permitted. If interested in reprinting/republishing IEEE copyrighted material for advertising or promotional purposes or for creating new collective works for resale or redistribution, please go to http://www.ieee.org/publications_standards/publications/rights/rights_link.html to learn how to obtain a License from RightsLink.

If applicable, University Microfilms and/or ProQuest Library, or the Archives of Canada may supply single copies of the dissertation.

[BACK](#)
[CLOSE WINDOW](#)

Copyright © 2016 Copyright Clearance Center, Inc. All Rights Reserved. [Privacy statement](#). [Terms and Conditions](#).



RightsLink®

[Home](#)
[Create Account](#)
[Help](#)


Title: On the energetics of quadrupedal bounding with and without torso compliance

Conference Proceedings: Intelligent Robots and Systems (IROS 2014), 2014 IEEE/RSJ International Conference on

Author: Q. Cao; I. Poulakakis

Publisher: IEEE

Date: 14-18 Sept. 2014

Copyright © 2014, IEEE

[LOGIN](#)
If you're a copyright.com user, you can login to RightsLink using your copyright.com credentials. Already a **RightsLink user** or want to [learn more?](#)

Thesis / Dissertation Reuse

The IEEE does not require individuals working on a thesis to obtain a formal reuse license, however, you may print out this statement to be used as a permission grant:

Requirements to be followed when using any portion (e.g., figure, graph, table, or textual material) of an IEEE copyrighted paper in a thesis:

- 1) In the case of textual material (e.g., using short quotes or referring to the work within these papers) users must give full credit to the original source (author, paper, publication) followed by the IEEE copyright line © 2011 IEEE.
- 2) In the case of illustrations or tabular material, we require that the copyright line © [Year of original publication] IEEE appear prominently with each reprinted figure and/or table.
- 3) If a substantial portion of the original paper is to be used, and if you are not the senior author, also obtain the senior author's approval.

Requirements to be followed when using an entire IEEE copyrighted paper in a thesis:

- 1) The following IEEE copyright/ credit notice should be placed prominently in the references: © [year of original publication] IEEE. Reprinted, with permission, from [author names, paper title, IEEE publication title, and month/year of publication]
- 2) Only the accepted version of an IEEE copyrighted paper can be used when posting the paper or your thesis on-line.
- 3) In placing the thesis on the author's university website, please display the following message in a prominent place on the website: In reference to IEEE copyrighted material which is used with permission in this thesis, the IEEE does not endorse any of [university/educational entity's name goes here]'s products or services. Internal or personal use of this material is permitted. If interested in reprinting/republishing IEEE copyrighted material for advertising or promotional purposes or for creating new collective works for resale or redistribution, please go to http://www.ieee.org/publications_standards/publications/rights/rights_link.html to learn how to obtain a License from RightsLink.

If applicable, University Microfilms and/or ProQuest Library, or the Archives of Canada may supply single copies of the dissertation.

[BACK](#)
[CLOSE WINDOW](#)

Copyright © 2016 Copyright Clearance Center, Inc. All Rights Reserved. [Privacy statement](#). [Terms and Conditions](#).



RightsLink®

[Home](#)
[Create Account](#)
[Help](#)


Title: On the control of gait transitions in quadrupedal running

Conference Proceedings: Intelligent Robots and Systems (IROS), 2015 IEEE/RSJ International Conference on

Author: Q. Cao; A. T. van Rijn; I. Poulakakis

Publisher: IEEE

Date: Sept. 28 2015-Oct. 2 2015

Copyright © 2015, IEEE

[LOGIN](#)

If you're a **copyright.com user**, you can login to RightsLink using your copyright.com credentials. Already a **RightsLink user** or want to [learn more?](#)

Thesis / Dissertation Reuse

The IEEE does not require individuals working on a thesis to obtain a formal reuse license, however, you may print out this statement to be used as a permission grant:

Requirements to be followed when using any portion (e.g., figure, graph, table, or textual material) of an IEEE copyrighted paper in a thesis:

- 1) In the case of textual material (e.g., using short quotes or referring to the work within these papers) users must give full credit to the original source (author, paper, publication) followed by the IEEE copyright line © 2011 IEEE.
- 2) In the case of illustrations or tabular material, we require that the copyright line © [Year of original publication] IEEE appear prominently with each reprinted figure and/or table.
- 3) If a substantial portion of the original paper is to be used, and if you are not the senior author, also obtain the senior author's approval.

Requirements to be followed when using an entire IEEE copyrighted paper in a thesis:

- 1) The following IEEE copyright/ credit notice should be placed prominently in the references: © [year of original publication] IEEE. Reprinted, with permission, from [author names, paper title, IEEE publication title, and month/year of publication]
- 2) Only the accepted version of an IEEE copyrighted paper can be used when posting the paper or your thesis on-line.
- 3) In placing the thesis on the author's university website, please display the following message in a prominent place on the website: In reference to IEEE copyrighted material which is used with permission in this thesis, the IEEE does not endorse any of [university/educational entity's name goes here]'s products or services. Internal or personal use of this material is permitted. If interested in reprinting/republishing IEEE copyrighted material for advertising or promotional purposes or for creating new collective works for resale or redistribution, please go to http://www.ieee.org/publications_standards/publications/rights/rights_link.html to learn how to obtain a License from RightsLink.

If applicable, University Microfilms and/or ProQuest Library, or the Archives of Canada may supply single copies of the dissertation.

[BACK](#)
[CLOSE WINDOW](#)



Confirmation Number: 11536074
Order Date: 02/03/2016

Customer Information

Customer: Qu Cao
Account Number: 3000889280
Organization: Qu Cao
Email: caoqu@udel.edu
Phone: +1 (302)5610658
Payment Method: Invoice

This is not an invoice

Order Details

Journal of mammalogy

Billing Status: N/A

Order detail ID: 69593301
ISSN: 0022-2372
Publication Type: Journal
Volume:
Issue:
Start page:
Publisher: AMERICAN SOCIETY OF MAMMALOGISTS.
Author/Editor: AMERICAN SOCIETY OF MAMMALOGISTS

Permission Status: **Granted**
Permission type: Republish or display content
Type of use: Thesis/Dissertation
Order License Id: 3801490839200

Requestor type: Academic institution
Format: Electronic
Portion: chart/graph/table/figure
Number of charts/graphs/tables/figures: 1
Title or numeric reference of the portion(s): Fig. 6
Title of the article or chapter the portion is from: N/A
Editor of portion(s): N/A
Author of portion(s): N/A
Volume of serial or monograph: 40
Issue, if republishing an article from a serial: 4
Page range of portion: 486
Publication date of portion: 1959
Rights for: Main product
Duration of use: Life of current edition
Creation of copies for the disabled: no
With minor editing privileges: no

For distribution to	Worldwide
In the following language(s)	Original language of publication
With incidental promotional use	no
Lifetime unit quantity of new product	Up to 499
Made available in the following markets	Academic Research
The requesting person/organization	Qu Cao, University of Delaware
Order reference number	
Author/Editor	Qu Cao
The standard identifier	None
Title	A MODELING AND CONTROL HIERARCHY OF QUADRUPEDAL RUNNING WITH TORSO COMPLIANCE
Publisher	University of Delaware
Expected publication date	May 2016
Estimated size (pages)	150

Note: This item was invoiced separately through our **RightsLink service**. [More info](#)

\$ 0.00

Total order items: 1

Order Total: \$0.00

[About Us](#) | [Privacy Policy](#) | [Terms & Conditions](#) | [Pay an Invoice](#)

Copyright 2016 Copyright Clearance Center